CAPITAL UNIVERSITY OF SCIENCE AND TECHNOLOGY, ISLAMABAD

Deep Learning Based Lumbar Spine Vertebrae Segmentation, Automated Measurements and Disorders Classification

by

Rao Farhat Masood

A thesis submitted in partial fulfillment for the degree of Master of Science

in the

Faculty of Engineering
Department of Electrical Engineering

2021

Dedicated to all extremely hardworking clinicians and health-care professionals.

CERTIFICATE OF APPROVAL

Deep Learning Based Lumbar Spine Vertebrae Segmentation, Automated Measurements and Disorders Classification

by

Rao Farhat Masood

MEE-191009

THESIS EXAMINING COMMITTEE

S. No.	Examiner	Name	Organization
(a)	External Examiner	Dr. Muhammad Usman Akram	NUST, Islamabad
(b)	Internal Examiner	Dr. Aamer Nadeem	CUST, Islamabad
(c)	Supervisor	Dr. Imtiaz Ahmad Taj	CUST, Islamabad

Dr. Imtiaz Ahmad Taj
Thesis Supervisor
February, 2021

Dr. Noor Muhammad Khan
Head
Dept. of Electrical Engineering
February, 2021

Dr. Imtiaz Ahmad Taj
Dean
Faculty of Engineering
February, 2021

Author's Declaration

I, **Rao Farhat Masood** hereby state that my MS thesis titled "**Deep Learning Based Lumbar Spine Vertebrae Segmentation, Automated Measurements and Disorders Classification**" is my own work and has not been submitted previously by me for taking any degree from Capital University of Science and Technology, Islamabad or anywhere else in the country/abroad.

At any time if my statement is found to be incorrect even after my graduation, the University has the right to withdraw my MS Degree.

(Rao Farhat Masood)

Registration No: MEE-191009

Plagiarism Undertaking

I solemnly declare that research work presented in this thesis titled **Deep Learning Enabled Lumbar Spine Vertebrae Segmentation, Automated Spinal Measurements and Spinal Disorder Disease Classification**" is solely my research work with no significant contribution from any other person. Small contribution/help wherever taken has been dully acknowledged and that complete thesis has been written by me.

I understand the zero tolerance policy of the HEC and Capital University of Science and Technology towards plagiarism. Therefore, I as an author of the above titled thesis declare that no portion of my thesis has been plagiarized and any material used as reference is properly referred/cited.

I undertake that if I am found guilty of any formal plagiarism in the above titled thesis even after award of MS Degree, the University reserves the right to withdraw/revoke my MS degree and that HEC and the University have the right to publish my name on the HEC/University website on which names of students are placed who submitted plagiarized work.

(Rao Farhat Masood)

Registration No: MEE-191009

Acknowledgement

All praises and glorification for **Allah SWT** for enabling me with the ability to complete this work in a befitting manner. Undoubtedly without His most-needed and vital guidance, I was unable to explore the hidden depths and variabilities in His crafted creation.

I express my deepest gratitude to my worthy supervisor **Dr Imtiaz Ahmed Taj**, for providing me with most valuable input to usher my research accomplishments. Besides my supervisor, I am also grateful to the clinicians including both Radiologist and Spinal Surgeons for giving me their valuable feedback to assess the clinical relevance and significance of my research work. Additionally, I would also like to thank **Dr Sud Sudirman** for allowing me to use and redistribute his elaborate dataset after performing necessary modifications.

My work is continuously fueled by unceasing motivation and never-ending prayers of my beloved family especially my mother, wife and kids. The support and encouragement rendered by them made this work possible. Special drive for completion of this work is generated through personal motivation, being diagnosed with degenerative disc disease at multiple discs levels in 2017. I had special attachment and inspiration for completion of this work.

(Rao Farhat Masood)

Abstract

Automated image understanding in medical imaging is of paramount importance as it not only alleviates the clinicians' burden in time consuming process of manual image handling as well as offer degree of confidence towards their diagnostic decision making. Presently, maximum reliance for medical imaging diagnosis is either on manual image handling or through the use of semi-automated tools. These methods are invariably prone to dissimilarity and variation once performed by different clinicians. In this thesis, a composite image dataset of mid-sagittal views i.e., annotated labels along with relevant spinal measurements of lumbar spine magnetic resonance imaging (MRI) scans is introduced. The markings have been conducted in two stages. In the first stage, expert radiologists performed the pixel-wise mask generation to identify the vertebral bodies (VBs) within each scan, which, later on, are validated by a panel of spinal surgeons in the second stage. An improvised algorithm (VBSeg) in order to present a comprehensive comparative overview of segmentation task performed by proposed traditional method vis-à-vis deep learning architecture methods is also presented. The best performance for semantic segmentation is achieved by ResNet-UNet with dice similarity score (DSC) of 0.97 and intersection-over-union (IoU) of 0.86. To develop a comprehensive fully automated image understanding application relevant lumbar spine, subsequent spinal measurements encompassing distance based and angular based measurements are performed. These measurements are performed as per the clinical standards in practice extensively used by clinicians. The performance of the proposed scheme for spinal measurements are significantly correlated with the clinicians' grading, where a statistically significant correlation coefficient of 0.979 for the lumbar lordotic angle (LLA), 0.951 for the lumbosacral angle (LSA) and 0.99 for lumbar height is achieved. Furthermore, mean absolute error (MAE) between the clinicians' grading and proposed scheme was 1.45^{o} for LLA, 1.55^{o} for LSA and 0.8mm for lumbar height. Furthermore, a novel scheme for the automated assessment of spinal misalignments that may aid spinal surgeons in making objective decisions about required surgical interventions is also presented. For spondylolisthesis classification, an accuracy of 89% by using angular deviation metric

whereas, 93% accuracy for determining adequacy/inadequacy in LL assessment through computation of area within enclosed lumbar curve region is achieved. In addition to this, the dataset with all the clinicians markings are publicly released at https://data.mendeley.com/datasets/k3b363f3vz/1.

Contents

List of Figures

List of Tables

List of Algorithms

Abbreviations

MRI	Magnetic Resonance Imaging
CT	Computed Tomography
VB	Vertebral Body
IVB	Intervertebral Body
VA	Vertebral Arch
LL	Lumbar Lordosis
LLA	Lumbar Lordotic Angle
LSA	Lumbosacral Angle
IVD	Intervertebral Body Disc
MIS	Minimal Invasive Surgery
PLIF	Posterior Lumbar Interbody Fusion
ALIF	Anterior Lumbar Interbody Fusion
TLIF	Transforaminal Lumbar Interbody Fusion
XLIF	Extreme Lateral Interbody Fusion
TRALL	Tangential Radiologic Assessment of Lumbar Lordosis
HPTM	Harrison Posterior Tangent Method
AUC	Area Under the Curve
UNet	U-Shaped Deep Learning Network
ResNet	Residual Network
SegNet	Segmentation Network
PSPNet	Pyramid Scene Parsing Network
MobileNets	Mobile Network

Chapter 1

Introduction

1.1 Outline

In this chapter, background information regarding the problem statement with the inherent underlying challenges faced while addressing the problem is presented. Initially, the anatomical area of human spine considered more susceptible to severe degenerative changes as compared to other spinal regions will be covered. After discussing the region of spine, the investigative examinations commonly recommended by the clinicians in order to diagnose lower-back pain including both computed tomography (CT) scan and magnetic resonance imaging (MRI) scan will be discussed. A user preference will be identified in terms of suitability, safety and convenience while undergoing a specific diagnostic examination. In the last part of the chapter, the challenges faced by clinicians while diagnosing patients with lower-back pain and how these challenges are presently addressed, will be elaborated. The importance of medical image segmentation towards developing an image understanding application will also be unfolded.

1.2 Background

Chronic backache in general and lower back pain in particular is considered one of the most commonly naturally occurring ailment by both the radiologists and spinal surgeon community [1–3]. Lumbar spine or lower-back is the area which once effected gives rise to lower-back pain clinically referred as lumbago, degrading the quality of life (QoL) [4] in patients. In most of the cases, the low-back-pain is associated to muscular or ligaments strain which is mostly caused by improper weight-lifting and sitting in improper posture for a longer duration [5, 6]. It is commonly termed as localized back-ache which is the aftermath of acute back-ache episode and is generally relieved by proper rest. The clinicians in some cases recommend physiotherapy augmented with radiation therapy or ultrasonography to relieve the muscular spasm. In chronic cases, lower back pain be caused due to multiple reasons. Lower back pain may be caused by a fracture of the vertebral body (VB) or vertebral arch (VA), thereby reducing the space between the vertebral bodies which is occupied by intervertebral discs (IVDs) [5]. The fracture in bone will generate an imbalance in IVD load sharing thereby causing the disc to protrude or herniate. As a consequence, the protruding or slipped discs exert pressure on the existing nerve roots causing tingling pain in legs and lower body paralysis in case of nerve damages [7]. This nerve compression which as a result radiates pain in either or both legs is commonly referred as sciatica [8]. In other cases, due to aging effect, VBs undergo end-plate deformation commonly known as osteophytes[9] formation [10]. This region of VB may intrude the exiting nerve roots and cause compression. The candidate patient may be considered suitable to undergo a spinal surgical intervention procedure usually but not limited to decompression procedure, in order to relief the pressure exerted on the nerves, thereby restoring the better QoL.

1.3 How Lower-Back Pain is Diagnosed?

In order to diagnose the patient with back-ache in general and lower-back pain in particular the clinician normally recommends the patient to undergo MRI exam of lumbar spine. An analysis was presented by Suri P et al. [7] that lumbar spine MRI exam is considered a standard investigative procedure while diagnosing lower-back pain. Based on their study performed on 313 total patients, 77 % of patients with complaints of lower-back pain underwent MRI exam. Out of those patients who underwent the MRI exam, 73.8 % of patients came with abnormal findings i.e., diseased lumbar spine. The total abnormal findings were 183 out of 313 that is 58.5 % included symptoms were diagnosed with lower-back pain disease. In addition, data was also formulated regarding the number of MRI exams being performed in one of the biggest institutes of radiology in Pakistan. Based on the data as presented in table 1.1, the number of MRI exams performed for spine region are relatively more in number once compared to the scans performed for other regions of the body excluding the brain. Based on the data, lumbar spine and cervical aggregated to 38.47 % of the total scans. Most scans i.e., 45.27 % were performed to investigate diseases related to the brain region.

1.4 MRI Scan or CT Scan - Subjects' Preference

If we narrow the medical imaging techniques down to CT scan and MRI only, the patients are more comfortable to undergo an MRI examination as it is free of ionization radiation, hence is considered the safest image acquisition method. While CT scan has its own application areas, both clinical and medical imaging researchers have made use of CT images for spine related segmentation and identification tasks. Here, the basic differences in MRI and CT scan are presented below:

- In CT scan, the candidate patient is exposed to more x-ray radiation as compared to single plane X-ray scan. Image reconstruction is performed as

TABLE 1.1: Category wise number of MRI Scans performed in Armed Forces Institute of Radiology (AFIRI), Rawalpindi, Pakistan from September 2020 to November 2020.

	Months			**Monthly**	**Percentage**
MR Scan Type	September	October	November	*Average*	%
Brain	646	610	620	625	45.27
Lumbar Spine	305	321	294	307	22.20
Cervical Spine	285	225	164	225	16.26
Shoulder	36	27	29	31	2.22
Sacroiliac Joint	47	40	40	42	3.06
Knee	151	162	68	75	5.41
Elbow	7	5	3	57	4.15
Hip	6	5	42	18	1.28
Wrist	2	1	3	2	0.14
Total	**1485**	**1396**	**1263**	**1382**	

a post-processing step exhibiting more information in multi-planer images. The principle of image generation is same as in conventional X-ray image generation, wherein high-density tissues such as bones etc. appear brighter as compared to low-density tissues such as lungs, kidneys etc.[11].

- MRI examination, unlike the CT Scan, the candidate patient is not exposed to any ionization radiation. It takes more time to perform the scan however gives superior details as compared to CT scan images[12, 13].

- Usually, for bone related disease investigation the medical consultants advise the patient to undergo a CT scan, whereas in case of organ/ muscle related disease investigation, MRI is more preferred mode of diagnostic examination [12].

After assessing the useful of MRI examination towards investigating lower-back pain, brief overview regarding standard MRI lumbar spine sequences with respect to the type of information contents in image is presented. Subsequently, MRI scan cycle related to patient is also described.

1.5 Body Planes

Before explaining the standard lumbar spine sequences, it is imperative to establish familiarity with standard reference planes and reference positions used to specify anatomy in human body. These planes are primarily used for identification and location of internal organs in medical imaging techniques by enabling the radiologist to divide the anatomical regions as per the region of interest. Consider the human body as shown in figure1.1, from the observer point of view, there are three two-dimensional planes [14, 15] which are used to describe the cross-sections of body.

- **Sagittal Plane**

  The plane in which the observer is facing the body sideways is termed as sagittal plane or lateral plane. It divides the body in right and left sides.

- **Axial Plane**

  This plane divides the body into superior or top and inferior or bottom regions. It is parallel to the ground and is also called as transverse plane. The observer is viewing the body from either the top end or the bottom end.

- **Coronal Plane**

  The plane in which observer is facing the body from the front is termed as coronal plane. It divides the body front or anterior and back or posterior regions.

1.6 Standard MR Image Sequences for Lumbar Spine

Let us first review the basics of image construction in MRI. Since, human body is composed of tissues containing higher hydrogen nuclei which behave as a tiny magnet in isolation. Once the human body is exposed to external higher magnetic

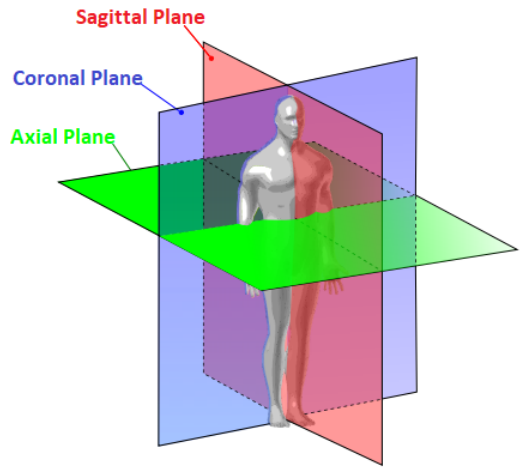

FIGURE 1.1: Human Body Reference Anatomical Planes [16].

field, these smaller magnets align with the field. This phenomenon is termed as precession. The protons in the aligned hydrogen nuclei are excited by impact of a radio frequency of a specific frequency called as Larmor frequency. The protons de-excites once the radio frequency is turned off and generates an MR signal which is subsequently used to construct the image using spatial encoding [11, 17, 18]

The relaxation of protons and emittance of MR signal is related to the specific tissue type and are categorized into two types namely T1 relaxation and T2 relaxation [19]. In standard practice sagittal and axial views for T1- and T2-weighted images are generated, however in certain cases coronal views, T2-weighted fat saturated (sagittal) slice sequences are also generated[20, 21].

Side-by-side view of both T1- and T2- weighted images of lumbar spine is shown in the figure 1.2. End-plate deformation in the VB, disc bulge and contrast difference of hydrated and dehydrated IVD is also depicted. It can be seen that T1-weighted images give the bright (white) representation of fat containing structures while on the other hand, T2-weighted images gives the bright (white) representation of both fat and fluid-based contents [22]. T1 images are generally more suited for anatomical depiction while T2 images are considered for pathological evaluation [22]. For the purpose of this thesis, the image acquisition modes are truncated to basic T1- and T2-weighted images only; there are certain variations which are used suited specifically for the anatomical region under study[23]

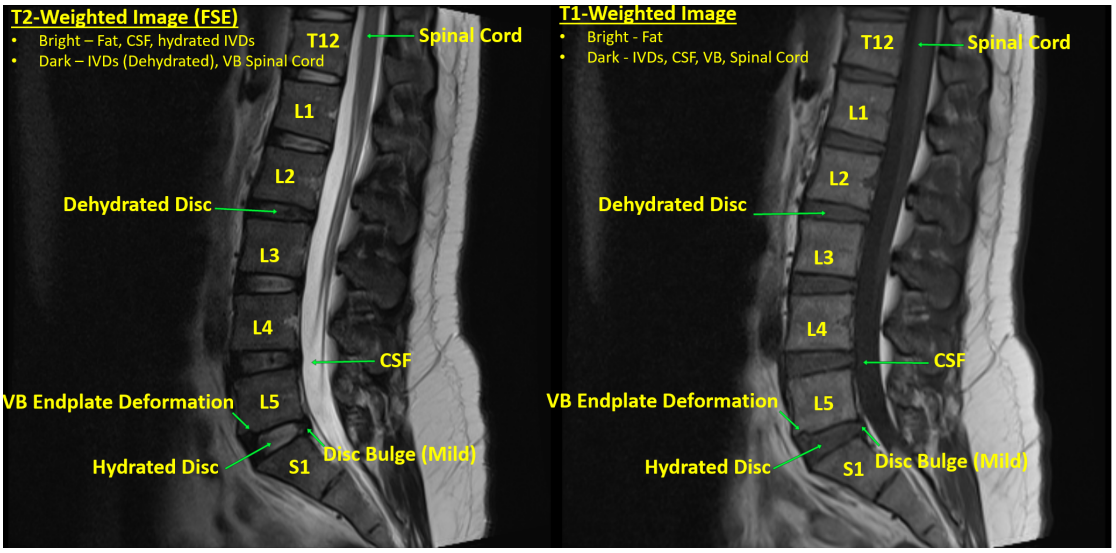

FIGURE 1.2: T1- and T1-Weighted Images of Lumbar Spine

The variation in information presented by both T1- and T2-weighted images for lumbar spine region is summarized in table 1.2. The easiest way to identify between a T1- and T2-weighted image is to identify cerebrospinal fluid (CSF) [24] which gives bright intensity levels in T2-weighted images and dark intensity in T1-weighted images [25]. Additionally, the hydrated IVDs appear bright in T2-weighted images whereas, in T1-weighted images both hydrated and dehydrated IVDs appear dark.

1.7 MRI Exam Sequence

As previously highlighted that MR images gives more information as compared to CT scan images, therefore, an MR exam is more suited to investigate the lumbar spine region. A candidate patient undergoes MRI examination of Lumbar Spine on the recommendation of consultant specialist with a view to ascertain the cause of lower-back pain or the specific complaint of the candidate patient. The scan is performed on MRI machine which varies from 20-45 minutes based on the magnetic strength of the MRI machine. Usually only sagittal and axial slices are generated for most of the cases, however, for particular patients with scoliosis, coronal scan is also included in the MRI exam [26].

TABLE 1.2: Comparison of Information Contents in T1- and T2-Weighted Images of Lumbar Spine.

	Dark	**Bright**
T1	IVDs (All)	Epidural Fat
	CSF†	Sub-cutaneous tissue fat
	Muscle Mass	
	Spinal Cord	
	Blood Vessels	
	VB End-plates	
	Nerves	
T2	IVDs (Dehydrated)	IVDs(Hydrated)
	Muscle Mass	*Epidural Fat
	Spinal Cord	*Sub-cutaneous tissue fat
	Blood Vessels	CSF†
	VB End-plates	
	Nerves	
		*In case of non-fat saturated image.

After the completion of scan, the Digital Imaging and Communications in Medicine (DICOM) [27] images are fed through Picture Archiving and Communications System (PACS) [28] to the radiologist for review/evaluation and report generation. A radiologist narrates the findings seeing the MRI images only without having physically examining the patient. The patient along with the radiologist analysis report and MRI scans, visits to the referring consultant for final verdict.

The patient obtains a final verdict from a spinal surgeon who evaluates the subject patient clinically and establishes a correlation between the clinical findings i.e., physical symptoms with the MRI scan. A conclusion is made towards conservative treatment or adoption of appropriate surgical intervention procedure to eradicate the ailment.

1.8 Challenges in Diagnosing Lower Back-Pain

Invariably, the present system of diagnosing lower-back pain is time consuming and laborious task which is graded subjective in nature. The evaluation of same candidate subject is prone to variation once made by different clinicians, as the clinicians have varied experiences and skill-sets. These deviations of observation are augmented with variability in clinical findings which are observed by relevant clinician i.e., assessment of spinal surgeon may differ from the assessment performed by orthopedic surgeon in case of analyzing lumbar spine disorders/diseases.

A convenient way to offset this variation is introduction of certain quantitative methods towards establishing a concrete analysis for diagnosis of lumbar spine region. At present, the spinal surgeons and radiologist community are dependent on manual or software-assisted image understanding methods for acquiring certain quantitative attributes, which are certainly laborious, time-consuming methods and are likely to be subjective in nature based on the variation of observer both intra- and inter-medical specialty i.e., within radiologists and spinal surgeons. The quantitative methods for performing spinal assessment includes spinal alignment measurements, spinal deformation attributes and spinal balance readings.

1.9 Significance of Spinal Measurements

Spinal measurements are directly related to the spinal balance and correct spine geometry of human spine. These measurements are extremely important pre-operative procedure to restore the normal spinal lordosis enabling posture correction and spinal balance restoration. The spinal disorders elaborated in this thesis are assessment for adequacy/inadequacy in lumbar lordosis and presence of spondylolisthesis.

It has been clinically established [29] that lumbar load bearing and impact of stress sharing are remarkably affected in altered lumbar lordosis (LL) i.e., inward

angle of lumbar spine. It was established by Berven et al. [30], that restoration of LL [31] i.e., inward angular curve at lumbar area is important aspect of spine reconstructive procedure once the lordosis range was found inadequate.Additionally, based on a research conducted by Chun et al. [32], a strong relationship was identified between the lower-back pain and flat back condition i.e., less LL. It was also found to be associated with disc degeneration or herniated discs. Furthermore, based on the study conducted by Rafael et al. [33] a correlation was developed between LL and lumbago. It was also found in another study by Breven et al. [30] that patients with lumbar disc herniation undergoing surgical procedure were found to have increased LL, however have shown decrease in perceived pain. In the same research [30], while evaluating segmental lordosis it was found that segmental lordosis is greatest for L4-L5 and L5-S1 motion segments. The same is quantitatively experienced during this work. Based on the analysis of research carried out in 2014, lordotic curve angle is associated with spinal misalignment disorders like spondylosis [34–36] and spondylolisthesis [37, 38] commonly termed as out of alignment of the VB. It was also found in another study carried out by Hashimoto et al. [39]that subsequent adjacent segment degradation was directly related to efficacy of the restoration procedure- that is, if not correctly performed at L4 to S1, adjacent segment is prone to more degradation. The relevant spinal measurements enable the spinal surgeon in making an estimation of effective posture correction post-operative procedure [40].

1.10 Challenges in Medical Image Analysis

Over the period of time, substantive work has been done in medical image analysis for addressing the formidable computer vision problems related to segmentation, identification and labelling. The exponential growth of diagnostic imaging data in the medical industry with wide variety, intensive volume, enormous speed, diversity and importance [41]; has substantiated the need for more robust, dynamic techniques for image information extraction and evaluation in a response to address the related problems.

Certainly, the noise and undesired artifacts such as inhomogeneities in intensity, random noise caused by external interference, motion related noise, within the MR images can also become extremely challenging for the researchers and clinicians to correctly identifying the disease [42, 43]. Thus, to counter these challenges the researchers have to use various pre-processing and post-processing techniques [44–47].

As mentioned in section 1.4 MRI is generally more suited for soft-tissues as opposed to CT as the bone appears dark in MR images, however, the bony structures which are visible in MRI scan are a mixture of bone, fat and water. This adds an additional challenge to segment the bones and soft-tissues because of the overlapping regions, therefore conventional methods based on edge-based segmentation or intensity-based segmentation may not work well [48]. Equally challenging is the variability in content of the image which significantly varies from subject to subject.

As it was previously highlighted that, the analysis report generated by radiologists is focused on identification and presence of spinal disease whereas the spinal surgeon clinically evaluates the patients with reference to the exhibited symptoms to build correlation between the MR images and the pain symptoms. In order to build this correlation, spinal quantitative assessment is performed either manually or by the use of software-assisted methods. Therefore, an automated quantitative assessment tool for lumbar spine region is necessitated enabling the clinicians to offset the inter- and intra-clinician variation by obtaining reproduceable automated readings.

1.11 Thesis Structure

To best present the contents of the conducted work, the thesis is structured as follows:

Background of problem and challenges faced by both clinicians and medical imaging researchers are covered in chapter 1. Chapter 2 identifies the research gaps in the reviewed literature and enumerate the contributions to furnish the identified gaps. Anatomy of lumbar spine with pathological conditions and clinicians' including radiologist and spinal surgeons' perspective is discussed in chapter 3. The methodology adopted for creation of ground truth images is covered in chapter 4 whereas, the category wise segmentation details are elaborated in chapter 5. After execution of the segmentation task, extraction of clinically significant spinal measurements are highlighted in chapter 6. The proposed methodologies for classification of spinal disorder diseases are explained in chapter 7 followed by presentation of results achieved for the performed tasks with analysis in chapter 8. In the last chapter 9, summary of work is concluded and research direction for future work is narrated.

1.12 Summary

- The assessment of lumbago performed manually by clinicians is subjective and is prone to variation based on the skill level and experience of clinician.
- Presently, little to none quantitative correlative analysis is performed by the clinicians while assessing the lumbar spine for spinal disorders.
- There is a definite requirement of developing an automated image understanding tool to establish clinical correlation between the perceived symptoms and MR image through quantitative measurements.
- The challenges contained in MR images demand rigorous empirical implementation of image processing methods and techniques to counter the challenges.
- To attain this task, image segmentation is foremost requirement followed by subsequent automated spinal measurements.

Chapter 2

Literature Review, Problem Statement and Research Contributions

2.1 Outline

In this chapter, a concise non-exhaustive literature review has been presented regarding the previous work on development of ground truth image dataset for lumbar spine images, methods and techniques used by various other researchers to segment out the region of interest, which for this thesis is the VB in lumbar spine region. The methods and techniques used to carryout spinal measurements bearing most clinical significance and relevance prior to the surgical intervention procedure is also discussed in section 2.4. A brief analysis of the reviewed work is also presented to determine the suitability for the research continuity. In the last section 2.5 of the chapter, analysis is presented in order to identify the existing research gaps and the efforts that have been made in this thesis to fill those gaps.

2.2 Development of Image Ground Truth Dataset

Considering the work being done regarding creation of ground truth image datasets of spinal in general and in particular lumbar spine region, following was overviewed: -

Bennani et al. [49] made use of 3D modelling using camera image-acquisition and reconstruction using image-based technique. The main idea was acquiring complete 360° scan of images at the same distance and then construction of 3D model using Agisoft Photoscan software which is currently upgraded to Agisoft Metashape [50].

Another free resource available is provided by Imperial College, London which comprises of CT scan images of 125 patients [51]. Multiple resources of labelled lumbar spine database are available on SpineWeb [52], however, the datasets are mostly composed of CT images and the ones with MR images are limited to less than 100 scans. Since, the focused area understudy is evaluation of lumbar spine through MRI scans therefore, other databases suggesting X-ray images and CT images are not used.

Burian et al. [53] have also published their work in creating a database of ground truth images in sagittal views highlighting the VBs from L1 and L5 and excluding the sacrum bone. The dataset is comprised of 54 images of healthy Caucasian subjects including water, fat and proton density fat fraction (PDFF) images and relevant masks. No information regarding the ailment related to spinal disorder was given in the dataset.

A recent work proposed by Loffler [54], provides vertebral segmentation masks for spine images with annotation comprising of fractures or spinal abnormalities. The dataset composed of CT scans of 141 patients is publicly available online [55].

The MRI database that is being used in this research thesis is publicly available at Mendeley website [56], provided ample variability with total of 515 scans of patients with symptomatic back pains. On the same dataset, Friska Natalia et

al.[57] have manually labelled the axial views of last three-disc levels. The regions of interest selected by them are also labelled and marked from number 1 to 4 in figure 2.1 including intervertebral disc (IVD) marked as number 1, posterior element (PE) marked as number 2, thecal sac (TS) marked as number 3 and area between anterior and posterior segments (AAP) marked as number 4. Later, with the labelled dataset, segmentation was performed for detection of spinal stenosis through semantic segmentation using deep learning based on U-Net[58] architecture [59].

The same dataset is picked and is considered suitable to perform segmentation of the VBs followed by spinal measurements. Prior executing segmentation task, labelling/annotation is done on the sagittal views. The details of labelling and creation of ground truth images in sagittal plane is covered in chapter 4.

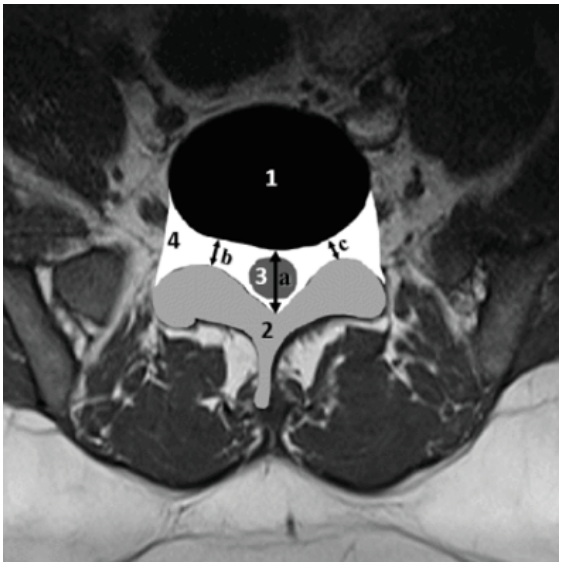

FIGURE 2.1: Regions of Interest of Lumbar Spine in Axial Planes

2.3 Segmentation and Labelling

In this part of the research thesis, previous work done towards medical image segmentation is highlighted based on use of both conventional methods for image segmentation and machine learning methods are presented in sub-section 2.3.1 deep learning methods to perform medical image segmentation [60] related tasks

is also reviewed in sub-section 2.3.2. Just to develop an understanding, a limited review of use of unsupervised learning for segmentation related task and its comparison with deep learning supervised methods is also presented in sub-section 2.3.3. The existing methods which are followed to perform segmentation tasks can be grouped in semi-automatic and fully automatic methods. The former suggests user intervention where the user may place certain landmarks followed by detection, whereas the latter is fully autonomous method of segmentation with no user intervention. A non-exhaustive summary of previous work is presented.

2.3.1 Conventional/Traditional Methods of Medical Image Segmentation

Smyth et al. [61] used Active Shape Model (ASM) [62] to measure the shape of VB on a dataset comprising of 84 x bone density scans or clinically termed as dual-energy X-ray absorptiometry (DXA) Images. The work was done through manual labelling the vertebrae on each image on a total of 10 vertebrae including 6 – Thoracic from T7-T12 and 4 Lumbar from L1-L4. In a similar work by Aslan et al. [63] made use of universal shape model in order to perform the segmentation task on CT Images.

Carballido et al. [64] used normalized cuts for spinal MRI segmentation task by seeking user input to select the vertebrae to keep. Their study also showed that a decline was seen in the segmentation results once mid-sagittal slice was not selected, giving importance to precise selection of mid-sagittal slice of MRI scan. In another work, generalized Hough transform (GHT) [65] template matching is used in order to locate the lumbar vertebrae in X-ray images [66]. Their work suggested matching a template and finding the vote for the best matched.

Zhu et al. [67] used Gabor filter banks to localize and the IVD, followed by spinal curve estimation, Gabor feature images (GFIs) of IVDs and finally segmenting the IVDs on a dataset comprising of T2 Images from 37 patients provided by a

Xinqiao Hospital, China, claiming the accuracy of localization to be 98.23 % and DSC for segmentation to be 0.9237.

Similary, in another work, clustering based on fuzzy c-means algorithm and segmentation was performed by making use of GHT on a dataset comprising of cervical radiograph scans. The accuracy claimed by the method is 96.88 % [68]. A similar work was done making using of k-means clustering and GHT (template matching) [69, 70].

In another work by Bampis et at. [71], spinal canal segmentation and extraction has been performed by making use of k-means clustering in T2-weighted images of sagittal slices.

Glocker et al. [72] made use of classification random forests in order to localize (finding centroids) using a dataset based on CT Images, claiming the identification rate of 81 % with overall median localization error of less than 6mm.

2.3.2 Deep Learning Based Methods for Medical Image Segmentation

Lu et al. [73] performed the segmentation task on sagittal MR images by making use of U-Net architecture. The image input size chosen was 512 x 512. The evaluation criteria was to ascertain the number of VBs detected and that detected sacrum bone should not overlap the lumbar area once compared with the GT Images. They have detected 188 VB out of total 200 (accuracy 94 %), with dice similarity coefficient being 0.93 of standard deviation 0.02. They have also performed quantitative evaluation of mean error distance between center of GT Image with the detected center to be 0.79 mm with standard deviation of 0.44 mm.

Janssens and Zheng [74] performed the segmentation task on CT Images using Fully Connected Network (FCN) and obtained DSC 0.9577 $\pm$ 0.81 and average symmetric surface distance of 0.37 $\pm$ 0.06 mm. The approach follows a localization

net based on FCN to localize the region of interest (Lumbar Spine) followed by Segmentation-Net (FCN) which segments the lumbar spine vertebrae within the cropped regions. 15 x CT Images were used to perform the segmentation. (DSC 0.9577 $\pm$ 0.81, JC 0.9190 $\pm$ 1.48, Hausdorff Distance (HD) [75] 4.32 $\pm$ 2.60, ASSD 0.37 $\pm$ 0.06)

Lessmann et al. [76] made use of CNN for vertebrae segmentation and achieved an average DSC of 94.9 % on various datasets including both CT and MRI images.

Tang et al. [77] proposed the use of Dual Densely Connected U-Net architecture to segment out the regions on axial scans extracted from CT Images. The metrics pixel accuracy (PA) – 0.9913, mean pixel accuracy – 0.9099, mean Intersection over Union (IoU) 0.8331 and frequency weighted IoU 0.9835 were evaluated.

Benjdira et al. [78] performed semantic segmentation using U-Net architecture on Ultrasound Images of Lumbar Spine claiming its useful for spinal surgeons during and after the laminectomy [79] surgical procedure in which part of the bone which causes nerve compression is removed.

As suggested in the work by Hassan et al. [80] RAGNet [81], originally proposed by the same group is used for performing retinal lesions segmentation. In their work, they have compared the performance of various deep learning frameworks on lesion segmentation. They have exhibited that RAGNet has shown most promising results as compared to other models like U-Net [58], SegNet [82] and PSPNet [83] due to its inherent retention of lesion contextual information during image decomposition, is well suited for retinal images.

In this thesis, harvesting the potential of pre-trained networks to perform segmentation tasks various models are trained through application of fine-tuning, the most refined transfer learning method, details of which are covered in chapter 5 section 5.3.4.

2.3.3 Supervised vs Unsupervised Learning

The work of Joyce et al. [84] suggesting usage of generative adversarial networks (GAN) [85] for segmentation and reconstruction by making use of labels from a different dataset (same anatomy) on cardiac images including both CT scan and MR images. Clearly their study suggests that supervised methods have given promising results. They were able to achieve dice similarity score of 0.84 on MR images and 0.87 on CT scan images with the help of supervised methods using U-Net architecture. In comparison, with unsupervised methods, the dice similarity coefficient was 0.66 for MR images and 0.51 for CT scan images.

2.4 Spinal Measurements

For the purpose of this research thesis, the existing in-use manual methods for spinal measurements are not reviewed. These methods include the use of inclinometer [86], flexible rulers [87, 88] and spinal mouse [89, 90]. The measurements are done either physically on the patient or on a radiography image. A comprehensive review related to semi-automated measurement methods, involving human intervention through software assistance as well as fully automatic methods without human intervention is presented.

2.4.1 Measurements through Semi-Automated Methods

The use of DICOM viewers with built-in measurement tools have been actively used in the past and are in present use of both spinal surgeons and radiologists while carrying out spinal measurements.

Many researchers, while evaluating the spinal curvature measurements through use of computer software relied on manual marking of landmarks for making the

respective measurements[91–94]. The manual landmarks included, the corner-points identification which were subsequently used to estimate the other spinal measurements including curve estimation.

Babai [95] made use of AutoCAD by Autodesk to measure the lumbar lordosis angle using 30 standing X-ray images. The work of MacIntyre et al. [96] compared the spine curve estimation by making use of IONMed Mobile phone application software assisted manual measurement) with the measurements made by digital inclinometers. The method involved an experienced rater to take both manual measurements using inclinometer as well as by making use of mobile phone app. The DICOM viewers, having these types of measurement tools, are commonly used by both the radiologists and spinal surgeons for making computer assisted measurements.

Zhang et al. [97] measured Cobb angle for scoliosis cases using 105 radiograph images in coronal plane and found 0.98 correlation between the manual measurement which is performed by clinician and computer aided measurement which is performed by non-clinician and the mean absolute error was found to be less than 3°.

All the above narrated works fall in the category of computer assisted measurements where a software helps to establish a relationship between the geometrical structure involving manual identification and selection of landmarks for measurements.

2.4.2 Measurements through Fully Automatic Methods

In the recent past, work has been done to develop computerized image understanding methods which will based on fully automated and semi-automated diagnosis thereby supporting the clinicians' manual diagnosis decision.

Pang et al.[98] have also claimed to have mean absolute error of 1.23 mm while computing spinal distances including VB dimensions from L1 superior-left corner

to L5 inferior-left corner in 225 images, however their method involves manual user input for identification of superior-left corner of L1 VB and inferior-left corner of L5 VB for providing reference to region of interest (ROI) cropping.

Cho et al. [99], presented the use of U-Net architecture and performed segmentation of lumbar spine on radiograph images of 151 images subsequently computing the lordotic angle (only) claiming to have mean absolute error of 8.055°, however correlation coefficient metric is not evaluated.

Masad et al. [100] have also measured lumbar lordosis in T2-MR images on 32 sagittal images and established a correlation of 93.2 % with manual Cobb Angle measurement, once tested on 27 images.

2.5 Problem Statement(s)

To summarize the reviewed literature, following gaps are identified which form part of the problem statement:

- Section 2.2 reveals that at present no lumbar spine dataset with related spinal measurements is publicly available which provides an extensive set of clinically significant spinal measurements.
- To solve the computer vision problems related to segmentation, labelling and identification, a clear bias has been identified advocating the use of deep learning and ruling out the conventional image segmentation methods as deliberate in section 2.3. Segmentation of region of interest (ROI) being the first step towards development of image understanding methods needs further investigative research. This necessitates, exclusive empirical evaluation of existing traditional image processing methods with deep learning models being popularly used in the research community.
- The present system of diagnosing medical ailments regarding lumbar spine are subjective in nature and lack quantitative assessment. Section 2.3 reveals

that clinicians rely on software-assisted methods to perform measurement which are time-consuming as well as prone to variation based on skill and expertise of the performing clinician. Furthermore, the development of automated image understanding tool involving spinal measurements and spinal disorder disease classification is also necessitated to facilitate the decision making and enhancing the diagnostic ability of both radiologists and spinal surgeons.

2.6 Contributions

Addressing to bridge the gap, following efforts have been made in this research thesis:

1. Detailed investigation of radiologists' analysis of MR scan vis-à-vis a spinal surgeons' preference is presented in order to establish clinical relevance towards building an automated spinal measurements tool. (Section 3.5)

2. To present in-depth image understanding regarding alignment and spinal balance, a composite dataset comprising of labelled/annotated image dataset (section 4.4) including clinically relevant automated spinal measurements (section 6.2) focused on lumbar spine that excludes VA is also created. The MRI dataset [56] is suitable for IVDs analysis as the annotations are in axial plane. In the proposed dataset is labelling is carried out in sagittal views, more suited for spinal balance assessment.

3. A conventional fully automated image segmentation algorithm (VBSeg) (section 5.2) is proposed to segment out the VBs. Existing deep learning methods being used to address the segmentation related task are also extensively experimented over the same dataset (section 5.3). A quantitative comparison is made in the results acquired by the use of the proposed conventional algorithm with those of deep learning methods.

4. A mathematical model for extraction of clinically relevant spinal measurements including angular and distance based measurements is also presented (section 6.2).

5. Additionally, automated spinal deformation classification methodologies for spondylolisthesis (section 7.2), hyper/hypo/normal lumbar lordosis assessment (section 7.3) are also proposed.

The basic framework of thesis is presented in figure 2.2, showing the input image being the first step followed by VB segmentation including labelling and identification of specific VB. The third step being the spinal measurements related to spinal geometry while the last step in which spinal disorder diseases classification is performed through automated means after estimation of spinal curve.

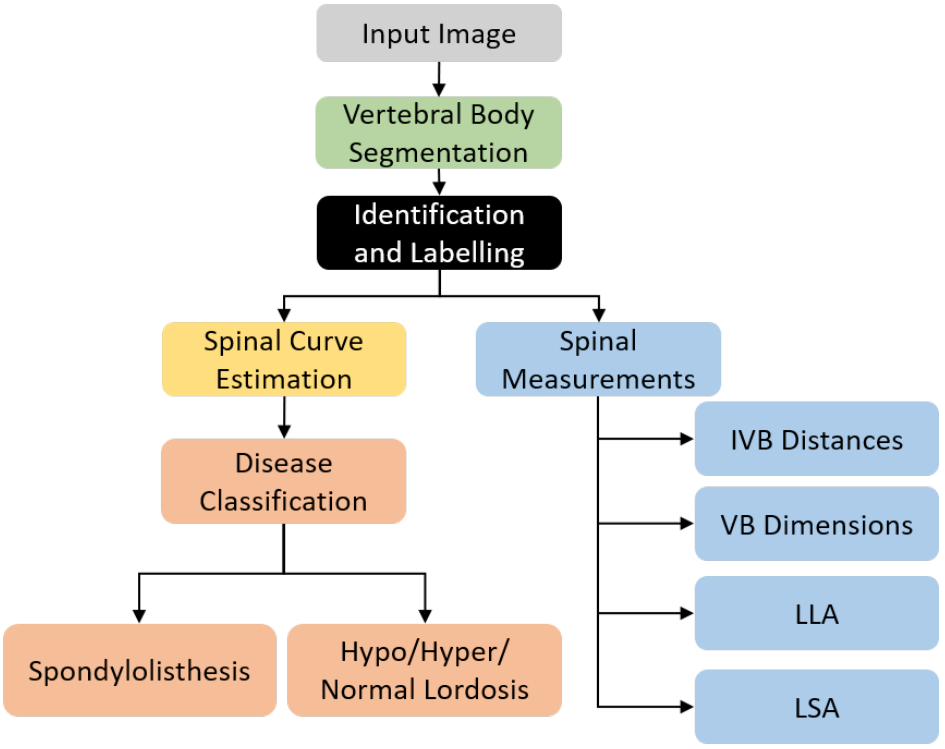

FIGURE 2.2: Thesis Framework

2.7 Summary

- Deep learning networks have shown promising results in performing semantic segmentation as compared to traditional machine learning based methods and algorithms.
- A tool for automated measurements will not only reduce the time to acquire relevant spinal measurements but also add confidence to the readings acquired through aid of computer assisted software.
- For development of an automated tool for a specific anatomical site, it is critically imperative and important to understand the clinical requirements and preferences of both radiologists and spinal surgeons, to make the tool clinically helpful. The clinical preferences of both radiologist and spinal surgeon while diagnosing lower-back related diseases and disorders are covered in chapter 3.

Chapter 3

Basic Lumbar Spine Anatomy with Pathophysiology and Clinicians' Overview

3.1 Outline

In this chapter, a brief introduction of lumbar spine anatomical structure with spinal diseases is presented. The reader will be able to understand the basic considerations undertaken by radiologists and spinal surgeons while diagnosing a subject for lower-back pain. In the last section of the chapter, certain clinically relevant spinal measurements are explained which are performed either manually or through software-assistance by spinal surgeons before spinal intervention procedure. These measurements play an important role to ascertain the normal curvature restoration in a subject with excessive inward curve in lumbar spine area.

3.2 Anatomy of Lumbar Spine

Human spine or vertebral column commonly known as backbone can be divided into five main regions that is cervical, thoracic, lumbar, sacrum and coccyx, comprising of normally thirty-three vertebrae [101] as shown in figure 3.1 [102]. The human spine with sections is shown in the left view which is taken in sagittal plane, while the subsequent section axial view is shown in the right of the figure.

In this research thesis, only lumbar spine region is under consideration, therefore, will be elaborated further. Lumbar spine begins after last thoracic (normally T12) vertebral body (VB) and ends at fused sacrum bone. It consists of total five vertebrae from L1 to L5 where each vertebra is composed of main VB in the anterior side or font-side and vertebral arch (VA) in the posterior side or back-side once looking at the human spine in lateral or sagittal view.

3.2.1 Main Vertebral Body (VB)

The main VB located at the anterior region, is the principle axial load bearing structure, where the space between the adjacent VBs is occupied by the intervertebral body discs commonly referred with respect to levels from L1-L2, L2-L3, L3-L4, L4-L5 and L5-S1. These intervertebral body discs (IVD) made up of fibrocartilage and provide cushion to the vertebral column while providing with stability by holding the adjacent VBs together and allowing mobility of spine. The outer portion of IVD is called anulus fibrosus while inner portion is called nucleus pulposus. A compromise in shape, size and structure of IVDs cause load sharing imbalance and functionality issues [103].

3.2.2 Vertebral Arch (VA)

The VA is composed of pair each (left side and right side) of transverse and articular processes while a single spinous process which is formed by joining of laminae from both sides. This portion of the vertebra provides protection to

spinal canal, a cavity through which spinal cord along with CSF passes. It also stabilizes the spine during excessive flexion and shear forces[104].

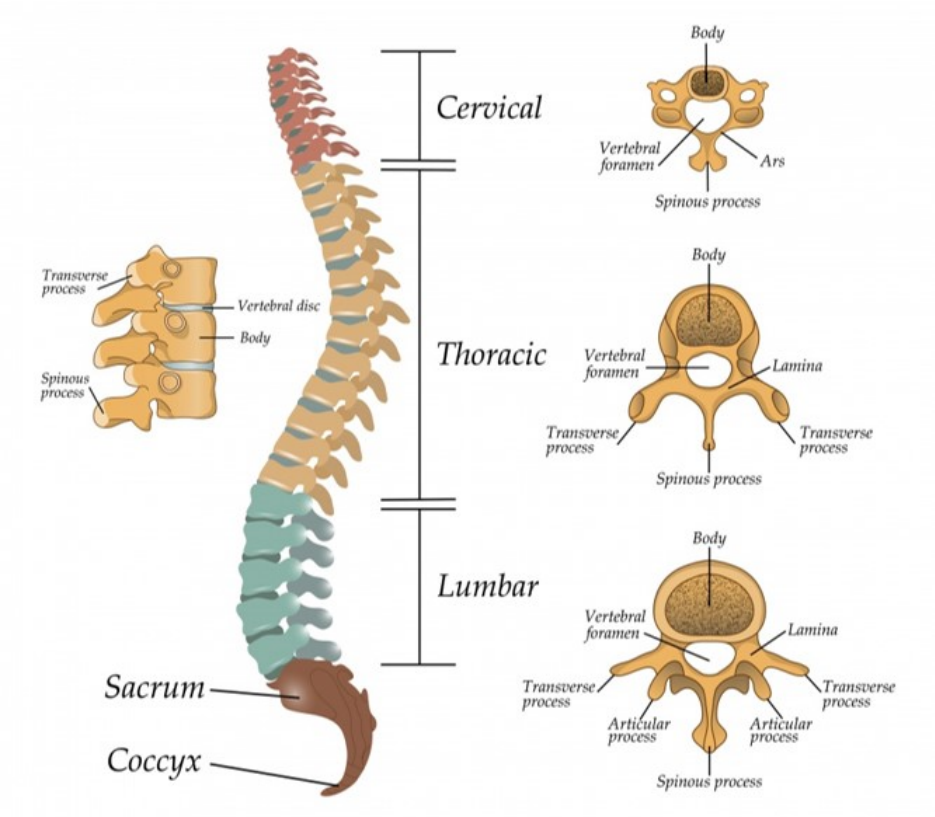

FIGURE 3.1: Sections of Human Spine

For the purpose of this research thesis, VA region which is at the posterior end or back side of the spine is not under consideration because spinal alignment measurements are associated with the main VB region of the spine.

3.3 Spinal Disorders (Pathophysiology)

In this section, the VB, IVD related issues / disorders and the clinical features showcasing the relevance of disorders are presented.

3.3.1 Degenerative Disc Diseases and related VB Changes

Degenerative disc diseases [105] are considered to be the most common disease which has been found to require surgical intervention procedure. Over 90 % of spinal surgical interventions are related to correct the degenerative disc diseases and related IVDs issues [106].

Mostly the patients with lower back pain symptoms have degenerative disease, in some form either due to the abnormal wear commonly termed as spondylosis in VB/IVD or reduction of cartilage which covers the bones commonly referred as osteoarthritis [107] .

These induced changes can be either based on aging or underdoing some trauma. It has also been found that sometimes degenerative changes attributable to aging are considered normal and do not cause pain [23]. In that case the center of IVD gradually dehydrates thereby imposing a limit in ability to absorb the shock and making the discs more susceptible to permanent damages.

Fracture in the VB also contribute towards degenerative changes of VB and IVDs. In some cases, the end-plate deformation or VA deformation is observed resulting in formation of bone spur commonly termed as osteophytes [108] significantly exerting pressure on the existing nerves. Some of the changes in spine due to degenerative diseases of IVDs are as follows:

- The *narrowing of disc* is aftermath of dehydration [104] i.e., drying out of nucleus pulposus. As a consequence, the discs become vulnerable due to lesser shock absorption with gradual reduction in the IVD volume and IVD space as shown in figure 3.2a. This as a result alter the spinal balance. It is also experienced by clinicians that healthy disc can withstand better shock absorption as compared to dehydrated discs. A hydrated and dehydrated IVD is also shown in figure 3.2a.

- *Annular tear* [109] is referred to the cracks in annulus fibrosis which is the outer ring of fiber as shown in figure 3.2b, where the IVD is interfering with

the thecal sac. The annulus fibrosis is surrounding nucleus pulposus which is gel-like structure in the center of IVD.

- *Disc herniation* [110] is displacement of disc material beyond the limits of annulus fibrosis and is commonly referred as slipped disc. *Disc bulge* [111] is the broad displacement of disc material usually in one direction as shown in figure 3.3.

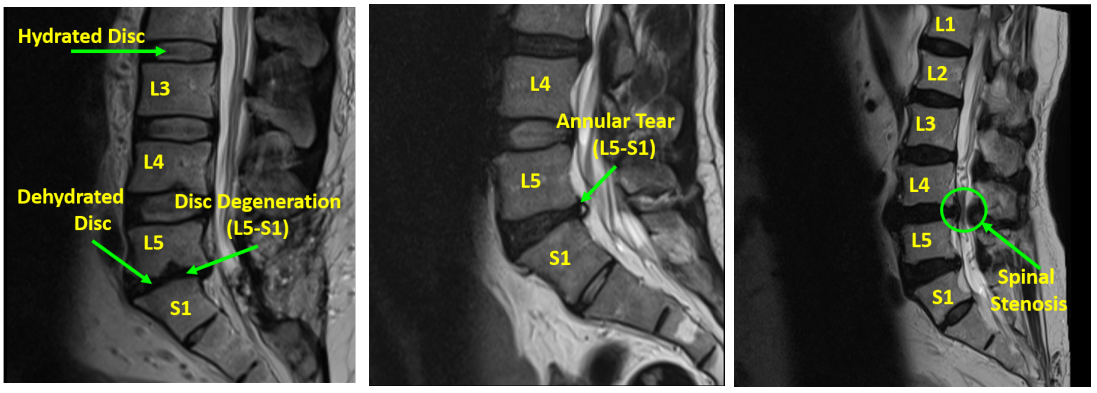

(a) IVD Degeneration (b) Annular Tear of IVD (c) Spinal Stenosis

FIGURE 3.2: Pathophysiological Conditions of Lumbar Spine.

3.3.2 Common Clinical Features

Most common clinical features in lumbar spine related to VB and IVD are discussed as under:

- *Sciatica* is typically pain radiating from back to lower leg usually caused by a prolapsed disc exerting pressure on the nerve root and causing compression.
- *Spinal stenosis* [112] is the condition in which the spinal canal is narrowed as shown in figure 3.2c due to the pressure exerted by the protruding disc from the front and thickening of yellow ligament from the back. As a result of this pressure, a tingling sensation of pain, which usually occurs after walking a certain distance and is relieved with rest.
- *Spondylolisthesis* is the condition in which VB is dislocated either towards anterior or posterior side in relation to its counterpart with which the VB

articulates. This malalignment is produced because of a fracture of the posterior element (VA) allowing the affected vertebra to slip. The same is pictorially represented in figure 3.3.

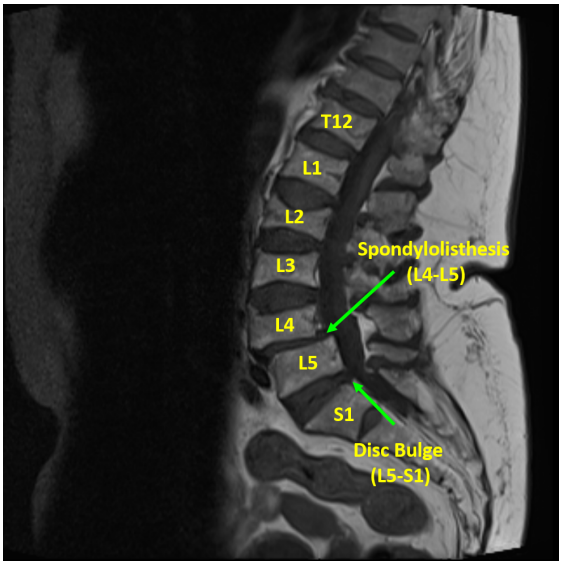

FIGURE 3.3: Spondylolisthesis and Disc Bulge in Lumbar Spine

3.4 Spinal Curvature Deformities

The major spinal curvature deformities including kyphosis, scoliosis and lordosis are shown in figure 3.4 and figure 3.5. For the purpose of this thesis while making automated measurements only lumbar spine is considered therefore, only lordosis related measurements will be elaborated. Typically, x-ray radiographs are used to make assessment towards analyzing normal or abnormal ranges in curve deformations [96].

A brief overview of spinal deformities is presented below:

- *Kyphosis* is the excessive outward curve usually in the thoracic region commonly termed as hunchback or humpback. The condition in which kyphosis exceeds a certain range is called hyper-kyphosis whereas the condition in which the kyphosis is below a range is called as hypo-kyphosis. It may occur in the lumbar area as shown in figure 3.4b, where the natural curvature is

found to be disturbed. The yellow dashed line is representing the regular lordotic curve, whereas the red curve is actual kyphotic curve.

- *Scoliosis* is a condition in which person is having side-ways curve once viewed in the coronal plane. It generally takes an 'S' or 'C' curve form as can also be seen in figure 3.4a and figure 3.5a, where the red curve is showing the actual spinal curve once viewed in the coronal plane as opposed to the dashed yellow line which is representing the desired alignment of spine.

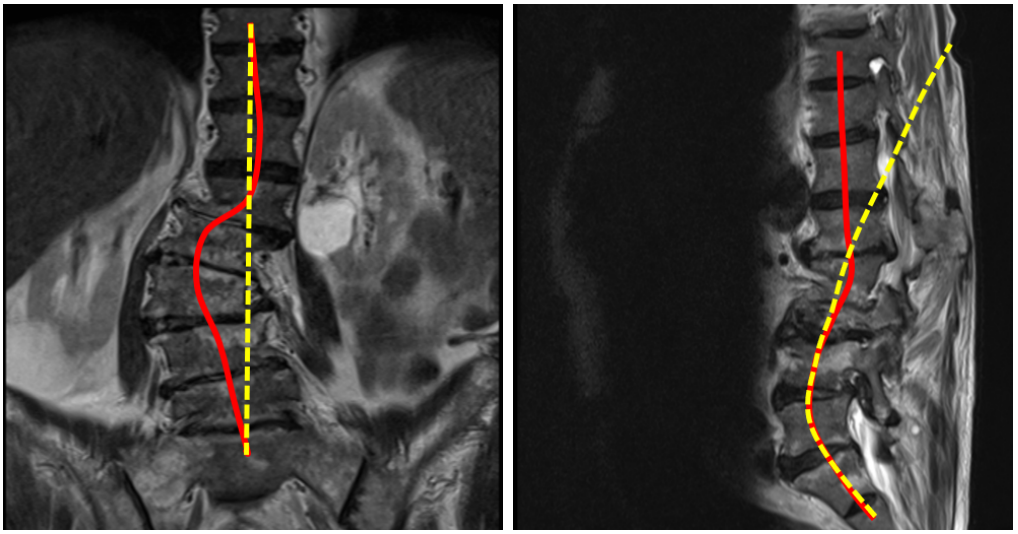

(a) Coronal View (b) Sagittal View

FIGURE 3.4: Kyphoscoliosis in Lumbar Spine.

- *Lordosis* or specifically lumbar lordosis is referred to the inward curve of the lumbar spine. In case, the curve (lordotic curve) exceeds and the lordotic angle becomes large the term is called 'Sway Back' or hyper-lordosis as shown in figure 3.5b. Similarly, if the lordotic angle is too less the condition is termed as 'Flat Back' or hypo-lordosis as shown in figure.

3.5 Clinical Evaluation / Analysis Perspectives

In the previous section, basic anatomical overview 3.2 with common pathological conditions 3.3 of lumbar spine region is explained. This section aims to provide

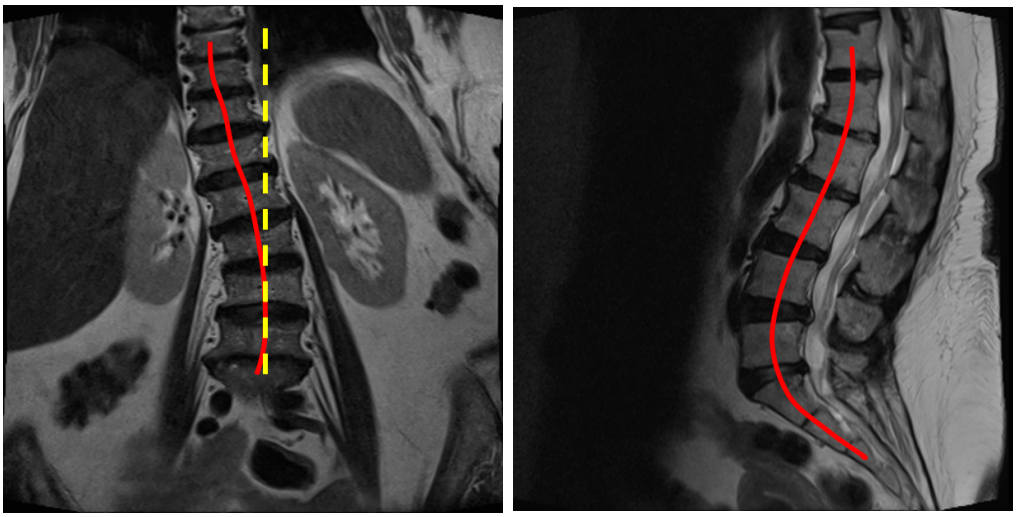

(a) Scoliosis (Coronal View) (b) Hyper-Lordosis (Sagittal View)

FIGURE 3.5: Spinal Alignment Deformities.

preferences of both radiologists and spinal surgeons while performing the evaluation for lower-back pain towards establishing a diagnosis. First, an overview of radiologist is given followed by the overview of spinal surgeon. The significant aspect is that spinal surgeon clinically examines that patient in addition to establishing a correlation with the MRI images. In this thesis, the spinal disorders related to spinal geometry are elaborated in details whereas other pathological conditions related to lumbar spine are briefly overviewed.

3.5.1 Radiologists' Viewpoint

The community of radiology is off the opinion that lumbar spine region is more susceptible to be effected by degenerative changes within the backbone as it is subject to more wear and tear due to impact of most body weight in this region [23, 113, 114]. Furthermore, as per their opinion, the most effected or probable effected region within the lumbar spine is comprising of last three-disc levels L3-L4, L4-L5 and L5-S1 due to the imposition of maximum load stress [104]. The analysis of lumbar spine by radiologist is to identify the region where the spinal disease is present, enabling the spinal surgeons to correctly perform surgical interventional, if required [115]. The diagnosis/analysis report invariably varies based

on the specifics of candidate patient scans; however, a generalized viewpoint is summarized as follows:

While making analysis of the lumbar spine, presence of degenerative disc diseases and related VB deformations are noted by the radiologists being the most common disease present in lumbar spine region [105, 106]. The presence of abnormal wears including spondylosis in VB/IVD or osteoarthritis are also noted. VB End-plate deformations are also observed which may result in formation of bone spur, clinically known as osteophytes, being a significant cause of exerting pressure on the existing nerves. Other clinical findings may include identification of dehydrated IVD [104], disc cracks and herniation [103, 110, 111].

While ascertaining the spinal curvature deformities the clinicians usually resort to X-ray image in sagittal plane for assessment purpose, however, MR images provide much clearer assessment due to the superior image quality [96, 116]. The major spinal curvature deformity which is usually noted in lumbar spine region while analyzing sagittal view is assessment of adequacy or inadequacy in lumbar lordosis. It is experienced that 'Sway Back' or hyper-lordosis is considered one of the main causes of spinal misalignment and backpain [117]. Similarly, hypo-lordosis is also found to disturb the natural curve in lower spine thereby causing problems in load distribution and balancing [118]. It has been experienced that human body tend to tire itself more when its spinal alignment if out of order and may lead to functional disorder [96, 119].

Additionally, the diagnosis may include clinical findings in relation to sciatica , typically pain radiating from back to lower leg, grading of spinal stenosis [120] or commonly termed as narrowing of spinal canal, identification of spondylolisthesis and related disorders.

The review is made by creating a mental map of projecting a three-dimensional projection of lumbar spine by making use of both sagittal and axial slices. For scoliosis candidate subject coronal scan is also included. This multi-planar review enables the radiologist to develop better understanding regarding the structure/anatomy of lumbar spine. In case of any visible abnormality/deformation

specific measurement (if required) is performed. The measurements performed by the radiologist are the only source of establishing correlation once the measurements are performed by spinal surgeons.

3.5.2 Spinal Surgeons' Viewpoint

A spinal surgeon clinically examines the candidate patient and relate clinical findings with the MR scans and the analysis report of the radiologist. Based on the specific symptoms of the patient further physical evaluation is performed. The objective of spinal surgeon is to locate the surgical site with relevance to the present disease and suggest/propose a corrective treatment [121] enabling the subject patient effective restoration of QoL. The treatment can be surgical or non-surgical based on conservative medication [122]. Depending on the severity of spinal disease/disorder, pain threshold and inclination of the candidate patient a suitable decision modality is adopted for specific surgical intervention procedure.

The surgical intervention procedure related to Lumbar Spine can be grouped into two major categories [105, 123, 124]:

3.5.2.1 Lumbar Decompression

The main idea behind a lumbar decompression procedure is to relief the pressure that is exerted by the protruding IVD and yellow ligament towards spinal canal causing stenosis [106, 112]. The procedure involves removal of part of disc or bone and ligament that is causing the compression or narrowing in spinal canal. *Microdiscectomy* [125] involves the removal of part of prolapsed IVD which is the source of compression to the spinal canal. *Laminectomy* [126] is referred to the removal of the part of bone along with yellow ligament that is the main source of spinal stenosis i.e., narrowing of spinal canal.

3.5.2.2 Lumbar Fusion

In lumbar fusion procedure, two adjacent vertebrae are fused or joined together to limit movement between them. This is usually done in patient with painful degenerative IVDs, instability and spinal misalignment. Restoration of spine alignment by correcting lumbar lordosis is also a priority for spine reconstructive procedure. The procedure involves insertion of a bone graft to encourage fusion to restrict the motion at painful or compromised VB segment [127–129].

The types of spinal fusion are narrated below:

- **Posterolateral Gutter Fusion**

  In this method, bone graft is taken either from the pelvis area or substitute bone graft is used and subsequently placed in the posterolateral area which is vascular enabling proper blood flow to the grafted region. Transverse process serves as the muscle attachment site creating requisite tension and muscle packing over the grafted bone [37, 130, 131]. After the surgical procedure, the bone grows naturally and fuses the VBs hence stopping the segmental motion. In some cases, pedicle screws may be used to provide additional support.

- **Posterior Lumbar Interbody Fusion (PLIF) Surgery**

  In PLIF procedure, the vertebral column is approached through posterior end through a three- to six-inch-long incision in the midline. Most commonly it is performed to fuse L4 to L5 or L5 to S1 VBs in case of degenerative disc disease or spondylolisthesis. Laminectomy is performed after removing the left and right sides muscles at multiple levels, enabling visualization of nerve roots. Later, the facet joints are trimmed to create more space for nerve roots, retracting the roots sideways and IVD space is cleaned. A bone graft is inserted in the IVD space which fuses with the superior and inferior VB to form a segment thereby restricting the movement of the joint. The bone graft may be extracted from the pelvis region or the bone removed during

the laminectomy procedure may also be used. Additional support is given by pedicle screws and rods [37, 129, 131, 132].

- **Anterior Lumbar Interbody Fusion (ALIF) Surgery**

  In ALIF procedure the vertebral column is approached to the anterior side of the patient. It may also be combined with posterolateral gutter fusion for more stability [37] in order to provide high degree of stability. The abdominal muscles and blood vessels are retracted sideways thus exposing the spine. The IVD material is removed making space for implant commonly called a cage. Later a bone graft is inserted so that adjacent VB can fuse together restricting the motion of the segment. Additional support may also be given by attaching screws and rods.

- **Transforaminal Lumbar Interbody Fusion (TLIF) Surgery**

  This procedure is similar to PLIF however, both anterior and posterior sides are fused through a single approach in which the posterior side of spine is fused as in done in PLIF however the anterior side is fused by placing pedicle screws rods and bone graft. It avoid the forceful retraction of spinal nerves thereby avoiding damage to the nerve roots [129, 133].

- **Extreme Lateral Interbody Fusion (XLIF) Surgery**

  Unlike in ALIF, PLIF/TLIF in this approach the spine is approached sideways and fusion operation is performed. After the incision, a dilator and retractor is placed directly above the IVD to spread the muscles and tissues. Because of the smaller incision size, it is also referred as Minimally Invasive Spine (MIS) fusion [105]. Muscles and vessels are retracted sideways and standard discectomy is performed. A spacer (cage) is placed in the cleared space followed by the bone graft. Additional reinforcement may be given by placing pedicle screws and rods [37, 128, 134].

3.5.2.3 Non-Surgical Treatments for Lower Back Pain

In other cases, where surgical intervention is avoided certain conservative treatments through medication comprising of pain medication and muscle relaxants [135–137] with specific physical exercises including McKenzie Method [138, 139], pain management through caudal epidural injection [140], acupuncture [141], spinal manipulation through chiropractors [142], thermography i.e., heat therapy [143] may also be recommended.

3.6 Indepth Assessment of Spinal Disorders

Before performing the suitable surgical intervention procedure, the spinal surgeon resorts to detailed evaluation of spinal alignment and spinal balance by performing manual spinal measurements on X-Ray radiograph images and MRI images including lordotic curve angle, lumbosacral angle, pelvic incidence angle, lumbar spine height, IVDs size both at posterior and anterior sides. Thus, in contrast with radiologists' opinion, a spinal surgeon relies on detailed in-depth measurements, as covered in sub-sections 3.6.1, 3.6.2, 3.6.3, in order to ascertain presence or absence of surgical site and severity of spinal disorder for selection of the most appropriate surgical procedure

3.6.1 Assessment of Spondylolisthesis

Spondylolisthesis is a common term for the misalignment of a VB posteriorly or anteriorly due to bone stress fracture i.e., spondylolysis. It has been found that 65 % of cases diagnosed with spondylolysis will develop spondylolisthesis [38]. It was also ascertained that it was developed in the patients in young age i.e., before 16 [144]. Amongst the cases with spondylolysis, majority cases i.e., 90 % lesions were identified at L5 while only 10 % were found at L4 VB [38, 145].

In order to identify spondylolisthesis, clinicians resort to review the patient X-ray image, however, it was found in a research that MRI scans present a much clearer picture for identification of the disorder [146]. For classification of the disorder, Wiltse classification [147] types from type I to type VI are typically used, where the type defines the etiology ranging including congenital, isthmic, degenerative, post-traumatic, pathological and iatrogenic [148]. While performing grading of spondylolisthesis, the clinicians follow Meyerding classification [149] from grade I to grade V at an equal interval of 25 % . In this grading system, the superior end-plate of the VB below the VB under observation is divided into four-quarters depicted by four colored regions in figure 3.6. The grading is based on the slippage of the VB in relation to its position in the specific quarter of posterior-inferior corner [150] e.g., if the VB is within the first quarter of its lower VB counter-part it is graded as grade I, whereas, if the VB is completely slipped i.e., slipped beyond the fourth quarter, it is graded as grade V spondylolisthesis or spondyloptosis [151]. The same information is graphically represented in figure 3.6, where L4 and L5 are under observation for spondylolisthesis. The top-plate of L5 is divided into four quarter depicted in red, magenta, orange and green colors. It can be seen that posterior-inferior i.e., bottom-right corner of L4 lies in second quarter depicted by orange region, thereby, grading as grade II spondylolisthesis of L4 over L5 level.

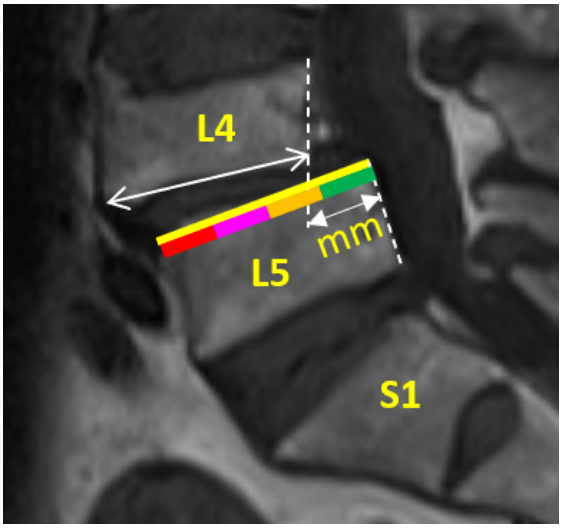

FIGURE 3.6: Assessment of Spondylolisthesis by Clinicians.

3.6.2 Assessment of Lumbar Lordosis

Before actual intervention, the spinal surgeon manually performs certain measurements for developing better understanding of shape and structure of vertebral column. The typical methods include use of computer assisted software, physically measuring dimensions on patient by using flexible rulers[152], inclinometers [86] or spinal mouse [89, 90]. Despite being most significant spine parameter [153], the assessment of spinal curvature is lacking quantitative evaluation as the readings are prone to variation due to observers' manual or semi-automated handling [154].

In clinical practice, optimal lordotic curve range is not fixed and there is variation in LLA in male and female subjects and significant difference is observed in elderly subjects [31, 155–157]. As a general practice lordotic curve should match the pelvic incidence angle with a tolerance of ± 10 deg [31, 158].

Typically, a standing X-ray radiograph is performed for evaluation of lordotic curve followed by manual angular measurements which includes Cobb angle [159] i.e., Modified Cobb Method [160], which has become a standard for evaluating lordotic curve [161, 162] in the sagittal plane [163]. As shown in figure 3.7, θ is the angle of intersection between the perpendicular lines drawn from superior end-plate of L1 and superior end-plate of S1.

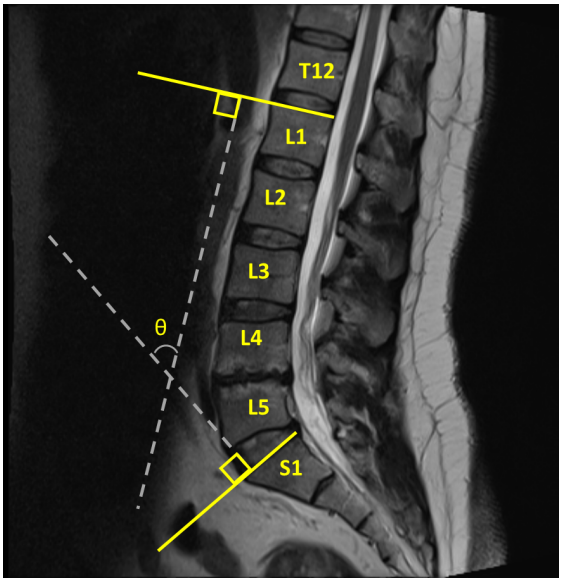

FIGURE 3.7: Modified Cobb Angle θ Measurement Method.

The basic *limitation* of using Cobb method, as reported in a research [164], is the reliance on end-plate structure to measure the angle. In order to overcome this limitation, various other techniques were introduced by medical practitioners. A summary of some of the techniques is presented below:

- **Ishihara Index**

  While computing the Ishihara index, posterior-inferior corners of superior VB i.e., L1 and inferior VB i.e., L5 are connected to form a straight spinal line representing the lumbar spine length. Remaining in-between VBs posterior-inferior corners are connected perpendicularly to the spinal line. The ratio of sum of lengths of perpendicular lines to the spinal length is the measure of Ishihara index [165]. As shown in figure 3.8a, the magenta dotted line represents the lumbar length from inferior posterior L1 corner-point to inferior posterior L5 corner point whereas the red line segments represent the perpendicular lines from the remaining VB inferior posterior corner points to the magenta line. The expression for computing Ishihara index is given $I = \frac{\sum d_i}{L}$ where, L is the lumbar length as depicted by magenta dotted line in figure 3.8a whereas, $\sum d_i$ is the sum of red line segments.

- **Maximum Distance Method**

  In this method, instead of joining the posterior corner-points, anterior-inferior corners of superior VB and inferior VB are connected to form a straight spinal line representing the lumbar height. Maximum orthogonal distance from spinal line and remaining in-between VBs is measured. The ratio of maximum distance and spinal length is measured using $I = \frac{d}{L}$, where, d is maximum perpendicular distance between the anterior inferior corner points shown in red in figure 3.8b to the lumbar height shown in magenta [166].

- **Tangential Radiologic Assessment of Lumbar Lordosis (TRALL)**

  In this method, posterior-inferior corners of superior VB and inferior VB are connected to form a straight spinal line represented by magenta line in figure 3.8c. Maximum orthogonal distance from spinal line and remaining in-between VBs is measured as plotted in red line in figure 3.8c. Superior

VB posterior-inferior point and inferior VB posterior-inferior points are directly connected to the corner-point with maximum distance. The angle of intersection θ is measured[153].

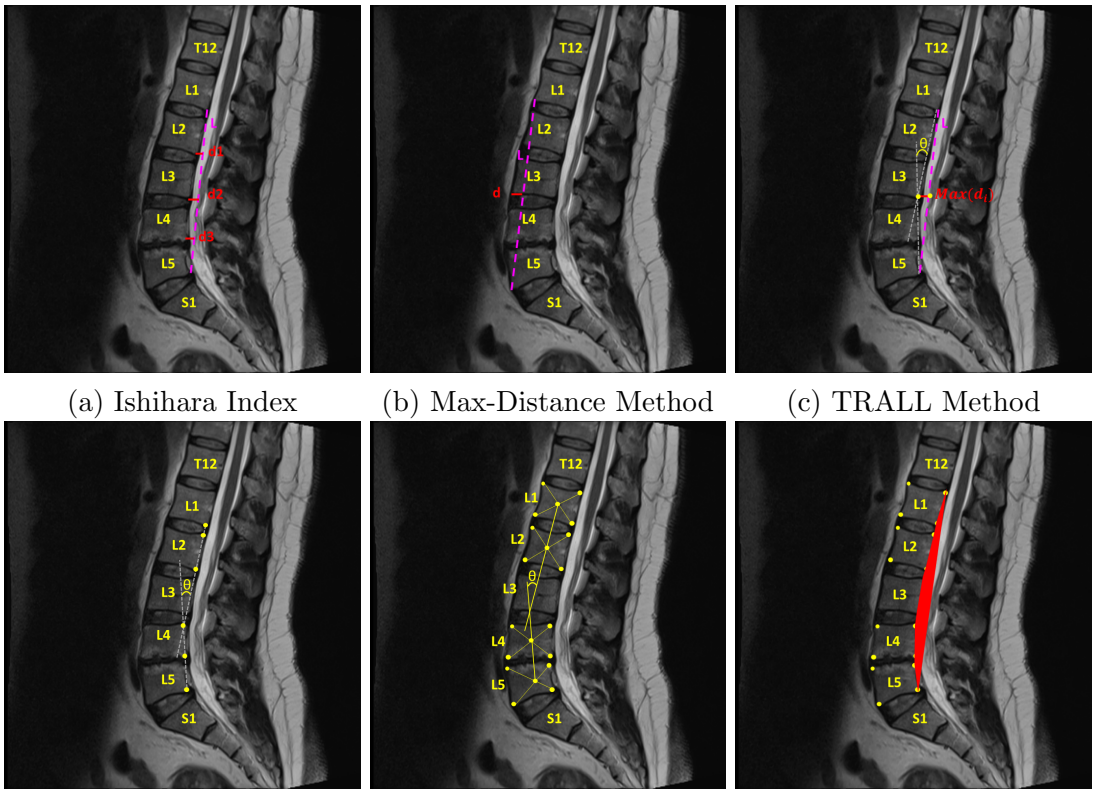

(a) Ishihara Index (b) Max-Distance Method (c) TRALL Method

(d) HPTM (e) Centroid Method (f) AUC Method

FIGURE 3.8: Methods used for Assessment of Lordotic Curve.

- **Harrison Posterior Tangent Method (HPTM)**

  The angle of intersection θ between the tangent lines made by connecting posterior-inferior and posterior-superior corner-points of two superior VBs and posterior-inferior and posterior-superior corner-points of two inferior VBs [160–162]. As shown in figure 3.8d, initially, a line is subtended from the posterior inferior corner points of last two VBs followed by a line from posterior inferior corner points of first two VBs. The angle of intersection θ is the measure of lordotic curve angle.

- **Centroid Method**

  The method proposed by Chen, in which the angle of intersection between

the lines from connecting centroids of two superior VBs and the line connecting two inferior VBs [167]. The opposing corner-points of each VB are joined and centroid is determined as the point of intersection of the opposing lines. The centroids are joined and angle of intersection θ is measured as shown in figure 3.8e.

- **Area Under the Curve (AUC) Method**

  Yang et al. proposed AUC method in which a curve is plotted connecting the posterior corners of lumbar VBs. Afterwards, superior corner-point is connected directly to the inferior VB corner point. Area enclosed in the region is measured [168]. As shown in figure 3.8f, it is evident that this method requires software support to measure the area enclosed in the region of spinal curve.

Quite evidently, these alternate methods are more effort demanding and calculation intensive once compared to modified Cobb angle measurement for assessment of lumbar lordosis [90]. The alternate methods described above, involve multiple measurements, where the Chen [167] centroid method was found to be most calculation intensive hence more reliable [163] and Yang method [168] was calculated through software-assistance and is not measured using manual methods. The reliability and reproducibility of these alternate methods was found to be superior than the modified Cobb method [162, 169].

For the purpose of this research thesis, from clinicians' perspective modified Cobb angle for lumbar assessment is considered for comparison purposes with the the proposed method.

A spinal surgeon while conducting in-depth spinal lordosis analysis, also measures *segmental lordosis angles*, as shown in the figure 3.9a whole lumbar lordotic curve is measured to be 67.6° which is the angle subtended by the superior end-plate line of L1 and superior end-plate line of S1. Whereas in figure 3.9b segmental lordotic angles are measured to be 20.7° at L1-L3 that is the angle subtended by the superior end-plate line of L1 and superior end-plate line of L3. Similarly, the

angle subtended by the superior end-plate line of L4 and superior end-plate line of S1 (L4-S1) is 46.4°. The candidate patient is having scoliosis with significant spondylolisthesis at L4-L5 level.

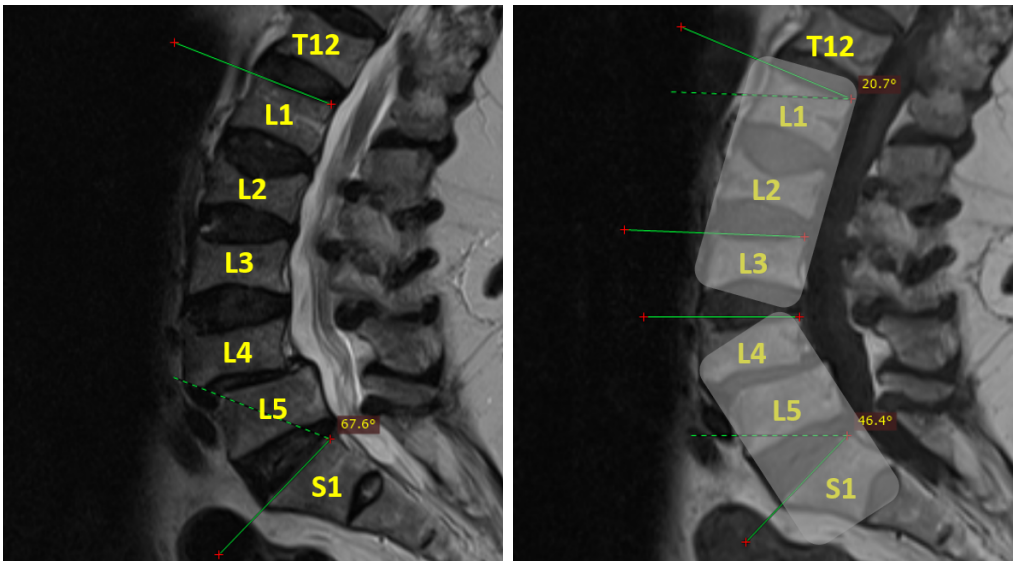

(a) Whole Lumbar Lordosis (b) Segmental Lumbar Lordosis

FIGURE 3.9: Assessment of Lordotic Curve using Cobb Angle.

Lumbosacral angle [170], that is the angle subtended by the inferior end-plate line of L5 and the superior end-plate line of L5, is also measured and shown in figure 3.10.

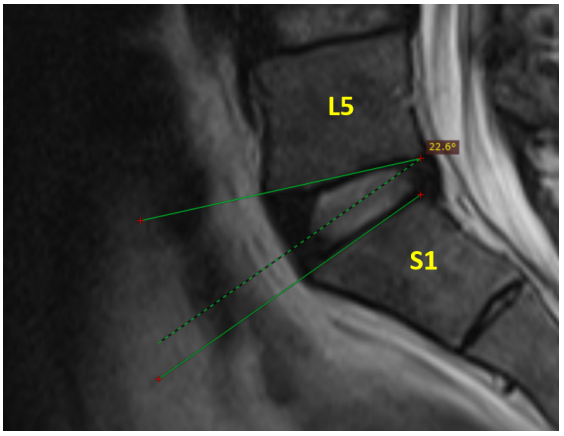

FIGURE 3.10: Lumbosacral Angle (LSA) Measurement.

3.6.3 VB Dimensions and Related Measurements

Additionally, some other important measurements related to VBs dimensions including the VB side walls, VB endplates and IVB distances at both anterior and posterior sides are also performed. These measurements give information about the VB fracture, reduction in space and size of IVD or VB thus enabling the clinician in establishing correlation between the symptoms and clinical findings. The space between adjacent VBs is shown in figure 3.11a, whereas the sidewall dimension is shown in figure 3.11b. Any abnormality in this general trend is also noted thereby making an indication for spinal misalignment or imbalance.

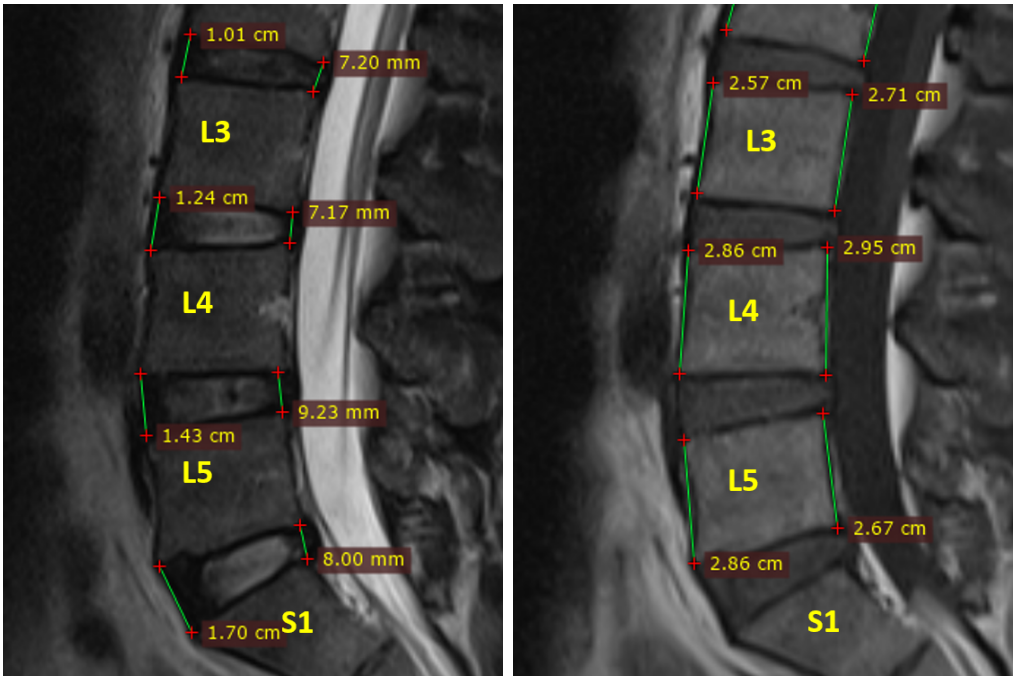

(a) IVB Distance(s) (b) VB Sidewalls Dimension(s)

FIGURE 3.11: IVB Distances and VB Dimensions.

3.7 Summary

- At present, the clinicians rely on manual or software-assisted measurements to assess the spinal disorders.
- Assessment of spondylolisthesis is dependent on the structure of superior and inferior VBs end-plates

- Assessment of lumbar lordosis is performed using modified Cobb angle for calculation of LLA to analyze whole lumbar spine lordosis and LSA to examine segmental lordosis.

- Related spinal measurements including VB dimensions, space between the adjacent VBs are extremely relevant and important spinal metrics to assess the spinal structure.

- A spinal surgeon before selection of appropriate spinal intervention procedures relies on these quantitative measurements to establish a correlation in order to determine the efficacy of surgical procedure usually spinal fusion in alignment restoration i.e., normal lordosis restoration enabling the subject in posture correction.

Chapter 4

Creation of Ground Truth Image Dataset

4.1 Outline

In this chapter the details involved in creation of annotation for lumbar spine mid-sagittal view are presented. The importance of developing a ground truth dataset is also highlighted with the rationale of selection mid-sagittal view for evaluation of spinal related measurements is explained. Like already mentioned in 2.2, the original DICOM dataset[56] comprised of axial labels of IVDs which is not suited to perform VB segmentation, therefore, this manual labeling/annotation is performed.

4.2 Importance of Developing a Ground Truth (GT) Dataset for Lumbar Spine

As correctly highlighted by Weese et al., to make the results of image analysis algorithms and processes reliable with the ability to exhibit reproduceable results, the development of Ground Truth dataset is of paramount importance. With the

huge volume influx of medical imaging data, manual image analysis invariably is a slow process [171]. Therefore, an effort to not only annotate a comprehensive dataset focusing only on sagittal views but also relevant automated spinal measurements extraction is performed in order to support the spinal surgery community, by rendering confidence to their decision regarding surgical intervention procedure.

4.3 Rationale of Selection of Sagittal Views

Mid-sagittal views, presenting maximum information contents regarding spinal alignment, balance and curvature study, are selected in order to perform related spinal measurements including distances between adjacent VBs both posterior and anterior ends, lumbar lordosis curve estimation through lordotic angle. The sagittal views present ample information related to VBs fracture cases, spinal misalignment including spondylolisthesis and spinal deformity cases including hyper-, hypo- and normal-lordosis. Sigurd Berven et al. [30] have also suggested that to understand normal spinal alignment with focus on lordosis, sagittal views present a comprehensive picture, thereby relating the pathophysiology of lumbar degenerative disease to lumbo-pelvic parameters. The axial views present a clearer picture towards establishing spinal stenosis. Together in conjunction with sagittal views present a more precise diagnosis. The use of sagittal plane has been found most adequate for developing the understanding of spinal curvature and postural balance [154, 172].

4.4 Adopted Methodology

For the purpose of this study, 2D images are used instead of 3D volumetric DICOM Images. The dataset used in this study [56], is publicly available, however, formal permission is received from the author to modify and redistribute the dataset for research collaboration. The IVDs are not assigned with labels because proposed

area of study in this research thesis is related to spinal curvature estimation and associated VB measurements. Emphasis is made on the shape and size of VB as well as the distance between each of the VB, keeping in view the area of interest for spinal surgeon.

The dataset is tailored as per the research requirement and preference by selecting 514 out of total 515 images in the dataset. A single scan is dropped as it was found unsuitable for evaluating purpose in sagittal view particularly L1 VB, however presented ample information and details regarding IVDs in axial views. RadiAnt DICOM Viewer by Medixant [173] is used to read the MR DICOM images while Image Labeler Toolbox of MATLAB 2020a, to assign the pixel level labels. The method comprises of three steps involving image extraction, label assignment and label validation as given in the flowchart diagram as given in figure 4.1. The resultant ground truth images are presented in figure 4.3.

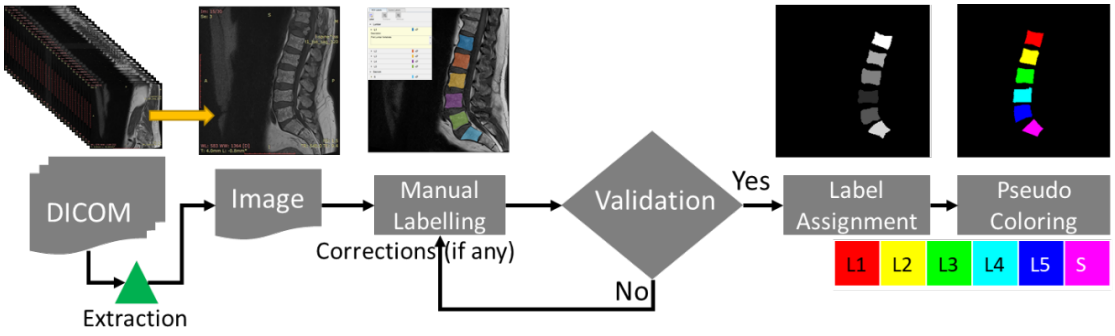

FIGURE 4.1: Process Flowchart (Image Extraction, Labelling and Validation).

4.4.1 Image Extraction

The DICOM images are read using the RadiAnt DICOM Viewer by Medixant as shown in figure 4.2. Mid-sagittal slice is identified by the expert radiologist in order to create the ground-truth image. The identified slice is exported and is stored in a separate folder. Since, the bone presents the same contrast in both T1 and T2 images as shown in the Table 2, therefore, selection of either T1 or T2 images for the purpose of this study is deemed suitable [22]. While extracting the image slices, relevant pixel spacing information is also stored to be used in subsequent

part for scaling the measurements and dimensions. This step is performed to make the dimensions of the measurements relatable to the measurements performed by clinicians.

FIGURE 4.2: RadiAnt DICOM viewer showcasing the sagittal view image of lumbar spine.

4.4.2 Image Annotation

The extracted images are loaded in Image Labeler Toolbox in MATLAB (2020a). The objective is to make the image dataset suitable to perform Semantic Segmentation (later on); therefore, pixel wise ROI labels are defined for 6 x classes for brevity namely, L1, L2, L3, L4, L5, S (since the sacrum bone is fused region). A total of 514 images of mid-sagittal views extracted from DICOM files are labelled in consultation with expert radiologists. Moreover, the region around the vertebral body is plotted using smart polygon/polygon tool whichever gave the most fill. Afterwards, fine-tuning is performed by making use of brush tool to fill the desired regions which were missed by polygon/smart-polygon tool.

4.4.3 Image Validation

The final validation and evaluation of correctness of labelled images are ascertained by expert spinal surgeons. Any incorrectness observed by the spinal surgeon is rectified.

The amount of time consumed (per image on average) in label assignment was around 12 - 15 minutes whereas another 5-7 minutes were consumed on validation and necessary correction. Total images in the dataset are 514.

4.5 Results of Annotation

Out of total 515 images extracted from the DICOM images dataset [56], 514 images are assigned 6 labels from L1 to L5 and S1 while a single image is assigned 5 labels (missing L1 Label). Some of the results are shown in figure 4.3, where the input images are shown in figure 4.3a and the ground truth labels assigned manually are depicted in figure 4.3b. The VBs in pseudo-colored annotated images are highlighted as red for L5, yellow for L4, green to show L3, cyan for L2, blue for L1 and magenta to depict S1. Image overlay result is also shown in figure 4.3c. Image labelling results are validated by expert spinal surgeon as previously explained in 4.4.3.

The images in dataset with relevant spinal measurements details of which are covered in this chapter are shared online [174] after seeking formal permission from the author of the original dataset.

4.6 Summary

- Pixel wise labeling is performed manually with the help of expert clinicians.

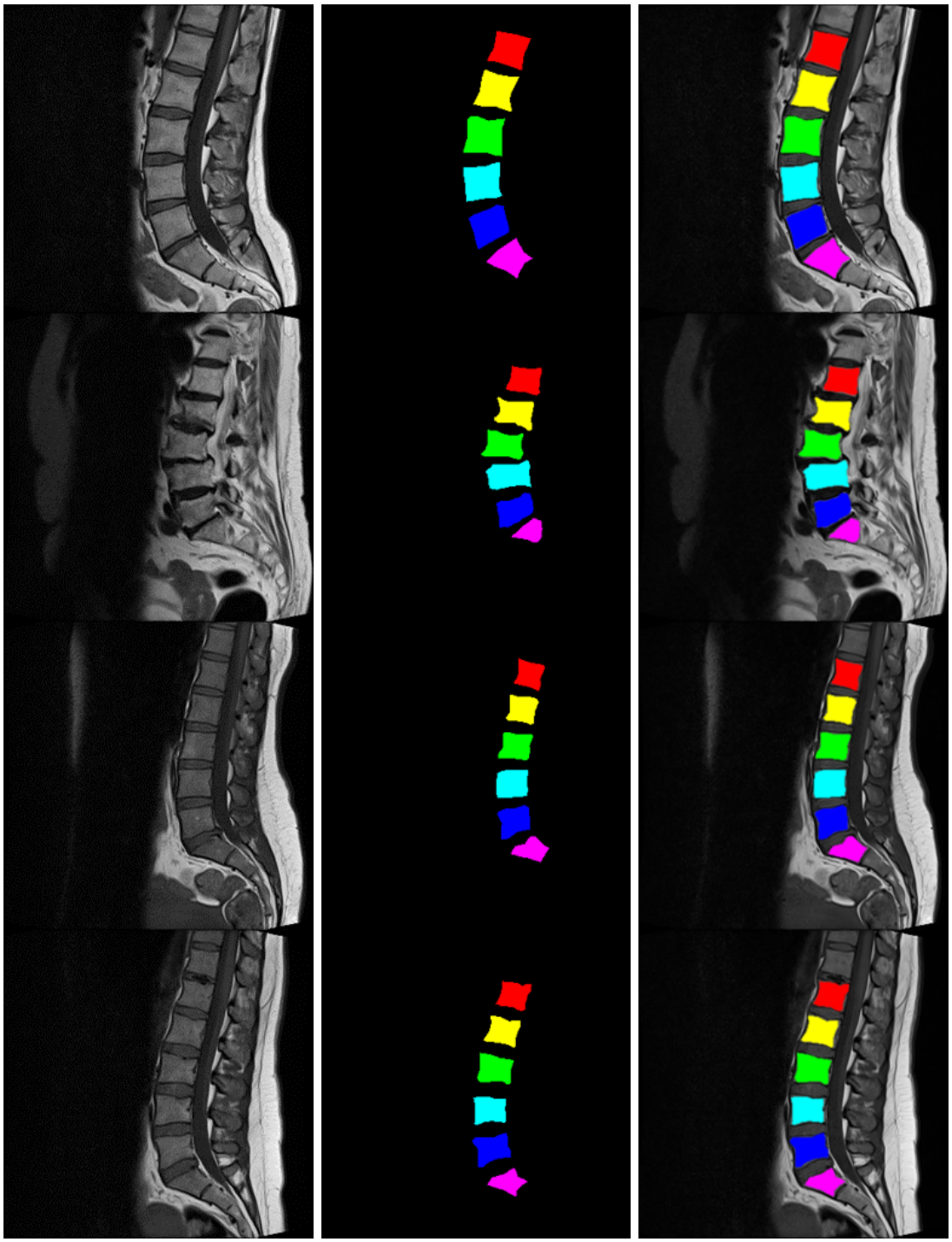

(a) Original Image(s) (b) Annotated Image(s) (c) Overlay Image(s)

FIGURE 4.3: Result of Image Annotation.

- The constructed labels are generated to perform the semantic segmentation task as discussed in 2.2, being the foremost requirement towards establishing an autonomous spinal measurement toolkit.

- As previously highlighted in section 4.2, the importance and relevance of sagittal views towards making spinal geometry analysis, the proposed composite dataset comprising of lumbar spine images, ground truth labels and related spinal measurements may prove useful and effective to develop robust and reliable autonomous spinal analysis toolkit.

- The composite dataset may help to improve the performance metrics in automated application developments by enabling the researchers to draw quantitative correlation between predicted and actual results.

Chapter 5

Vertebral Body Segmentation

5.1 Outline

In this chapter, an improvised algorithm utilizing traditional/conventional methods for image segmentation of lumbar spine VBs is proposed in section 5.2. While experimenting with deep learning methods, first of all networks including deep learning encoder-decoder, scene parsing and fully convolutional networks are utilized to perform the same task with the help of Python. Subsequently, the deep learning toolbox available in MATLAB 2020a is also used to perform the segmentation task on the same dataset. The details of deep learning implementation are covered in section 5.3 of this chapter.

5.2 Proposed Algorithm Conventional Image Processing

The proposed algorithm flow chart is given in figure 5.1 in which the green dotted portion is showing the pre-processing stage, yellow dotted region is the main-framework whereas red dotted region is the post-processing steps. The proposed method is empirically tested to give the best results. Other methods which were

used and extensively tested while developing an algorithm are also discussed in details subsequent section.

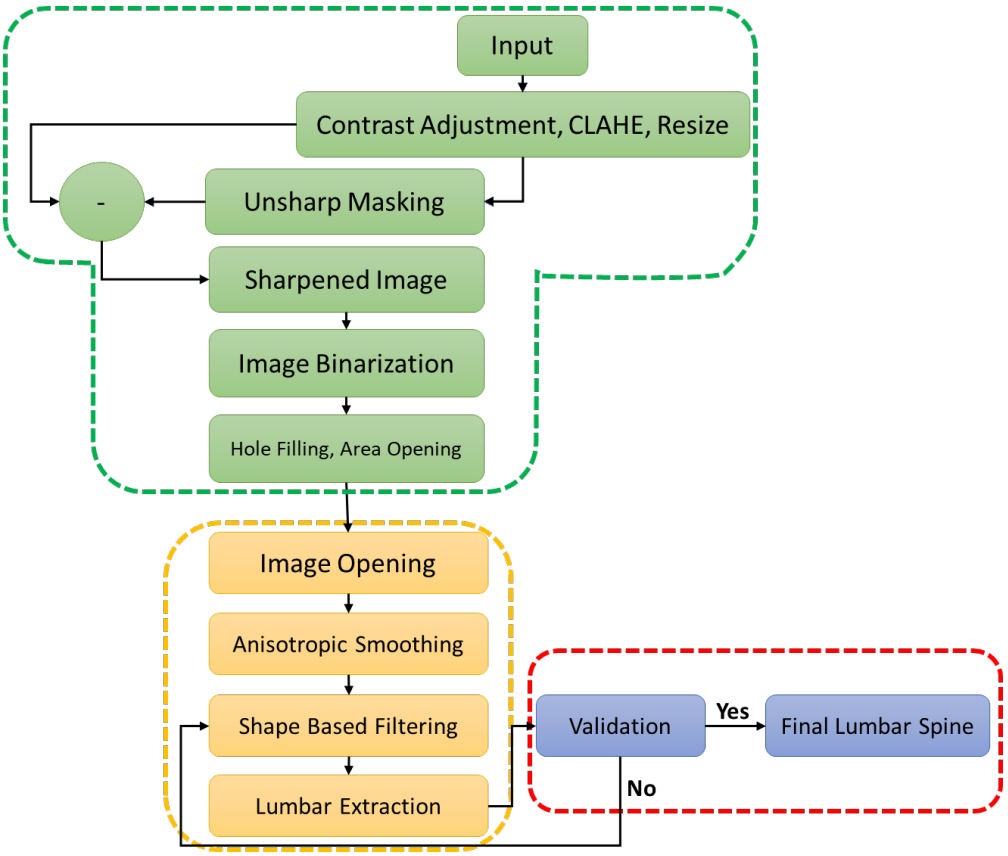

FIGURE 5.1: Proposed Image Segmentation Algorithm using Conventional Image Processing Methods.

5.2.1 Pre-Processing Stage

The pre-processing stage involves three steps including image preparation, image details refinement and image binarization. The details are covered in subsequent sub-sections.

5.2.1.1 Image Preparation

The extracted images (mid-sagittal slice) are picked as input images which are T1 weighted images as shown in figure 5.2a. As previously established that both T1-and T2-weighted images present same information regarding the bone contents

therefore either of them is selected. The RGB image is converted into grayscale image, thereby, reducing the number of channels from 3 to 1. As shown in the figure 5.2b image contrast adjustment is performed by saturating top and bottom one % pixel values thereby increasing the contrast information in the image. Contrast-limited adaptive histogram equalization (CLAHE) [175] is performed, in which instead of whole image, contrast enhancement is done on portions of image normally called as tiles. The resultant image is combined using bilinear interpolation performed on neighboring tiles in order to eliminate artificially induced boundaries. Images are resized to 320 x 320, as most of the images in dataset were of the same size, for uniformity purposes. The resultant prepared image is shown in figure 5.2c.

(a) Original Image (b) Contrast Adjustment (c) Histogram Equalization

FIGURE 5.2: Image Preparation in Pre-Processing Stage.

5.2.1.2 Image Details Enhancement Techniques

Various methods are tried in parallel and the method with empirically best result is selected. A few methods that are being used are as under:

- A 5 x 5, rotationally symmetric *Laplacian of Gaussian (LoG)* [176] is created and the image filtering is performed. The resultant enhanced image is obtained by adding the gradient image (figure 5.3a) to the original image as shown in figure 5.3b.

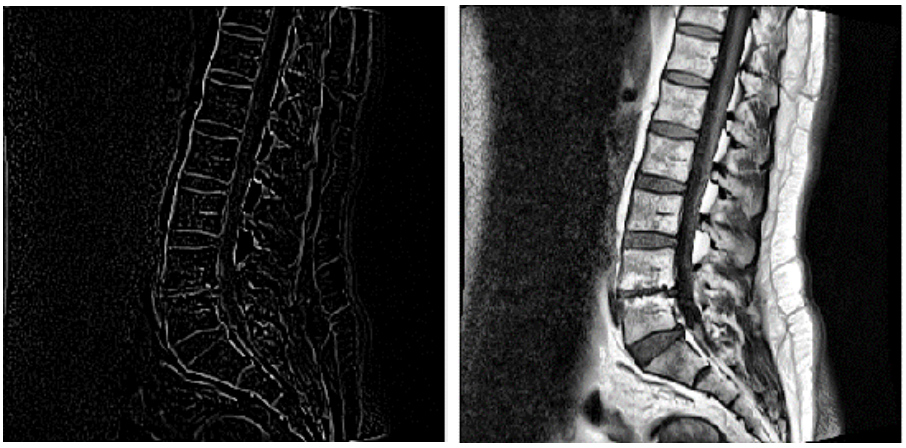

(a) Gradient Image (b) Enhanced Image

FIGURE 5.3: Result of LoG Filter.

- Image is also filtered through *Local Fast Laplacian Filter (LFLF)* [177] as shown in figure 5.4a, varying the amplitude of edges(sigma), smoothing details(alpha) and dynamic range(beta). It was experienced that variation in alpha 0.9 (parameter to control the smoothing details) and beta value greater than 1 (parameter to control dynamic range) enabled edge enhancement, are more suited for these image types.

- Image sharpening through *unsharp masking* [178] as shown in figure 5.4b is also performed in which a sharp image is obtained by subtracting a blurred (unsharp) from itself.

- A normalized custom *edge sharpening* 5 x 5 filter is also created and image filtering is performed. The resultant image obtained is shown in figure 5.4c. In the original work [179], edge enhancement has been performed on fluoroscopic images however in proposed research the objective is to enhance the edges of VBs in MR Images.

The variations showed that the most appropriate results (through visual inspection) for image enhancement for these specific set of images are obtained by making use of image sharpening through unsharp masking filter.

(a) LFLF (b) Unsharp Masking (c) Edge Sharpening

FIGURE 5.4: Result of Image Enhancements.

5.2.1.3 Image Binarization

Following techniques were empirically evaluated:

- *Global Otsu thresholding* [180] is performed on the resultant enhanced image varying the bin size to 16, 32 and 64. It is observed that for computing histogram count, the bin size of *32* is most suited. Otsu Thresholding is performed on the total number of pixels and images are binarized. The resultant images are near to a washed-out images in which various regions of interest are found to have merged with the surrounding pixels depicted in figure 5.5a.

- *Global thresholding* method by making use of gray level thresholding metrics and effectiveness metric is also tested. Normally *64 bins* are used to compute the histogram count and then compute the threshold level. It is also found that neighboring regions are merged as shown in figure 5.5b.

- As suggested by Derek Bradley et al. [181] *Adaptive Thresholding* method for binarization based on the integral image proved to be an effective binarization method. The basic intuition lies in defining a neighborhood window, approximately $1/8^t h$ of the size of image, the pixel under consideration is declared background(black) if it's less than a specific threshold otherwise its declared as foreground (white). Result is displayed as figure 5.5c.

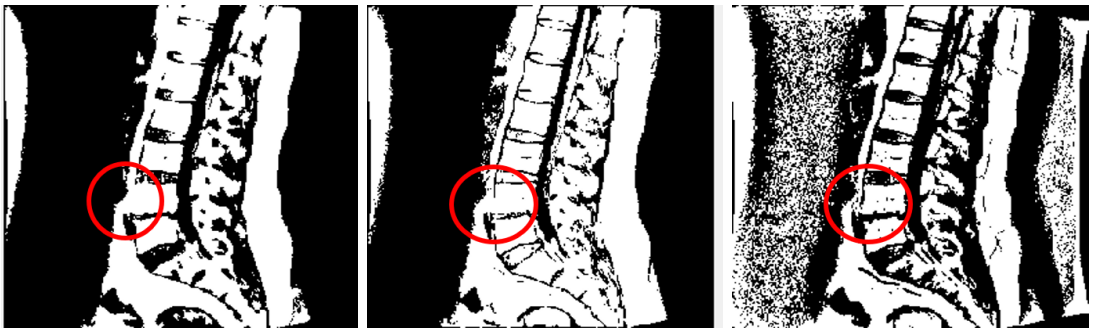

(a) Global Otsu (32 bins) (b) Global Otsu (64 bins) (c) Adaptive Method

FIGURE 5.5: Binarization Results.

Through experimentation and visual inspection Adaptive method proved to give the best results without compromising the desired image details. As evident from figure 5.5c, the region merger issue is comparatively less as compared images obtained through other two methods.

Hole filling operation as shown in figure 5.6a, is performed in order to fill the missing pixels thereby morphologically reconstructing the image, by making use of 8 surrounding neighbors instead of 4 surrounding neighbors. *Area opening* operation is also performed to remove small objects which are undesired. Finally, a binary mask is obtained which is fed to the main framework to perform the segmentation task. The result is shown in 5.6b.

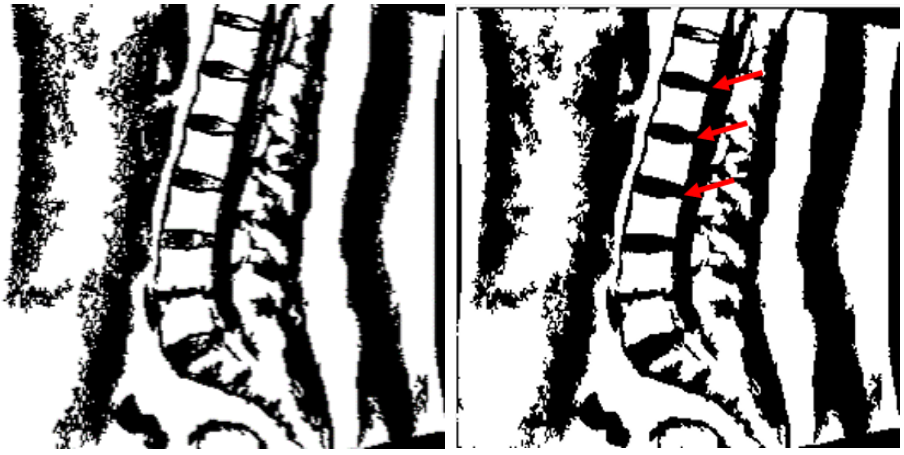

(a) Hole Filling (b) Area Opening

FIGURE 5.6: Binary Mask.

5.2.2 Main Framework

The main framework of the proposed algorithm involves morphological operation to eliminate the region merger problem in the VBs followed by shape restoration. The final part is shape based filtering where the lumbar spine VBs are extracted.

5.2.2.1 Morphological Operation

For performing the morphological operation, *structure elements* (SE) are defined prior performing the image opening operation. Three lines of equal lengths, flat structuring elements, are defined with angular variation as $-15°$, $+15°$ and $80°$. Three diamond structure elements of (7×7), (5×5) and (3×3) are also defined. An arbitrary structuring element of (5×5) is also defined in order to separate or delineate the merged regions thereby making an attempt to restore the edges.

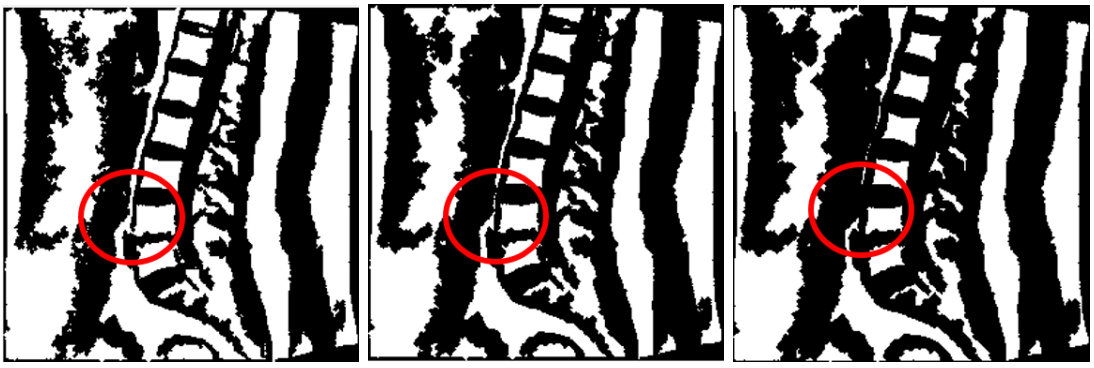

(a) Line SE (b) Diamond SE (5×5) (c) Arbitrary SE

FIGURE 5.7: Reduction in Region Merger.

Image opening [182] operation is later performed and is tested to show similar structural similarity in the reconstructed image for the 5×5, diamond structured element and combination of all three lined structured elements as shown in figure 5.7a,b. However, the arbitrary structuring element showed variation in the resultant image as shown in figure 5.7c. By the use of this morphological operation (image opening), shape restoration of binary masks was enabled thereby addressing the region merger problem, with the reduction in area of the VBs. For addressing the issue, a smoothing operation was applied details of which are covered subsequently.

5.2.2.2 Image Smoothing

Anisotropic filtering is considered very useful in edges preservation and keeping the shape intact [183]. The technique basically involves computation of distance transform followed by anisotropic smoothing. The expression is given as under:

$$C(x,y)_t = e^{(-\frac{\|\nabla i\|}{\rho})^2} \tag{5.1}$$

where, $\|\nabla i\|$ represents the image gradient, ρ is the parameter to control the sensitivity of the edges, x and y shows the spatial coordinates while sub-script t shows the iteration count i.e., 30 iterations. The resultant binarized image as shown in figure 5.8 is a smooth image which is showing high correlation with the original image in which the region merger issue existed. The main benefit of anisotropic smoothing is the preservation of edges.

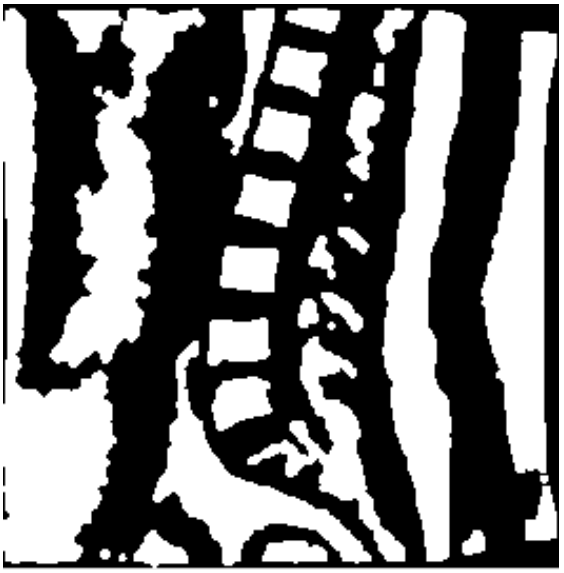

FIGURE 5.8: Preservation of Edges in Image using Anisotropic Filtering.

5.2.2.3 Extraction of Vertebral Column

The resultant binary image is assigned with labels, for further evaluation of region properties in order to extract the relevant lumbar spine VBs. Thresholding on *Area* is performed in order to filter the larger bodies not fitting the description

of VB. Here perimeter filtering is also tried but the results are more accurate in filtering larger undesired objects based on Area thresholding. Irregular Elongated shapes are filtered based on *major-axis* and *minor-axis* thresholding. Thresholding is performed based on the ratio of major and minor axis and simply the ones less than the threshold value are kept.

After filtering the undesired regions, lumbar spine extraction sequence is executed involving filtering based on the sub-image properties involving *extent*, *circularity* and *solidity*.

Measure of *Extent* proved to deliver the most accurate results to segment out lumbar VBs. The calculation of extent of sub-image region involves taking a ratio of total pixel area with the pixel area of smallest possible rectangular bounding box that can be defined around that region. In MATLAB, bounding box is rectangular shape with 4 parameters. The first and second being the co-ordinates of top-left corner of the region and third being the width whereas the height is specified in the fourth parameter.

Circularity property which is the measure of roundness of the region/object was also experimented. In this case it was found that circularity property didn't return good results in segmenting out the VBs. Also, it was observed that circularity is not a good measure while evaluating very small regions as most of the smaller regions are falsely returned with maximum circularity score.

5.2.3 Post-Processing including Validation

The details of post-processing being the final step are covered in this section. The resultant segmented image is checked for the number of VBs content based on the lumbar spine. The desired number of VBs are six from L1 to L5 and first sacrum bone. The visual result of proposed algorithm is given in figure 5.9, where pre-validation and post-validation results are shown. Pseudo colored images are also highlighted in order to present better depiction. The quantitative results are presented in table 8.1.

Algorithm 1: VBSeg - Vertebral Body Segmentation

Input: Original Image I
Output: Extracted Image I_{VB}
$I_c \leftarrow$ ContrastAdjustment(I)
$I_h \leftarrow$ CLAHE(I_c)
$I_s \leftarrow$ UnsharpMasking(I_h)
$I_b \leftarrow$ Binarization(I_s)
$I_b^f \leftarrow$ ImageFill(I_b)
$I_b^{f,a} \leftarrow$ AreaOpening(I_b^f)[RejectArea = *Area*$< \tau$]
$I_b^{f,a,o} \leftarrow$ ImageOpening($I_b^{f,a}$)[*5x5, Diamond Structure Element*]
$I_b^{f,a,o,s} \leftarrow$ Smoothing($I_b^{f,a,o}$)[*Anisotropic*]
$I_{VB}^{pv} \leftarrow$ ShapeFilter($I_b^{f,a,o,s}$)[$\rho \leftarrow$ *Extent, Area,*MA/mA]
for $I_{VB}^{pv} \neq I_{VB}^{v}$ **do**
    $nVB \leftarrow$ CountVB(I_{VB}^{pv})
    if $nVB = valid$ **then**
        $I_{VB}^{v} \leftarrow (I_{VB}^{pv})$
    else
        if $nVB = invalid$ **then**
            ShapeFilter($I_{bw}^{f,a,o,s}$)[$\rho \uparrow$ if $nVB < valid$,$\rho \downarrow$ if $nVB > valid$]
        end
    end
end
$I_{VB} \leftarrow I_{VB}^{v}$

A validation check is performed to count the number of VBs detected in the image. For this purpose, all the labelled regions centroids are computed using the region properties. The centroids are sorted based on the y-direction. The size of the input image is *(320, 320)* therefore, the center pixel coordinate is *(160, 160)*; this center pixel coordinate is picked as first centroid. The distance of all the centroids from the first pixel coordinate is calculated and the minimum distance index pixel coordinate are assigned to the first point pair.

After having the first centroid correctly identified, remaining centroids are identified based on minimum distance between the consecutive points. Two subsequent checks are performed in order to calculate the superior VBs and the inferior VBs, till the number of objects detected in the image are six i.e., for L1-L5 and S1 or seven for L1-L5, S1 and T12. In case the number of VBs are not meeting the desired criteria shaped based filtering was performed with variation in the region

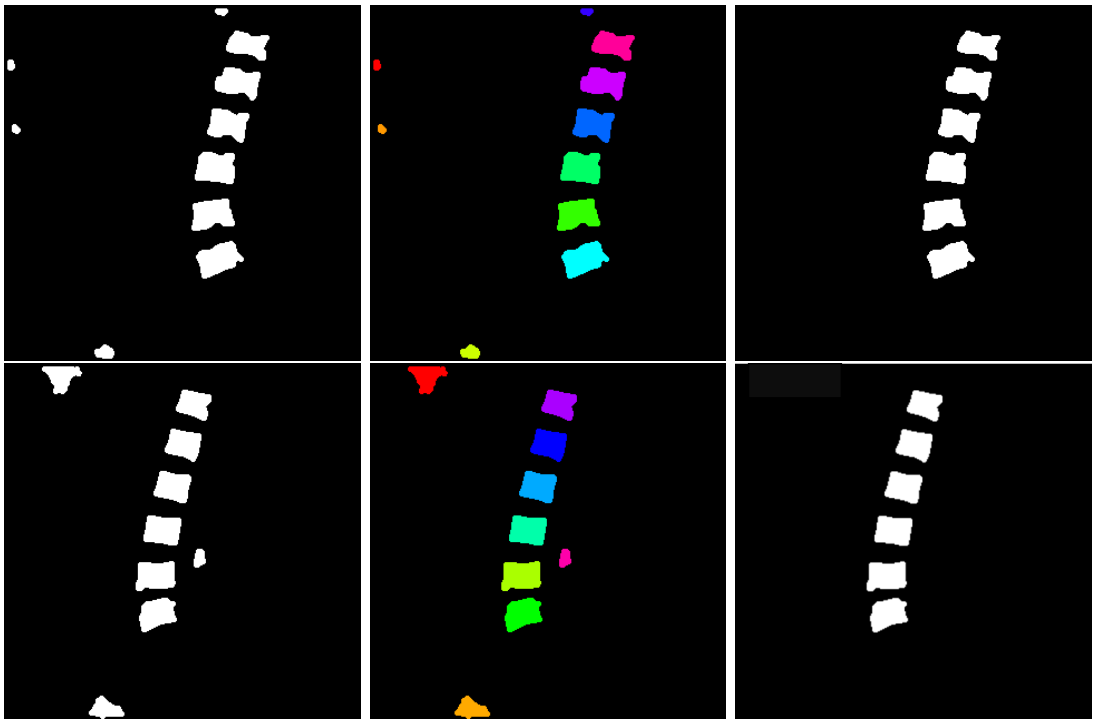

(a) Pre-Validation (b) Pseudo-Colored (c) Post-Validation

FIGURE 5.9: Result of VBSeg Algorithm.

property till the image returns desired output. The pseduo-code for algorithm is given as algorithm 1 whereas the flow diagram is given in figure 5.1.

5.2.4 Experimentation with Other Methods

A brief overview of other experimented methods including Gabor Filter, Radon Transform and Active Contours algorithm is presented in appendix A.

5.3 Segmentation using Deep Learning Architecture(s)

In order to address the computer vision problems, conventional or traditional image segmentation techniques have certainly shown promising and desired results over the last few decades, however, with the onset of deep learning and making use of neural networks to address the segmentation related tasks have easily surpassed

the results both in qualitative and quantitative aspects. After performing extensive testing by making use of traditional image processing techniques and proposed a customised algorithm (5.1) to perform the medical image segmentation task, deep learning methods were tested for executing the same task. Before getting into the details of implementation it is imperative to develop understanding of selected deep learning architectures with reference to their suitability for a specific task. In the subsequent sub-sections, brief overview of deep learning architectures and the preference with user point of view is presented.

5.3.1 Deep Network Architectures Overview

As already covered in the literature review section, many researchers have strongly advocated the use of deep learning methods to perform segmentation tasks [184–188]. For the purpose of this research thesis, vertebral column segmentation is performed using conventional deep learning encoder-decoder, scene parsing and mobile networks. A comparison is also drawn amongst multiple popular models such as UNet [58], ResNet [189], SegNet [82], PSPNet [83], and MobileNets [190]. A concise description of the models is given as follows:

- **UNet**

  Originally inspired by Fully Connected Network (FCN)[191], UNet has a contraction path and an expansion path. The contraction path, of traditional convolutional neural network (CNN) and max pooling layers, preserves contextual information while the expansion path localizes information through transpose CNN. Like in ResNet, UNet also concatenates features by providing skip connections from contraction to expansion path. It has a built-in data augmentation scheme hence very well suited for limited data cases[58].

- **ResNet**

  Residual Networks or ResNet solved the issue of vanishing gradient descent by introducing skip connections, thereby increasing flexibility and offering better preservation of contextual information [189].

- **SegNet**

  Segmentation Network (SegNet) based on encode-decoder architecture, where the encoder part preserves the contextual information and decoder part uses the max-pooling indices computed in encoder part to up-sample the feature-map non-linearly. It is computationally efficient once compared to UNet, owing to its lesser number of trainable parameters[82].

- **PSPNet**

  The pyramid scene parsing network makes use of pyramid pooling module to capture global contextual information, coarser to finer, in four-pyramids level. The feature-maps are up-sampled by decoder to present segmented result [83].

- **MobileNets**

  MobileNets is based on depth-wise separable convolution hence, offering reduction in size of model. It is suited for implementation in embedded systems and mobile applications on the fly due to lesser size and comparable accuracy [190].

All the models are trained and tested on Intel(R) Xeon(R) Silver 4110 CPU with 64 GB RAM and NVIDIA Quadro P4000 GPU, using Tensorflow Keras API, Python 3.7.9. For comparison purposes, MATLAB deep learning toolbox is also used with the same hardware configuration, summary of which is given in appendix B.

5.3.2 Choice of Optimizer

The role of optimizer is noteworthy to mention to correctly optimizing the weights in order to make correct predictions for future unknown samples. Together, with loss function, the model parameters are updated to reshape the network as accurate as possible. In order to vary the learning rate, to achieve better convergence, adadelta [192] optimizer is used in this research. It optimizes the weights adaptively as suggested by the name, through weighted exponential method. Here, it

is important to review the weights update rule as it will enable the reader in developing understanding why adadelta optimizer is used. A summarized version of transition from standard weight update rule in case of stochastic gradient descent to adadelta is presented below. Typical weight update equation is given below

$$w_t = w_{t-1} - \eta \times \left(\frac{\partial L}{\partial w_{t-1}} \right) \tag{5.2}$$

where, w_t represents updated weight, w_{t-1} shows the previous weight, η is the learning rate and $\frac{\partial L}{\partial w_{t-1}}$ is the gradient of loss function with respect to weight at *t-1* instance. The expression $-\eta \times \left(\frac{\partial L}{\partial w_{t-1}} \right)$ is denoting Δw_{t-1} i.e., the update factor.

As observed, the learning rate η remains constant throughout this weight update process, hence the step size while approaching towards the global minima is not changed.

In order to vary the step size, the learning rate η is reduced gradually so that initially larger steps taken to approach the global minima are reduced to smaller steps, thereby decreasing the time to converge to the global minima. Hence, the updated equation Adagrad [193] short for adaptive gradient is presented below

$$w_t = w_{t-1} - \eta' \times \left(\frac{\partial L}{\partial w_{t-1}} \right) \tag{5.3}$$

where, η' is the updated or changed learning rate for every iteration. The expression for η' is given as

$$\eta' = \frac{\eta}{\sqrt{\alpha_t + \epsilon}} \tag{5.4}$$

here, α_t is the dynamic update factor to subsequently update the learning rate η by accumulating the squares of gradient as the training process grows. It is pretty much possible that value of α_t becomes *zero* during the training process, therefore, in order to avoid dividing the previous learning rate η with *zero*, a small positive number ϵ is added. The expression for α_t is given below

$$\alpha_t = \sum_{i=1}^{t} \left(\frac{\partial L}{\partial w_i} \right)^2 \tag{5.5}$$

However, there is drawback with squared accumulation of gradients as during the course of training process α_t becomes very large and the updated learning rate become smaller and smaller such that it become infinitesimally small, hence the weight update will have no change. This results in halt in converge to the global minima.

The researchers [194] in RMSprop short for root mean square propagation, proposed that in order to avoid this halt and to restrict α_t values to become large, instead of squared accumulation of all the gradients, weighted accumulation is used, thus preventing the value of α_t from becoming large and resultantly avoiding the halt. The expression for learning rate update is given as

$$\eta' = \frac{\eta}{\sqrt{\gamma_t + \epsilon}} \tag{5.6}$$

where, Where, instead of α_t, i.e., squared accumulation of gradients, γ_t is used which is weighted squared accumulation of gradients. The expression for γ_t is given as

$$\gamma_t = \beta \times \gamma_{t-1} + (1 - \beta) \sum_{i=1}^{t} \left(\frac{\partial L}{\partial w_i} \right)^2 \tag{5.7}$$

Where, β hyperparameter, typically ranges from 0.90 – 0.95, ensures that γ_t doesnot become large enough. The comprehensive expression for weight update becomes as follows:

$$w_t = w_{t-1} - \frac{\eta}{\sqrt{\gamma_t + \epsilon}} \left(\frac{\partial L}{\partial w_{t-1}} \right) \tag{5.8}$$

Another major contribution was making the update formula independent of learning rate η which is proposed in Adadelta [192]. The expression is given as

$$w_t = w_{t-1} - \frac{\sqrt{\Delta w_{t-1} + \epsilon}}{\sqrt{\gamma_t + \epsilon}} \left(\frac{\partial L}{\partial w_{t-1}} \right) \tag{5.9}$$

where, the expression for Δ_{t-1} is given by

$$\Delta w_t = \zeta \times \Delta w_{t-1} + (1-\zeta)\left(\frac{\sqrt{\Delta w_{t-1}+\epsilon}}{\sqrt{\gamma_t+\epsilon}}\left(\frac{\partial L}{\partial w_{t-1}}\right)\right)^2 \tag{5.10}$$

where, ζ enables exponentially weighted selection, typically in the range of 0.90 - 0.95, of change in weights of parameters, thus there is no need to select the default learning rate η.

5.3.3 Cross-Entropy Loss Function

To measure the performance of classification model, cross entropy loss function is used. Simply, the loss function will increase when the predicted label diverges from the actual class label. The expression for cross entropy loss function is given below

$$l(\theta) = -\sum_{i=1}^{n} y_i \log \psi_i + (1-y_i)\log(1-\psi_i) \tag{5.11}$$

where, θ represents the parameters of model, y_i is the actual class label, ψ_i is the predicted class label.

5.3.4 Application of Fine-Tuning

The most common and popular and common scheme of training the model being widely used is fine tuning. In this research fine tuning is performed various encoder-decoder configurations by combining networks including ResNet-PSPNet [195], MobileNets-UNet [196], VGG-UNet [197], ResNet-UNet [198], ResNet-SegNet [185] and others. The process of fine tuning may be divided into four steps as shown in figure 5.10:

- Picking a pre-trained model on a source dataset like ImageNet, let us call it the source model.
- Defining a model replicating the layers and parameters of course model however, last layer i.e., output layer is clipped.

- Defining a new output layer with desired number of classes as per the custom dataset and randomly initializing the parameters of the output layer. Appending of layer with the defined model
- Perform training of defined model on the custom dataset from scratch. Updating the parameters of last layers while fine tuning the rest of layers parameters.

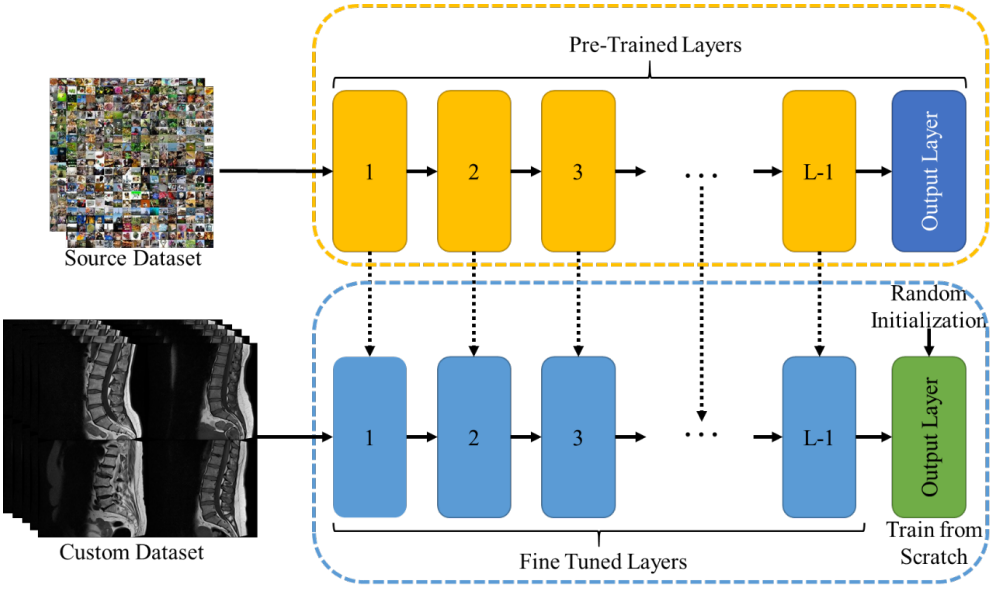

FIGURE 5.10: Transfer Learning through Fine Tuning Process.

The total number of *epochs* for training; using fine tuning, are *50* with the *batch size* of *2* images. It was found that *training time* is least for MobileNets-SegNet i.e., an average of 42.2 seconds per epoch, whereas the most for VGG-UNet i.e., an average of 465 seconds per epoch. The best *performance* for VB extraction is achieved by ResNet-UNet.

5.4 Summary

- A carefully worked-out VB segmentation algorithm (VBSeg) based on traditional image processing techniques is proposed after extensive empirical evaluation.

- Amongst the tested methods, deep learning network with ResNet as base model and UNet as classification network gave the best results to segment out the VBs.
- MobileNets have the lowest training time as compared to other networks. In performance metrics, MobileNets was also on the lower shade. Therefore, the researchers have to encounter a trade-off between complexity and accuracy while choosing MobileNets.
- Fine tuning method for transfer learning is an effective learning mode well suited and less time consuming.

Chapter 6

Automated Measurements of Lumbar Spine

6.1 Outline

After performing the segmentation task, automated spinal measurements on the segmented VBs are performed which ranges from angular measurements to distance measurements. These measurements are clinically relevant in order to correlate the findings of clinicians with symptoms in the subject patient, as already established in section 3.6. Initially, the distance related measurements are discussed followed by angular measurements, whereas the spine curve estimation is covered at the end of the chapter.

6.2 Proposed Methodology

In this research thesis, completely automated measurements (without human intervention) related to lumbar spine region by using MATLAB2020a, are performed two times involving the steps as shown in the flowchart presented as figure 6.1 which is explained in algorithmic form in algorithm 2. In the first measurement sequence, ground truth labels which are manually created as covered in chapter 4

are used in order to complement the images with quantitative attributes, forming part of composite dataset. The same dataset is publicly shared for research collaboration [174]. In the second measurement sequence, the automated segmented images with best quantitative results, in this case ResNet-UNet, are used to perform spinal measurements to establish correlation with the measurements obtained on the ground truth labels.

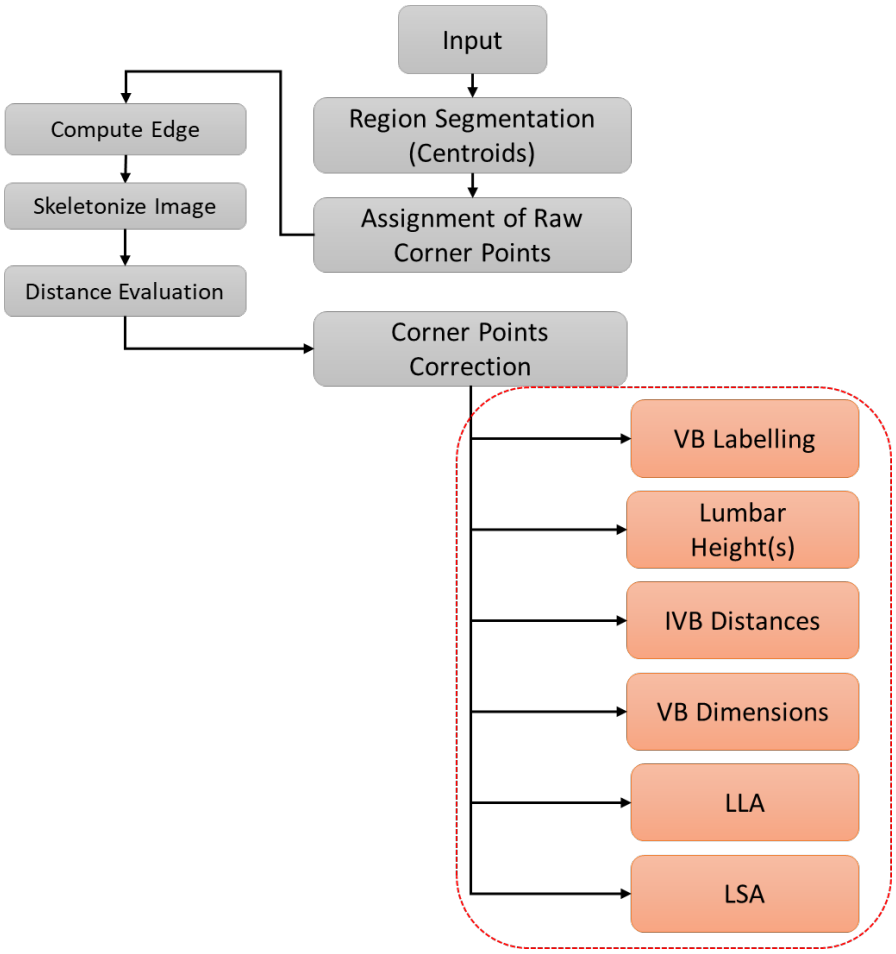

FIGURE 6.1: Spinal Measurements Acquisition (Block Diagram).

6.2.1 Identification and Labelling of VB

As a first step, region segmentation is performed in order to isolate the individual VB. Identification of VBs is performed by making use of region properties and extraction of respective centroids. Result subsample comprising of 4-images is

Algorithm 2: Spinal Measurements Extraction Scheme

Input: Extracted Image (I_{VB})
Output(s): $LH_{cp}, LH_{cen}, IVB_i^a, IVB_i^p, VB_i^p, VB_i^a, LLA, LSA$
for $\forall\ VBs$ **do**
    $cen_i \leftarrow \text{ComputeCenter}(I_{VB})$
    $cp_{i,d}^{raw} \leftarrow \text{CornerPoint}(cen_i)[d = T_L, T_R, B_R, B_L]$
    $cp_{i,d} \leftarrow \text{CorrectionCP}(cp_{i,d}^{raw})[Edge, NN]$
end
$LH_{cp} \leftarrow \text{LumbarHeight}(cp_{i,T_L}) \leftarrow [L1_{T_L}, S1_{T_L}]$
$LH_{cen} \leftarrow \text{LumbarHeight}(cen_i) \leftarrow [L1, S1]$
$IVB_i^a \leftarrow \text{Distance}(cp_{i,B_L,T_L}) \leftarrow [L_{i_{B_L}}^a - L_{i+1_{T_L}}^a]$
$IVB_i^p \leftarrow \text{Distance}(cp_{i,B_R,T_R}) \leftarrow [L_{i_{B_R}}^p - L_{i+1_{T_R}}^p]$
$VB_i^a \leftarrow \text{Distance}(cp_{i,T_L,B_L}) \leftarrow [L_{i_{T_L}}^a - L_{i_{B_L}}^a]$
$VB_i^p \leftarrow \text{Distance}(cp_{i,T_R,B_R}) \leftarrow [L_{i_{T_R}}^p - L_{i_{B_R}}^p]$
$LLA \leftarrow \text{ComputeAngle}(cen_i, cp_{i,d}) \leftarrow [L1_{T_L,T_R}, S1_{T_L,T_R}]$
$LSA \leftarrow \text{ComputeAngle}(cen_i, cp_{i,d}) \leftarrow [L5_{B_L,B_R}, S1_{T_L,T_R}]$

showcased in figure 6.2. Labels are assigned from L1-L5 for lumbar VBs and S1 to the first sacrum VB. $*$ represents the centroids.

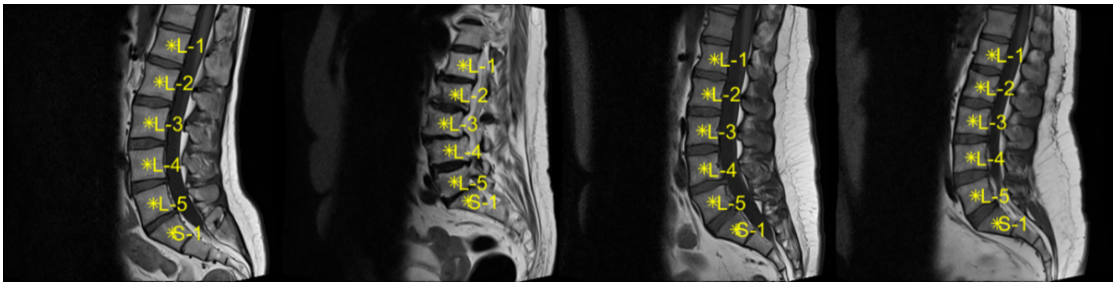

FIGURE 6.2: VB Identification and Labelling.

6.2.2 Computation of Corner Points

The most challenging part was the computation of 4 corner points, which involved raw corner-point assignment and refinement processes as shown in the flowchart given in figure 6.1. In raw assignment, initially, a bounding-box which is the smallest possible rectangular box which can be overlayed on the individual VB is computed. The four corners of rectangle are assigned as raw/initial corner points of VB. Here, it is noteworthy to mention that the bounding-box is drawn parallel to the image horizontal axis irrespective of the orientation of the object around which

it is drawn. While refinement is performed in order to match the initial corner point assigned to the actual border pixel of the VB. For that purpose, image is skeletonized and non-zero entries are enlisted. The distance is computed for each corner-point, say superior-left, superior-right, inferior-right, inferior-left, from the non-zero list of coordinates. The lowest distance pixel-coordinate is assigned to the respective corner-point. The expression is given as follows:

$$d_{\tau,i} = \sqrt{p_{\tau}^2 - p\prime_i^2} \tag{6.1}$$

where, p_τ represents the raw corner-points assigned by the corners of bounding box and the sub-script τ depicts the four-corner points namely superior-left, superior-right, inferior-right, inferior-left, $p\prime_i$ shows all the non-zero pixels of a particular VB, $d_{\tau,i}$ shows the distance matrix for all four corner points. Finally, the minimum distance pixel index as given in equation 6.2 is stored and the coordinate corresponding to the index is assigned to the respective corner-point p_τ.

$$idx = \min\left(d_{\tau,i}\right), p_\tau \leftarrow p\prime_{idx} \tag{6.2}$$

6.2.3 Distance Related Measurements

After calculation of 4 corner points, *lumbar height* is computed based on the Euclidean distance using two different approaches. In the first method, distance between L1 superior-anterior corner point and S1 superior-anterior corner-point as shown with green line segment in figure 6.3a. In the second method, the lumbar height is measured from centroids between L1 VB and S1 VB as depicted by the yellow line segment in figure 6.3b.

Intervertebral body distances (IVB) i.e., distance between consecutive VB at anterior and posterior sides is also measured. While computing the distances at anterior side of the spine, the distance between anterior-inferior corner point and

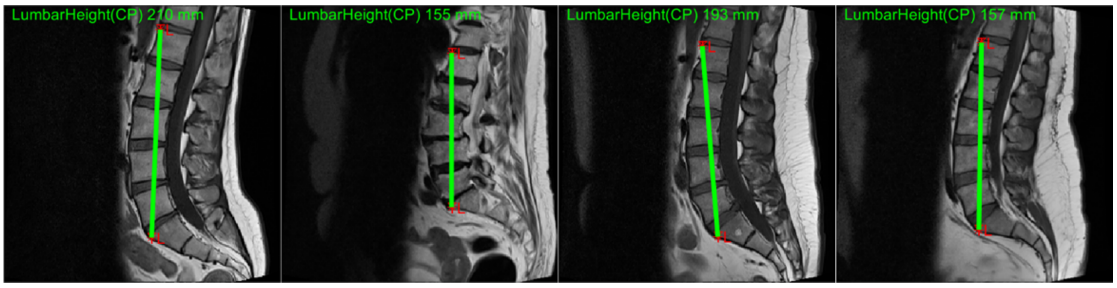

(a) Measured between L1-S1 Anterior-Superior Corner-Points.

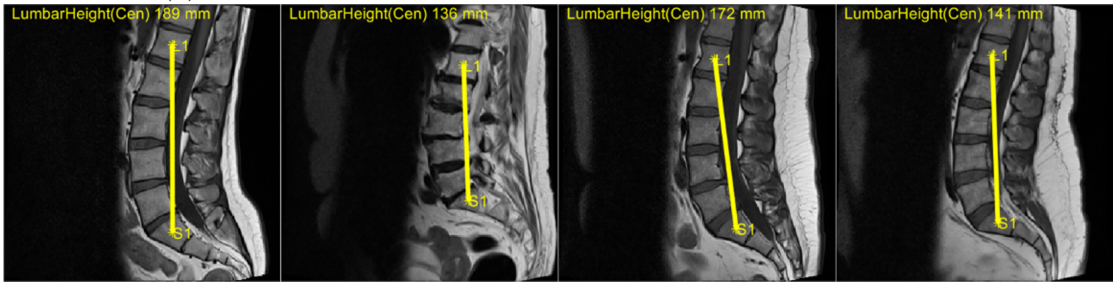

(b) Measured between L1-S1 Centroids.

FIGURE 6.3: Calculation of Lumbar Height in *mm*.

anterior-superior corner point of consecutive VB is measured. Similar measurement is performed for posterior sides as shown in figure 6.4a). Here, the measurements represented in red are anterior side measurements, whereas the posterior side measurements are given in green font.

Likewise, the *VB dimension* are measured at anterior and posterior sides such that the distances between the superior and inferior corner points are measured in the same VB as depicted in figure 6.3b. A failure case (2^{nd} sub-image from right) is also showcased in figure 6.3 labelled in yellow, where the computation error is due to the misalignment of corner point. All the distance related measurements are calculated using the expression given in equation 6.3 for Euclidean distance given below

$$d = \sqrt{(x_2 - s_1)^2 + (y_2 - y_1)^2} \tag{6.3}$$

In both cases, the lumbar height(s), IVB distances and VB dimensions are measured in millimeters *mm*.

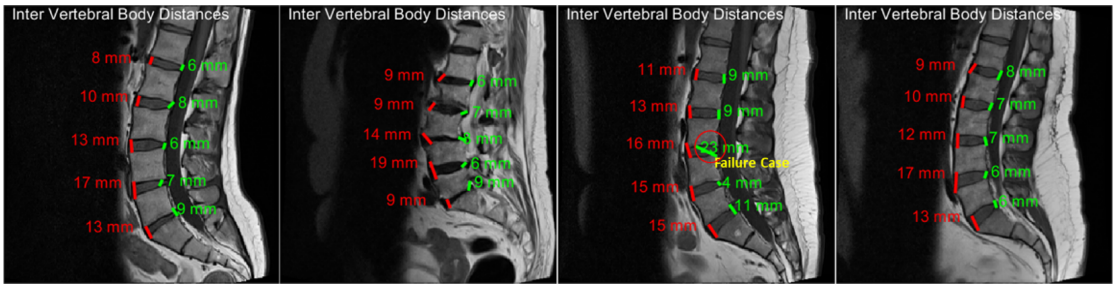

(a) IVB Distances.

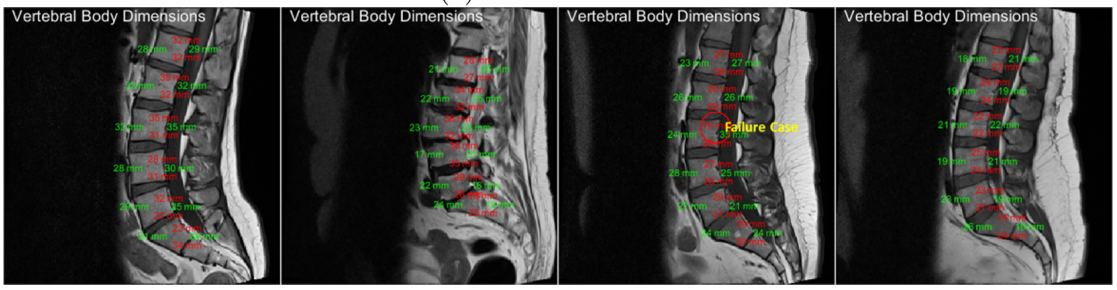

(b) VB(s) Side-Wall Dimensions.

FIGURE 6.4: Calculation of Intervertebral body (IVB) distances and VB Dimensions in *mm*.

6.2.4 Angular Measurements

After computing the distance related measurements, angular measurements are also performed. First, *lumbar lordotic angle (LLA)*, being the angle subtended by L1 superior-endplate and S1 superior-endplate, is measured as represented by white lines in figure 6.4a. The expression is given as

$$m^{L1,S1} = \frac{y_2^{L1,S1} - y_1^{L1,S1}}{x_2^{L1,S1} - x_1^{L1,S1}} \tag{6.4}$$

where in equation 6.4, $m^{L1,S1}$ depict slopes of two line segments i.e., L1 superior-endplate and S1 superior-endplate. The angle θ is calculated using the expression given in equation 6.5 below

$$\theta = \tan^{-1} \left| \frac{m^{L1} - m^{S1}}{1 + m^{L1} m^{S1}} \right| \tag{6.5}$$

In the similar manner, *lumbosacral angle (LSA)*, angle subtended by the L5 inferior end-plate and S1 superior end-plate is also measured as shown in figure 6.4b where the green lines depict the L5 inferior-endplate and S1 superior-endplate. The

measured angles are also labelled in both cases for LLA and LSA.

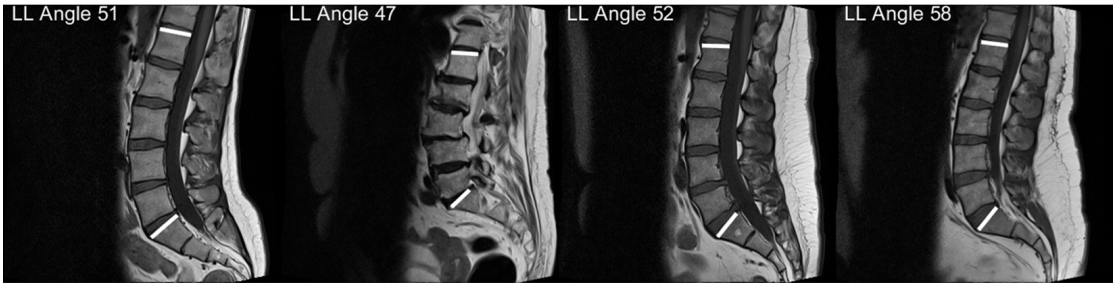

(a) Lumbar Lordotic Angle (LLA).

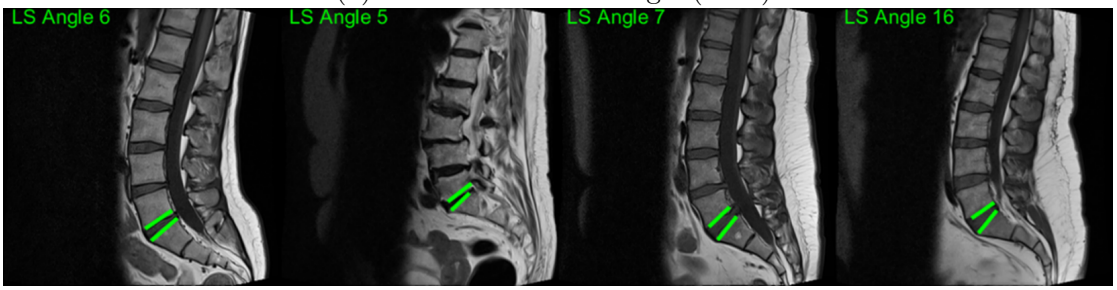

(b) Lumbosacral Angle (LSA).

FIGURE 6.5: Spinal Angular Measurements measured in Degrees (°)

6.2.5 Spinal Curve Estimation

Lumbar spinal curve is also plotted to differentiate between the symmetrical and asymmetrical spinal curves. Here, cubic spline interpolation is used instead of polynomial piecewise interpolation to avoid the higher order polynomials hence avoiding overfitting and enabling better generalization of spinal curve. In the case of lumbar spine, spline fitting is performed on previously identified centroids. The expression is given as

$$C_i(x) = a_i x^3 + b_i x^2 + c_i x + d_i \tag{6.6}$$

where, in this particular case $n = 6$ i.e., six centroids, hence *n-1* splines are fitted between the set of coordinates. It is also important to mention that for cubic spline to be smooth and continuous following two sets of conditions should be satisfied:

- **Condition for Continuous Spline**

  The expression $C_i(x_i) = y_i$ and $C_i(x_{i-1}) = y_{i-1}$ needs to be satisfied for

the splines to meet the criteria i.e., two consecutive polynomials $C_i(x)$ and $C_{i+1}(x)$ must join at x_i, or equivalently the polynomial passes through the two end points.

- **Condition for Smoothness**

  For a curve to be smooth, the same order derivative should be equal between two consecutive splines at the same point. The statement is expressed $C\prime_i(x_i) = C\prime_{i+1}(x_i)$ and $C\prime\prime_i(x_i) = C\prime\prime_{i+1}(x_i)$. Here, $C\prime_i(x_i)$ is the first derivative, while $C\prime\prime_i(x_i)$ shows the second derivative at point x_i. Alternatively, the expression can be generalized as $C_i^{(k)}(x_i) = C_{i+1}^{(k)}(x_i)$, where, k is the order of derivative.

The result of curve estimation is given in figure 6.6, where in second sub-image from right it can be seen that the slope in asymmetrical giving evidence that spinal balance is out of order, whereas in the other shown sub-images the curves are found to be symmetrical.

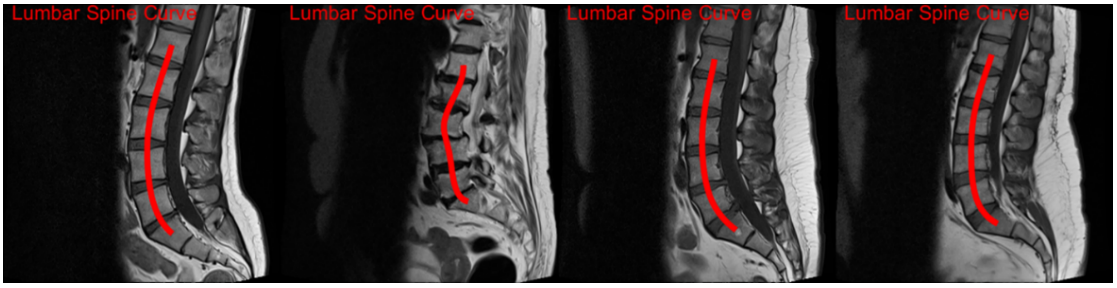

FIGURE 6.6: Estimation of Spinal Curve.

Since, all these distance related measurements are in pixels which are made meaningful and relatable by conversion of these distances into millimeters. For this purpose, the respective pixel spacing information is extracted from the DICOM file and the distance in pixels are scaled as per the pixel spacing information.

6.3 Summary

- In the proposed spinal measurements acquisition methodology, centroids are initially computed in the segmented images containing VBs, followed by distance based and angular measurements.
- These measurements are performed through automated way to give support to the clinicians to acquire these measurements certainly be conserving time as well as giving quantitative bias to their manual performed measurements.
- Spinal curve estimation is performed to support the subsequent spinal disorder diseases classification methodologies as proposed in this thesis.

Chapter 7

Spinal Misalignment Disease Classification

7.1 Outline

After extracting the spinal profiles, including spinal measurements (6.2.3) and spinal curve estimation(6.2.5), spinal misalignment classification methodologies for spondylolisthesis i.e., the dislocation of VB towards anterior or posterior side as well as identification of hyper/hypo/normal lordosis using a novel proposed method. In section 7.2 classification methodology for spondylolisthesis is presented followed by lordosis assessment in section 7.3.

7.2 Automated Spondylolisthesis Classification

As already covered in the section 3.6.1, for grading of severity and determining etiological type of spondylolisthesis, Meyerding classification grading system is commonly used. The clinicians mostly resort to grading by visual observation, without performing the measurements. Quite evidently, this methodology for grading is subjective in nature, therefore, automated quantitative assessment is necessitated. In this thesis, a novel technique to identify and classify spinal misalignment i.e.,

spondylolisthesis by using an improvised angular deviation metric is proposed, diagrammatic flowchart is shown in the figure 7.1 whereas the algorithmic representation is given as algorithm 3.

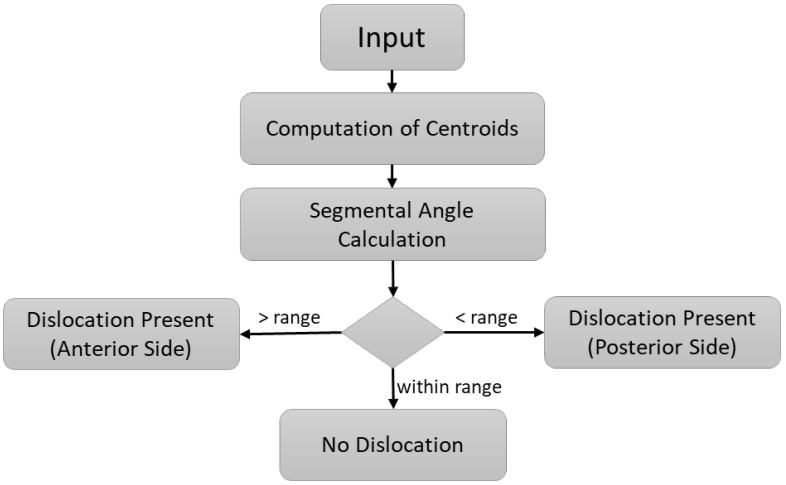

FIGURE 7.1: Flow Diagram for Classification of Spondylolisthesis.

In proposed method, instead of the original method used by clinicians to measure spondylolisthesis which is based on corner-points and related to end-plate structure; evaluation for presence of spondylolisthesis through centroids is performed, thus harnessing the potential of automated measurements and the previously computed centroids (6.2.1) and corner-points(6.2.2).

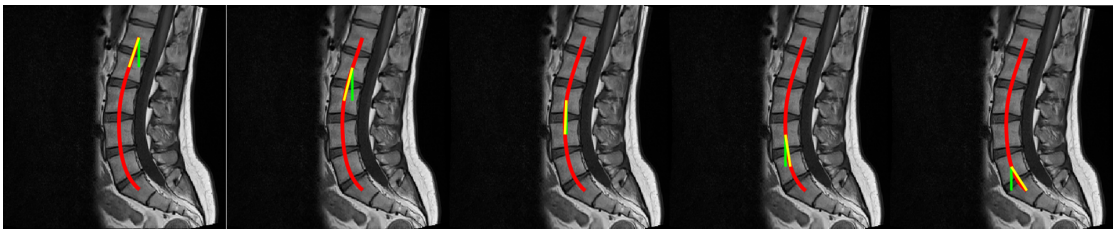

FIGURE 7.2: Angular Deviation Metric for Assessment of Spondylolisthesis.

As shown in figure 7.2, initially beginning from L1 VB (left), the angle subtended between perpendicular line (shown in green) from L1 centroid and the line segment from L1 centroid to L2 centroid (shown in yellow) is measured. The process is repeated for all the VBs from L2 to S1 as shown in figure 7.2(left to right). Intuitively, it can be seen that if the angle of respective VB is found deviating beyond the standard deviation of the mean of angles of all VBs, the VB is classified

to have dislocation i.e., spondylolisthesis or mathematically as shown in equation 7.1given below:

$$\omega_i = \frac{1}{n}\sum_{i=1}^{n}\theta_i \pm \sigma_\theta \tag{7.1}$$

where, θ_i is the angular deviation measured between the yellow and green lines as shown in figure 7.2(left to right), n=5 i.e., the number of VBs segments and σ_θ is the measure of standard deviation. The dislocated VB is then labelled along with the image.

Algorithm 3: Spondylolisthesis Classification

Input: Extracted Image I_{VB}
Output: *Classification* ω_i
$cen_i \leftarrow$ ComputeCentroids(I_{VB}) $[i = n_{VB}]$
$\theta_{i-1} \leftarrow$ ComputeAngle(cen_i)
$\theta_m \leftarrow$ ComputeMean(θ_{i-1})
$\sigma_\theta \leftarrow$ ComputeSD(θ_{i-1})
for $\forall$ cen_i **do**
    if $\angle_i > \theta_m + \sigma_\theta$ **then**
        $\omega_i^{anterior} \leftarrow I_{VB_i}$
    else
        if $\angle_i < \theta_m - \sigma_\theta$ **then**
            $\omega_i^{posterior} \leftarrow I_{VB_i}$
        else
            if $\theta_m - \sigma_\theta < \angle_i < \theta_m + \sigma_\theta$ **then**
                $\omega_i^{normal} \leftarrow I_{VB_i}$
            end
        end
    end
end
$\omega_i \leftarrow \omega_i^{anterior}$
$\omega_i \leftarrow \omega_i^{posterior}$
$\omega_i \leftarrow \omega_i^{normal}$

A noticeable *advantage* in proposed angular deviation classification metric, is the ability to handle displacement of VB in both posterior and anterior directions. The present-day method used by clinicians to evaluate spondylolisthesis is based on posterior-inferior corner-points [150] as already referred and shown in figure

3.6. In this proposed algorithm, the posterior or backwards displacement is quantified, if the angular deviation is less than the standard deviation of mean of all deviation angles, similarly, the anterior or forward displacement is conditional to the deviation beyond the standard deviation of mean of all angles as highlighted in the algorithm 3.

7.3 Automated Lumbar Lordosis Assessment

Exploiting the potential of most reliable [154] methods for lumbar spine lordosis evaluation, the proposed method is a combination of Chen centroid method [167] and Yang AUC method [168] as discussed in section 3.6.2. In this proposed method, spinal curve is plotted (section 6.2.5) through the centroids instead of posterior corner-points in the original Yang method. Afterwards, the superior VB centroid is connected directly to inferior VB centroid and area enclosed in the region is computed in the similar pattern as suggested in Yang method. The diagrammatic flowchart of proposed method is presented in figure 7.3, where the red colored region classifies the hyper lordosis or excessive lordotic curve commonly termed as sway-back, yellow box presents the hypo lordosis classification or inadequate lordotic curve commonly termed as flat-back cases and the green region is shows the normal lumbar lordosis curve cases.

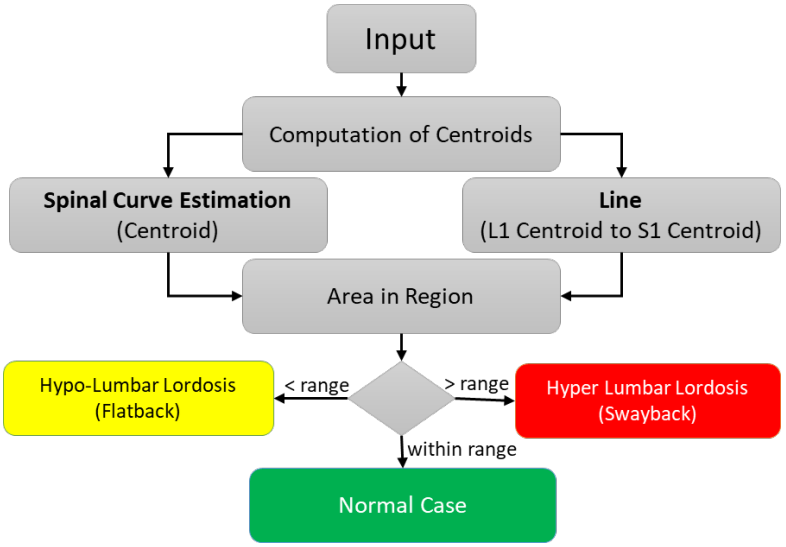

FIGURE 7.3: Flow Diagram for Assessment of Lumbar Lordosis.

In this proposed method for classification of spinal curve disorder as shown in figure 7.4a, the spinal curve through centroids of VBs is initially plotted followed by joining the L1 VB centre with S1 VB centre, thus forming an enclosed region. In the second step, the enclosed region is segmented out (figure 7.4b) and finally area within the region is measured in the final step as shown figure 7.4c. As suggested in the original work [168], while calculating AUC, it is empirically noted that for hypo-lordosis, the AUC is found to be less while AUC is noted to be more for hyper-lordosis cases. The expression is given as equation 7.2, which is the summation of all non-zero pixels ($p_i \neq 0$) within the region r as shown in figure 7.4c, where the total number of non-zero pixels are m and Δp is the interval i.e., equal to one pixel.

$$A_r = \sum_{i=1}^{m} p_i \times \Delta p \tag{7.2}$$

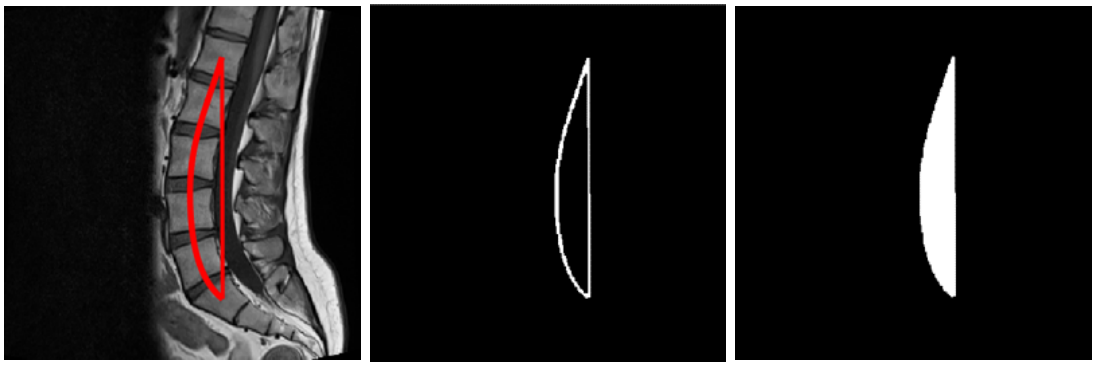

(a) Region Plotting (b) Region Segmentation (c) Area Computation

FIGURE 7.4: Proposed AUC Method for Lumbar Lordosis Assessment.

The same sequence is represented in algorithmic form as algorithm 4.

7.4 Summary

- Traditionally as practiced by clinicians, the classification of spondylolisthesis is performed visually without making any dedicated measurements which is subjective and prone to variability.
- For assessment of lumbar lordosis, modified Cobb method is used by the clinicians which is related to the superior and inferior VB end-plates, hence,

Algorithm 4: Hyper/Hypo/Normal Lordosis Classification

Input: Extracted Image I_{VB}
Output: *Classification* ω
$cen_i \leftarrow$ ComputeCentroids(I_{VB}) $[i = nVB]$
$Curve \leftarrow$ SpinalCurve(cen_i)
$Region \leftarrow$ MakeRegion($Curve$)
$A_r \leftarrow$ Area($Region$)
$\phi \leftarrow$ Range(A_r)$[a, b]$
if $A_r > \phi$ **then**
    $\omega_{hyper} \leftarrow I_{VB}$
else
    if $A_r < \phi$ **then**
        $\omega_{hypo} \leftarrow I_{VB}$
    else
        if $A_r = \phi$ **then**
            $\omega_{normal} \leftarrow I_{VB}$
        end
    end
end
$\omega \leftarrow \omega_{hyper}$
$\omega \leftarrow \omega_{hypo}$
$\omega \leftarrow \omega_{normal}$

in case of deformation or fracture correct lordosis assessment may not be possible.

- The proposed methodology for classification of spondylolisthesis is based on angular deviation metric encompassing dislocation in both anterior and posterior directions.

- For assessment of lordosis, the proposed method, based on AUC computation is independent of corner-points hence, is more robust to the end-plate deformities.

Chapter 8

Results and Discussion

8.1 Outline

In this chapter, first the metrics which are used to validate the performance of the automated VB extraction i.e., segmentation, automated spinal measurements and spinal diseases classification are presented. The same are extensively used by the research community [78, 80, 162, 199–204] Afterwards, detailed experimental results with qualitative analysis for ground truth annotations and VB segmentation are discussed. Later, quantitative analysis of the implemented segmentation techniques, automated spinal measurements and methodologies for spinal disorder diseases classification are highlighted.

8.2 Performance Metrics

To evaluate the performance of semantic segmentation, *mean pixel accuracy (MPA)* and *mean pixel precision (MPP)* metrics as given in equations 8.1 and 8.2 are used. Accuracy corresponds to the measure of percentage of pixels classified correctly in global context as VB and background, whereas, precision is the measure of correctness of classification at global level.

$$MPA = \frac{T_P + T_N}{T_P + T_N + F_P + F_N} \tag{8.1}$$

$$MPP = \frac{T_P}{T_P + F_P} \tag{8.2}$$

where, T_P denotes the pixel-level true positives indicating the correct extraction of VBs, T_N relates to pixel-level true negatives showing correct assignment of pixels as background, F_P signifies the pixel-level false positives indicating incorrect extraction of background pixels as VB and F_N specifies the false negatives i.e., incorrect extraction of VB pixel labels.

To measure the overlap between the segmented mask and the actual ground truth mask, mean *intersection-over-union (IoU)* commonly termed as Jaccard similarity coefficient score is used, which is measured through equation 8.3.

$$IoU = \frac{T_P}{T_P + F_P + F_N} \tag{8.3}$$

Additionally, *dice similarity coefficient (DSC)* score is also computed which computes the IoU/Jaccard metric with the only difference that it doubles the true-positives T_P, expression is given as equation 8.4.

$$DSC = \frac{2T_P}{2T_P + F_P + F_N} \tag{8.4}$$

To measure of closeness of the automated measured value with the manual measurement performed by spinal surgeons, *Pearson correlation coefficient* is used as given in equation 8.5,

$$R = \frac{\sum_{i=1}^{N}(m_i - \bar{m})(n_i - \bar{n})}{\sqrt{\sum_{i=1}^{N}(m_i - \bar{m})^2 \sum_{i=1}^{N}(n_i - \bar{n})^2}} \tag{8.5}$$

where, R is the correlation coefficient, N is the total number of observations, m_i is the automated calculated measurement taken for a specific sample i, $\bar{m}$ is the

mean value of automated computed measurement, n_i is manual computer assisted measurement performed by the spinal surgeon for a specific sample i, $\bar{n}$ is the mean of manual measurement performed by the spinal surgeon. Its value ranges from -1 to 1 where the value *(R=0)* means that the measurements are not correlated.

Similarly, to measure the errors in the predicted or estimated value without considering the direction of error mean *absolute error metric (MAE)* is computed. The expression given in equation 8.6:

$$MAE = \frac{1}{N}\sum_{i=1}^{N}|x_i - \bar{x_i}| \tag{8.6}$$

which shows that x_i is the computer assisted measurement performed by the spinal surgeon and $\bar{x_i}$ is the automated measurement. The average value gives the estimate of error value giving individual difference equal weight.

8.3 Results

For better presentation, the respective results are categorized in the same order according to each experiment. Details are as under:

8.3.1 Segmentation of VBs

The qualitative results are shown in Figure 8.1, followed by detailed quantitative assessment as given in table 8.1. In the figure, the sub-captions are also mentioned below each row showcasing the type of images. Here, a selected pictorial comparison of results obtained by VBSeg algorithm with the segmentation results obtained through various deep learning networks is presented. A row represents results of a single scheme on various samples whereas a column represents the results with different model/methods for a specific sample. A failure case is also presented in second column from left where it can be seen that VBSeg totally misses the VBs, whereas the deep learning methods have shown promising results. It can also be

seen that ResNet-UNet conveniently outperforms the results obtained by other deep learning networks including original proposed VBSeg, despite the fact VB-Seg is a customized thoroughly worked-out algorithm to perform VB segmentation task.

Similarly, while analyzing the quantitative aspects in table 8.1, it is quite evident that, the validation sequence used in VBSeg (VBSeg$^{\uparrow}$) as given in section 5.2.3 shows improvement in metrics, but is unable to reach anywhere near the results of best segmentation metrics obtained through deep learning networks. Amongst the deep learning networks, quite obviously, the lowest quantitative metrics are given by MobileNets-UNet$^{\downarrow}$ with the lowest training time. The results of VBSeg$^{\uparrow}$ are comparable to MobileNets-UNet$^{\downarrow}$ with respect to achieved IoU and DSC scores. In table 8.1, mean pixel accuracy is represented by MPA, mean pixel precision by MPP, intersection over union is given by IoU whereas dice similarity coefficient score is given by DSC. Additionally, $*$ marks with the models represents the best results within the same base-model category i.e., VGG, ResNet, MobileNets. The overall best results are given in bold whereas the worst result in the deep learning category are given by $\downarrow$ as marked with MobileNets-UNet. Here, it is also important to mention that MPA and MPP values are ranging from 0 to 100 where a value close to 100 is signifying better performance. Similarly, the values of IoU and DSC are ranging between 0 to 1, where, a value close to 1 represents a better performance of the model/method.

In table 8.2, a comparison of results obtained with the ResNet-UNet architecture used in this thesis with the results of other researchers for segmentation task is presented. The image modality (IM) and the method or technique adopted by respective researcher is also mentioned. Ghosh et al.[205] used neighborhood information to simultaneously segment IVD and thecal sac achieving a DSC of 0.84 making use of decision trees as represented by DT in the table 8.2, however, VB segmentation was not performed. Most researchers achieved good results with FCN and UNet architectures [73, 74, 76, 206]. Suzani et al. [207] achieved 96 and 94.4 percent accuracy and precision respectivel by 6 layered deep forward network. Tang et al. [77] used dual densely connected UNet (DDUNet) to achieve IoU score

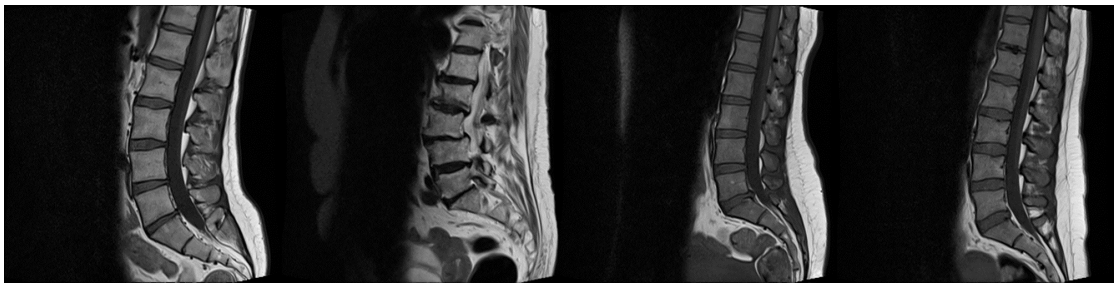

(a) Input Images.

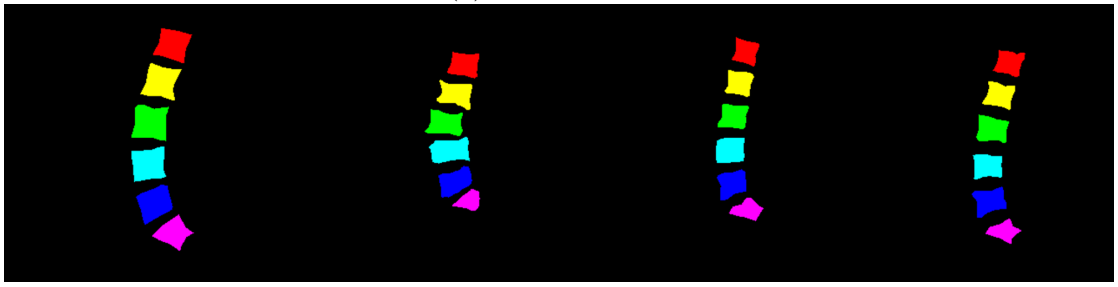

(b) Ground Truth Images.

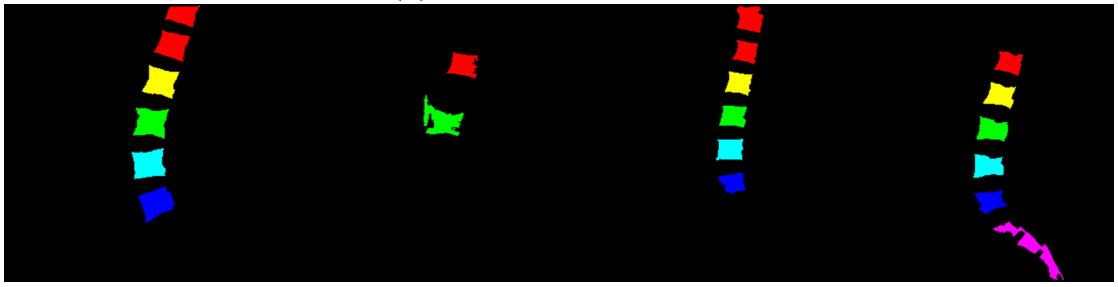

(c) Result of VBSeg (Proposed Conventional Algorithm).

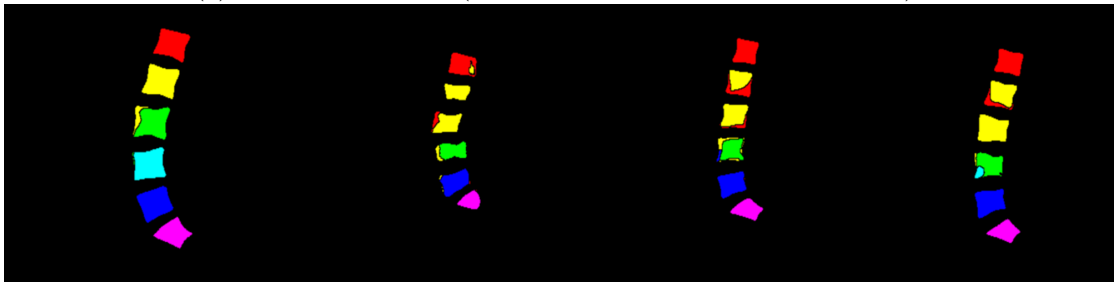

(d) Proffered Architecture ResNet-UNet.

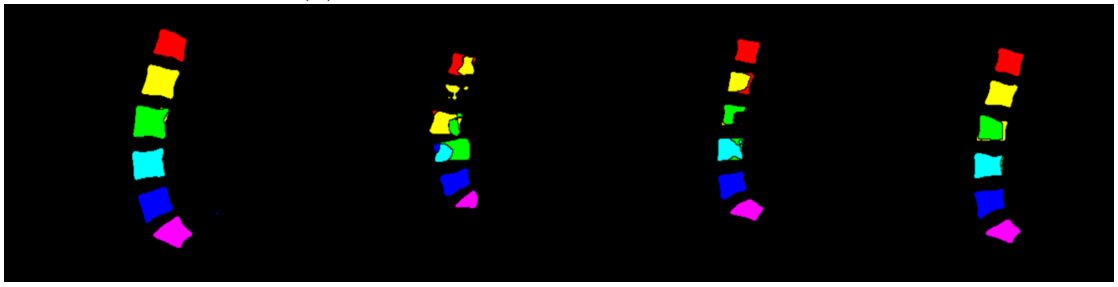

(e) VGG-SegNet Architecture.

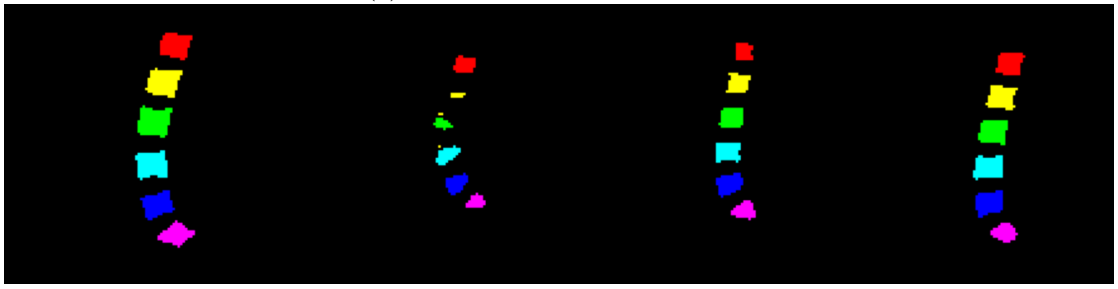

(f) MobileNets-SegNet Architecture.

FIGURE 8.1: Qualitative Comparison of VB Segmentation Results

TABLE 8.1: Comparative Quantitative Analysis of Methods/Models used for Semantic Segmentation. Mean Pixel Accuracy (MPA), Mean Pixel Precision (MPP), Intersection-over-Union (IoU), Dice Similarity Coefficient (DSC)

	MPA	**MPP**	**IoU**	**DSC**
VBSeg (Pre-Validation)	96.34	57.46	0.49	0.67
VBSeg (Post-Validation)$^{\uparrow}$	97.99	66.57	0.63	0.79
UNet	98.36	90.67	0.74	0.87
PSPNet	98.33	88.95	0.73	0.80
VGG-UNet	99.02	87.29	0.82	0.93
VGG-PSPNet	97.85	91.85	0.69	0.69
VGG-SegNet*	98.85	95.41	0.81	0.95
ResNet-UNet*	**99.12**	**98.31**	**0.86**	**0.97**
ResNet-PSPNet	98.08	95.66	0.72	0.76
ResNet-SegNet	98.59	98.06	0.78	0.93
MobileNets-UNet$^{\downarrow}$	97.50	81.33	0.67	0.63
MobileNets-SegNet*	98.63	88.71	0.75	0.87

of 0.83. Huang et al.[200] achieved a superior IoU score for vertebra segmentation with UNet architecture on a dataset of 100 MRI in which 50/50 split was used for training and testing purpose. Clearly, the results obtained by the proffered method i.e., ResNet-UNet are significantly better as compared to the results of other researchers in accuracy, precision and DSC. In literature, the reported range for MPA and MPP is also from 0 to 1, however, the value is scaled between 1 to 100 in order to avoid confusion. The values of IoU and DSC are within the range from 0 to 1, where the value near to zero shows that very less overlap is present between the ground truth and segmented image and the value near to one represents a good overlap.

TABLE 8.2: Comparison of Segmentation Results with related Researchers' Work. Image Modality (IM), Mean Pixel Accuracy (MPA), Mean Pixel Precision (MPP), Intersection-over-Union (IoU), Dice Similarity Coefficient (DSC)

	Method	IM	**MPA**	**MPP**	**IoU**	**DSC**
Proffered Method	ResNet-UNet	MR	**99.12**	**98.31**	0.86	**0.97**
Ghosh et al.[205]	DT	MR	-	-	-	0.84
Suzani et al. [207]	6-FFN	CT	96	94.4	-	-
Lu et al. [73]	UNet	MR	94	-	0.91	0.93
Janssens and Zheng [74]	FCN-UNet	CT	-	-	-	0.95
Lessmann et al.[76]	FCN	MR/CT	-	-	-	0.94/0.96
Rak et al.[206]	UNet	MR	-	-	-	0.94
Huang et al.[200]	UNet	MR	-	-	**0.94**	-
Tang et al.[77]	DDUNet	CT	90.1	-	0.83	-

8.3.2 Spinal Measurements

The qualitative aspects of spinal measurements are amply covered and elaborated in Chapter 6 as shown in figures 6.3, 6.4, 6.5 and 6.6. Here, the quantitative aspects are explained. To quantitatively analyze the results of measurements, out of the total 514 images, a sample of 50 images are randomly picked and are manually measured by spinal surgeon using RadiAnt DICOM Viewer by Medixant.

The results are reported in table 8.3, where, R is the correlation coefficient while MAE is mean absolute error, lumbar lordotic angle is referred as LLA, lumbosacral angle as LSA, lumbar heights (corner points) is given as LHCP refer to superior-anterior corner-point of L1 to superior-anterior point S1, lumbar heights (center points) is given as LHC refer to center point of L1 and S1. Moreover, bold indicates the best performance while '-' indicates that the metric was not been computed by the researcher.

GT-SS represents comparison between measurements of ground truth images and measurements of spinal surgeon, GT-DL shows the comparison between measurements of ground truth images and measurements of automated segmented out

TABLE 8.3: Spinal Measurements Quantitative Comparison, Lumbar Lordotic Angle (LLA), Lumbosacral Angle (LSA), Lumbar Height using Corner-Points (LHCP), Lumbar Height using Centroids (LHC)

	LLA		LSA		LHCP		LHC	
	R %	MAE $\theta°$	R %	MAE $\theta°$	R %	MAE mm	R %	MAE mm
GT-SS	**0.979**	**1.45**	**0.951**	**1.55**	**0.997**	**0.82**	**0.996**	**0.89**
GT-DL	0.84	2.61	0.79	2.01	0.981	1.07	0.992	0.95
SS-DL	0.81	3.63	0.83	3.16	0.978	1.2	0.991	0.92
Masad et al.[100]	0.932	-	-	-	-	-	-	-
Pang et al.[98]	-	-	-	-	-	1.23	-	-
Cho et al.[99]	-	8.05	-	-	-	-	-	-

image using deep learning method (ResNet-UNet) and finally, SS-DL means establishing relationship between the measurements of spinal surgeon and automated segmented out image using deep learning model (ResNet-UNet).

It can see that the proposed scheme achieves a correlation coefficient of *0.979* with the clinician's grading (with the MAE of 1.45°) for the LLA. Comparing it with the state-of-the-art schemes, the proposed framework achieved an improvement of *4.80* % (in terms of R). Although this comparison is indirect as the clinician's and their gradings in all the schemes varies. Nevertheless, it is worth noting that the spinal measurement obtained through the proposed scheme highly correlates (being statistically significant i.e. $p < 0.05$) with the expert clinicians as evident through R and MAE scores. Moreover, unlike its competitors, the proposed framework is also capable to measure LSA, and lumber heights as evident from table 8.3.

Here, it is worth mentioning that Pang et al. [98] achieved MAE of *1.23 mm* once measuring lumbar height, but their method suggested user input for specification of L1 and L5 superior-anterior corner points, hence the method proposed by them was not fully automated.

8.3.3 Spinal Disorders Classification

In this subsection, the results of two-proposed spinal disorder diseases classification methods including spondylolisthesis and classification for hyper/hypo/normal lordosis cases are presented.

8.3.3.1 Spondylolisthesis

Based on the manual radiologist report, out of total 514 patients, 29 candidate patients were diagnosed with presence of spondylolisthesis with variation of grade. The proposed automated disease classification system achieved the accuracy of *89 %* following the improvised angular deviation criteria, which was covered in details in section 7.2. A few selected results are displayed as sub-images in figure 8.2, where it can be seen that the classification model correctly identifies and labels the spinal dislocation disorder showcased by 'Disloc at L3' as shown in figure 8.2b. The proposed algorithm 3 also correctly categorized the normal cases labelled as 'No-Dislocation' as shown in figure 8.2a,c.

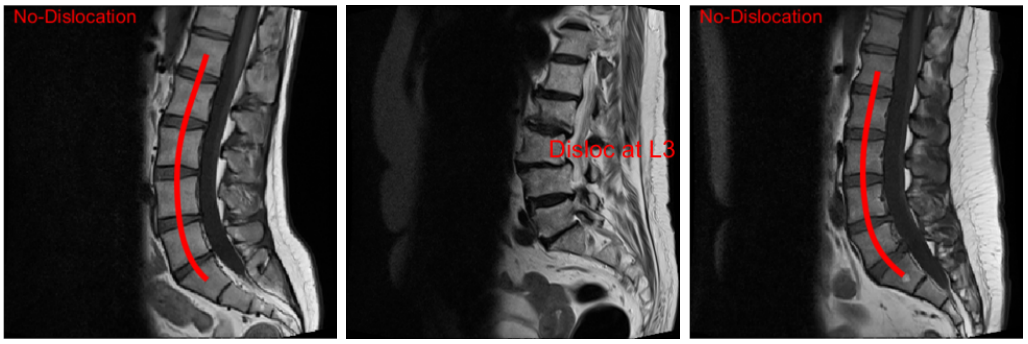

(a) No Dislocation (b) Dislocation at L3 (c) No Dislocation

FIGURE 8.2: Results of Spondylolisthesis Classification

8.3.3.2 Lumbar Lordosis Assessment

As already emphasized in section 7.3, the proposed method is a merger of two existing methods used to evaluate lordosis curve. The proposed method harnessed the accuracy of computed centroids as advocated by Chen method [167], as evaluation with the help of corner-points is subjective to errors in measurement, and

made use of technique of computing area in an enclosed region (A_r) in a similar way as suggested in Yang method [168]. Through meticulous experimentation, it is found that area of region for hypo lordosis / straight-back / flat-back cases is smaller once compared to normal lordosis. Similarly, the area of region for hyper lordosis / sway-back is greater than a normal lordosis curve, the same result were presented in the original AUC method[168]. The proposed automated spinal disorder classification system achieved an accuracy of *93 %* correctly identifying straight-back, sway-back (disorder cases, combined) and identifying the normal lordosis cases. Result of proposed algorithm 4 for automated lordosis assessment is presented in figure 8.3. Here, a sub-sample of results (6-images) is displayed where the normal lordosis are shown in sub-figure 8.3a, sway-back or hyper lordosis cases in sub-figure 8.3b and flat-back or hypo lordosis cases in sub-figure 8.3c.

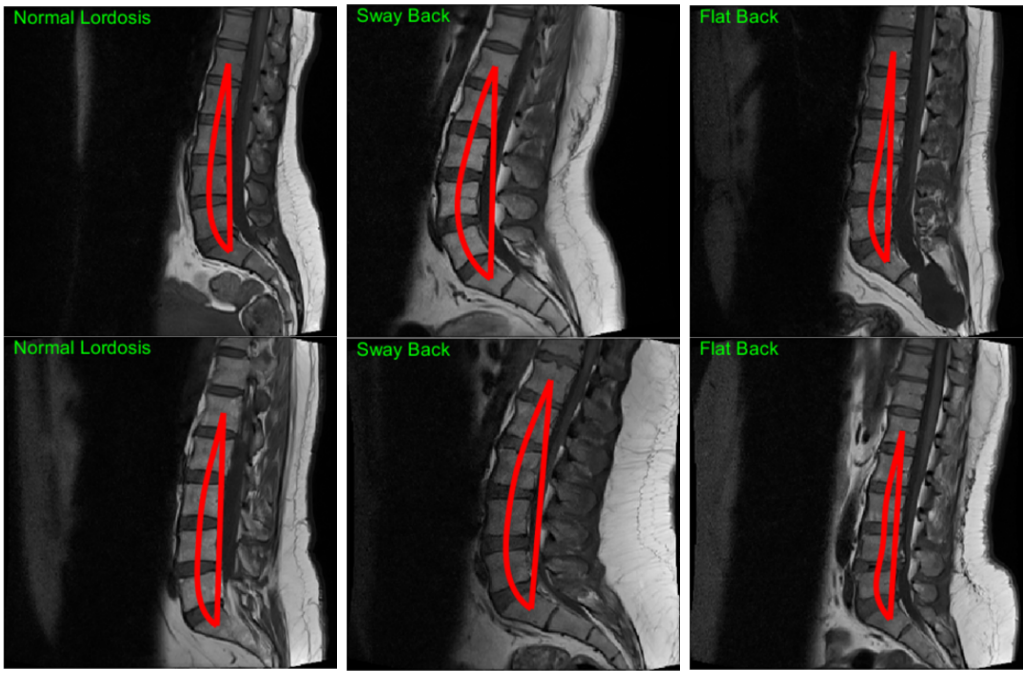

(a) No Dislocation (b) Dislocation at L3 (c) No Dislocation

FIGURE 8.3: Automated Lumbar Lordosis Assessment Result.

8.4 Summary

- The clinicians, at present, use Meyerding classification to grade the severity of spondylolisthesis, which is certainly subjective. The method proposed in this research uses an improvised angular deviation metric to identify the presence of this disorder.

- Likewise, the clinicians identify adequacy/inadequacy of lumbar lordosis through modified Cobb angle, which is dependent on the structure of superior and inferior VB end-plates. The method proposed in this thesis is based on area calculation by creating a region through centroids instead of corner-points.

Chapter 9

Conclusion and Future Direction

9.1 Thesis Summary and Research Contributions

The central theme of this thesis revolved around development of automated lumbar spine assessment toolkit. Usefulness of such an application is gauged by establishing its clinical relevance as discussed in section 3.5. Quite evidently, the effectiveness and reliability of automated assessment framework is directly linked with the precision of vertebral bodies segmentation which later is used for extraction of spinal measurements. For achieving this goal, selection of suitable dataset is most important for further analyzing the problem statement. To contribute in this particular aspect, 2D sagittal views of lumbar spine images are manually annotated through a meticulous process involving labelling and validation on previously available dataset containing 2D intervertebral body discs labelled masks in axial plane (section 4.4).

Extensive non-exhaustive review of related literature is carried out and the identified research gaps are further explored in order to plug the gaps. As a first measure, a customized vertebral body segmentation algorithm (VBSeg) is proposed (section 5.2) based on conventional machine learning and image processing techniques and methods. The main take away of the proposed algorithm is the ability to extract the vertebral body reasonably well keeping the structural integrity intact once

visually analyzed. However, on the other side, the performance metrics of the proposed tailored algorithm were in a lower shade because of lack of generalization once tested on unknown images as suggested in the reviewed literature. In an effort to improve the segmentation task, deep learning architectures are then extensively used with the suggested topology as reflected in the literature reviewed. The segmentation results obtained using the deep learning networks clearly surpassed the results of improvised vertebral segmentation scheme, emphasizing the utility and efficacy of deep learning models to perform the segmentation related tasks. The most refined and less time-consuming process of transfer learning fine-tuning has also proved to be extremely useful once avoiding complexity of training the deep learning models from scratch (section 5.3).

After having performed the segmentation task, clinically significant and most relevant spinal balance measurements are extracted (section 6.2). These extracted images and the earlier manually labelled ground truth images in the sagittal plane collectively make a composite dataset enabling the researchers with quantitative ability to make more reliable and robust solutions. Finally, effectively using the extracted measurements, classification methodologies for spinal balance disorders including the dislocation of vertebral body clinically termed as spondylolisthesis (section 7.2) as well as assessment of lumbar lordosis (section 7.3) for adequate or inadequate lumbar lordotic angle are proposed.

9.2 Conclusion

In a nutshell, an effort was made in this research thesis, to present an automated image understanding of lumbar spine images with the perspective of spinal surgeon who is clinically evaluating the candidate patient through physical examination. The decision for most appropriate surgical intervention procedure is based on certain spinal measurements which are presently done through laborious manual measurements. Adoption of the automated measurement as proposed in this research thesis will certainly save the valuable time of the spinal surgeon as well as

provide confidence to the decision for suitability of shortlisted/selected surgical intervention procedure. Here, a composite dataset comprising of highly detailed annotations of mid-sagittal views of lumbar spine MR images coupled with spinal measurements is presented. Furthermore, an autonomous framework capable of extracting the spinal measurements on-the-fly which can aid the clinicians in objectively assessing the spinal pathology of the candidate subject. Additionally, this thesis also introduced fully automated classification of spinal disorders such as spondylolisthesis, sway-back/flat-back cases.

Certainly, the intended purpose of proposed autonomous lumbar spine toolkit is not to replace the role of clinicians but to introduce a vote of confidence and reliability to their performed manual diagnosis. With the adoption of proposed toolkit, clinicians may enable themselves with reliable quantitative metrics thereby adding precision to the selected/shortlisted surgical intervention procedure.

9.3 Future Direction

In future, the proposed framework can be extended to objectively measure the misalignment within the cervical, thoracic, and pelvic region as well to give more in-depth understanding of the human spinal balance. Like any other framework, medical image understanding framework is excessively data hungry. The already available data may seem insufficient due to the novelty in challenges encountered by researchers while analysing the medical images. This may be supplemented by using 3D volumetric scans, hence creating another dataset with whole spine MRI images will be extremely beneficial.

Another direction which may be explored is determining of the efficacy of automated spinal toolkit in aiding the spinal surgeons to choose less invasive method over extensive invasive methods.

Bibliography

[1] S. H. Roy, C. J. De Luca, and D. A. Casavant, "Lumbar muscle fatigue and chronic lower back pain." *Spine*, vol. 14, no. 9, pp. 992–1001, 1989. [Online]. Available: https://pubmed.ncbi.nlm.nih.gov/2528828/

[2] V. E. Casiano, A. M. Dydyk, and M. Varacallo, "Back pain," *StatPearls [Internet]*, 2020. [Online]. Available: https://www.ncbi.nlm.nih.gov/books/NBK538173/

[3] F. Raciborski, R. Gasik, and A. Kłak, "Disorders of the spine. a major health and social problem," *Reumatologia*, vol. 54, no. 4, p. 196, 2016. [Online]. Available: https://www.ncbi.nlm.nih.gov/pmc/articles/PMC5090028/

[4] K. Hasegawa, M. Okamoto, S. Hatsushikano, H. Shimoda, M. Ono, and K. Watanabe, "Normative values of spino-pelvic sagittal alignment, balance, age, and health-related quality of life in a cohort of healthy adult subjects," *European Spine Journal*, vol. 25, no. 11, Nov 2016. [Online]. Available: https://pubmed.ncbi.nlm.nih.gov/27432430/

[5] H. Shemshaki, M. Etemadifar, M. Fereidan-Esfahani, M. Mokhtari, and S.-M. Nourian, "What is the source of low back pain?" *Journal of Craniovertebral Junction and Spine*, vol. 4, no. 1, 2013. [Online]. Available: https://www.jcvjs.com/text.asp?2013/4/1/21/121620

[6] S. Jonsdottir, H. Ahmed, K. Tómasson, and B. Carter, "Factors associated with chronic and acute back pain in Wales, a cross-sectional study," *BMC Musculoskeletal Disorders*, 2019. [Online]. Available: https://bmcmusculoskeletdisord.biomedcentral.com/articles/10.1186/s12891-019-2477-4

[7] P. Suri, E. J. Boyko, J. Goldberg, C. W. Forsberg, and J. G. Jarvik, "Longitudinal associations between incident lumbar spine MRI findings and

chronic low back pain or radicular symptoms: retrospective analysis of data from the longitudinal assessment of imaging and disability of the back (LAIDBACK)," *BMC Musculoskeletal Disorders*, vol. 15, no. 1, p. 152, Dec 2014. [Online]. Available: https://doi.org/10.1186/1471-2474-15-152

[8] J. W. Frymoyer, "Back pain and sciatica," *New England Journal of Medicine*, vol. 318, no. 5, pp. 291–300, 1988. [Online]. Available: https://pubmed.ncbi.nlm.nih.gov/2961994/

[9] K. Gelse, S. Söder, W. Eger, T. Diemtar, and T. Aigner, "Osteophyte development—molecular characterization of differentiation stages," *Osteoarthritis and cartilage*, vol. 11, no. 2, pp. 141–148, 2003. [Online]. Available: https://www.semanticscholar.org/paper/Osteophyte-development--molecular-characterization-Gelse-Soeder/3e832e20f32add2e4a4778a780f3144b5364bea4

[10] R. A. Deyo and Y.-J. Tsui-Wu, "Descriptive Epidemiology of Low-back Pain and Its Related Medical Care in the United States," *Spine*, vol. 12, no. 3, Apr 1987. [Online]. Available: https://pubmed.ncbi.nlm.nih.gov/2954221/

[11] P. Suetens, *Fundamentals of medical imaging*, 2017. [Online]. Available: https://www.cambridge.org/core/books/fundamentals-of-medical-imaging/E9D727DBE7EB6150768A74F655C07BAC

[12] T. Sawyers, "CT Scans vs. MRIs: Differences, Benefits, and Risks," 2018. [Online]. Available: https://www.healthline.com/health/ct-scan-vs-mri

[13] S. S. Eun, H.-Y. Lee, S.-H. Lee, K. H. Kim, and W. C. Liu, "Mri versus ct for the diagnosis of lumbar spinal stenosis," *Journal of Neuroradiology*, vol. 39, no. 2, pp. 104–109, 2012. [Online]. Available: https://pubmed.ncbi.nlm.nih.gov/21489629/

[14] "Anatomical Planes - Coronal - Sagittal - TeachMeAnatomy." [Online]. Available: https://teachmeanatomy.info/the-basics/anatomical-terminology/planes/

[15] S. A. Mirjalili, S. L. McFadden, T. Buckenham, B. Wilson, and M. D. Stringer, "Anatomical planes: are we teaching accurate surface anatomy?" *Clinical Anatomy*, vol. 25, no. 7, pp. 819–826, 2012. [Online]. Available: https://pubmed.ncbi.nlm.nih.gov/22674662/

[16] "1.4D: Body Planes and Sections - Medicine LibreTexts." [Online]. Available: https://med.libretexts.org/Bookshelves/Anatomy_and_Physiology/Book%3A_Anatomy_and_Physiology_(Boundless)/1%3A_Introduction_to_Anatomy_and_Physiology/1.4%3A_Mapping_the_Body/1.4D%3A_Body_Planes_and_Sections

[17] P. Armstrong and S. F. Keevil, "Magnetic resonance imaging–1: Basic principles of image production." *BMJ: British Medical Journal*, vol. 303, no. 6793, p. 35, 1991. [Online]. Available: https://www.jstor.org/stable/29712192?seq=1

[18] D. B. Plewes and W. Kucharczyk, "Physics of MRI: A primer," 2012. [Online]. Available: https://onlinelibrary.wiley.com/doi/full/10.1002/jmri.23642

[19] R. B. Buxton, R. R. Edelman, B. R. Rosen, G. L. Wismer, and T. J. Brady, "Contrast in rapid mr imaging: T1- and t2-weighted imaging," *Journal of computer assisted tomography*, vol. 11, no. 1, pp. 7–16, 1987. [Online]. Available: https://pubmed.ncbi.nlm.nih.gov/3805431/

[20] L. J. Wolansky, D. D. Parikh, K. J. Shah, R. Yalamanchili, and J. Farkas, "Magnetic resonance imaging protocols for cervical disc disease: What is your neighbor up to?" *Journal of Neuroimaging*, vol. 15, no. 2, pp. 183–187, Apr 2005. [Online]. Available: https://pubmed.ncbi.nlm.nih.gov/15746231/

[21] F. Zanchi, R. Richard, M. Hussami, A. Monier, J.-F. Knebel, and P. Omoumi, "MRI of non-specific low back pain and/or lumbar radiculopathy: do we need T1 when using a sagittal T2-weighted Dixon sequence?" *European Radiology*, vol. 30, no. 5, May 2020. [Online]. Available: https://pubmed.ncbi.nlm.nih.gov/32020402/

[22] Lloyd-Jones Graham, "MRI interpretation - T1 v T2 images," 2017. [Online]. Available: https://www.radiologymasterclass.co.uk/tutorials/mri/t1_and_t2_images

[23] M. C. Jensen, M. N. Brant-Zawadzki, N. Obuchowski, M. T. Modic, D. Malkasian, and J. S. Ross, "Magnetic Resonance Imaging of the Lumbar Spine in People without Back Pain," *New England Journal of Medicine*, vol. 331, no. 2, Jul 1994. [Online]. Available: https://pubmed.ncbi.nlm.nih.gov/8208267/

[24] D. A. Seehusen, M. Reeves, and D. Fomin, "Cerebrospinal fluid analysis," *American family physician*, vol. 68, no. 6, pp. 1103–1108, 2003. [Online]. Available: https://www.aafp.org/afp/2003/0915/p1103.html

[25] S. Hahn, Y. H. Lee, and J. S. Suh, "Detection of vertebral metastases: A comparison between the modified Dixon turbo spin echo T2 weighted MRI and conventional T1 weighted MRI: A preliminary study in a tertiary centre," *British Journal of Radiology*, vol. 91, no. 1085, Mar 2018. [Online]. Available: https://pubmed.ncbi.nlm.nih.gov/29393668/

[26] P. Suri, D. J. Hunter, J. N. Katz, L. Li, and J. Rainville, "Bias in the physical examination of patients with lumbar radiculopathy," *BMC Musculoskeletal Disorders*, 2010. [Online]. Available: https://www.ncbi.nlm.nih.gov/pmc/articles/PMC3009628/

[27] P. Mildenberger, M. Eichelberg, and E. Martin, "Introduction to the dicom standard," *European radiology*, vol. 12, no. 4, pp. 920–927, 2002. [Online]. Available: https://pubmed.ncbi.nlm.nih.gov/11960249/

[28] R. E. Cooke Jr, M. G. Gaeta, D. M. Kaufman, and J. G. Henrici, "Picture archiving and communication system," Jun. 3 2003, uS Patent 6,574,629. [Online]. Available: https://patents.google.com/patent/US6574629B1/en

[29] M. Pourahmadi, I. E. Takamjani, J. Sarrafzadeh, H. Mohsenifar, S. H. Fazeli, R. Bagheri, and M. Taghipour, "Effect of Chronic Low Back Pain on Lumbar Spine Lordosis During Sit-to-Stand and Stand-to-Sit," *Journal of Manipulative and Physiological Therapeutics*, vol. 43, no. 2, pp. 79–92, Feb 2020. [Online]. Available: https://pubmed.ncbi.nlm.nih.gov/32482434/

[30] S. Berven and R. Wadhwa, "Sagittal Alignment of the Lumbar Spine," *Neurosurgery Clinics of North America*, vol. 29, no. 3, pp. 331–339, Jul 2018. [Online]. Available: https://pubmed.ncbi.nlm.nih.gov/29933801/

[31] E. Been and L. Kalichman, "Lumbar lordosis," *Spine Journal*, vol. 14, no. 1, pp. 87–97, Jan 2014. [Online]. Available: https://www.thespinejournalonline.com/article/S1529-9430(13)01385-5/fulltext

[32] S.-W. Chun, C.-Y. Lim, K. Kim, J. Hwang, and S. G. Chung, "The relationships between low back pain and lumbar lordosis: a systematic review and meta-analysis," *The Spine Journal*, vol. 17, Aug 2017. [Online]. Available: https://pubmed.ncbi.nlm.nih.gov/28476690/

[33] M. R. Konieczny, S. Schroer, C. Schleich, M. Prost, M. Hufeland, H. Kubo, and R. Krauspe, "Lumbar lordosis as tool to assess the level of pain in patients with low back pain after lumbar disc herniation," *Journal of Orthopaedics*, vol. 22, pp. 190–193, Nov 2020. [Online]. Available: https://pubmed.ncbi.nlm.nih.gov/32419763/

[34] J. N. A. Gibson and G. Waddell, "Surgery for degenerative lumbar spondylosis: updated cochrane review," *Spine*, vol. 30, no. 20, pp. 2312–2320, 2005. [Online]. Available: https://pubmed.ncbi.nlm.nih.gov/16227895/

[35] M. Merkle, B. Wälchli, and N. Boos, "Degenerative lumbar spondylosis," in *Spinal Disorders: Fundamentals of Diagnosis and Treatment*. Springer Berlin Heidelberg, 2008, pp. 539–583.

[36] K. Middleton and D. E. Fish, "Lumbar spondylosis: Clinical presentation and treatment approaches," 2009. [Online]. Available: https://pubmed.ncbi.nlm.nih.gov/19468872/

[37] R. J. Mobbs, K. Phan, G. Malham, K. Seex, and P. J. Rao, "Lumbar interbody fusion: techniques, indications and comparison of interbody fusion options including PLIF, TLIF, MI-TLIF, OLIF/ATP, LLIF and ALIF." *Journal of spine surgery (Hong Kong)*, 2015. [Online]. Available: https://pubmed.ncbi.nlm.nih.gov/27683674/

[38] E. Syrmou, P. P. Tsitsopoulos, D. Marinopoulos, C. Tsonidis, I. Anagnostopoulos, and P. D. Tsitsopoulos, "Spondylolysis: A review and reappraisal," pp. 17–21, 2010. [Online]. Available: https://pubmed.ncbi.nlm.nih.gov/20411054/

[39] K. Hashimoto, T. Aizawa, H. Kanno, and E. Itoi, "Adjacent segment degeneration after fusion spinal surgery—a systematic review," *International Orthopaedics*, vol. 43, no. 4, Apr 2019. [Online]. Available: https://pubmed.ncbi.nlm.nih.gov/30470865/

[40] C.-H. Lee, C. K. Chung, J.-S. Jang, S.-M. Kim, D.-K. Chin, J.-K. Lee, S. H. Yoon, J. T. Hong, Y. Ha, C. H. Kim, and S.-J. Hyun, "Effectiveness of deformity-correction surgery for primary degenerative sagittal imbalance: a meta-analysis," *Journal of Neurosurgery: Spine*, vol. 27, no. 5, Nov 2017. [Online]. Available: https://thejns.org/spine/view/journals/j-neurosurg-spine/27/5/article-p540.xml

[41] M. Aiello, C. Cavaliere, A. D'Albore, and M. Salvatore, "The Challenges of Diagnostic Imaging in the Era of Big Data," *Journal of Clinical Medicine*, vol. 8, no. 3, p. 316, Mar 2019. [Online]. Available: TheChallengesofDiagnosticImagingintheEraofBigData

[42] A. S. Lundervold and A. Lundervold, "An overview of deep learning in medical imaging focusing on MRI," *Zeitschrift für Medizinische Physik*, vol. 29, no. 2, pp. 102–127, May 2019. [Online]. Available: https://linkinghub.elsevier.com/retrieve/pii/S0939388918301181

[43] A. M. Owrangi, P. B. Greer, and C. K. Glide-Hurst, "MRI-only treatment planning: Benefits and challenges," 2018. [Online]. Available: https://pubmed.ncbi.nlm.nih.gov/29393071/

[44] L. Chang, G. ChaoBang, and Y. Xi, "A MRI Denoising Method Based on 3D Nonlocal Means and Multidimensional PCA," *Computational and Mathematical Methods in Medicine*, vol. 2015, pp. 1–11, 2015. [Online]. Available: http://www.hindawi.com/journals/cmmm/2015/232389/

[45] S. J. Garnier, G. L. Bilbro, W. E. Snyder, and J. W. Gault, "Noise removal from multiple MRI images," *Journal of Digital Imaging*, vol. 7, no. 4, pp. 183–188, Nov 1994. [Online]. Available: http://link.springer.com/10.1007/BF03168537

[46] S. Vaishali, K. K. Rao, and G. V. S. Rao, "A review on noise reduction methods for brain MRI images," in *2015 International Conference on Signal Processing and Communication Engineering Systems*. IEEE, Jan 2015, pp. 363–365. [Online]. Available: https://ieeexplore.ieee.org/document/7058284

[47] I. Nagarajan and G. Lakshmi Priya, "Removal of noise in MRI images using a block difference-based filtering approach," *International Journal of Imaging Systems and Technology*, vol. 30, no. 1, pp. 203–215, Mar 2020. [Online]. Available: https://onlinelibrary.wiley.com/doi/abs/10.1002/ima.22361

[48] M. H. Hesamian, W. Jia, X. He, and P. Kennedy, "Deep Learning Techniques for Medical Image Segmentation: Achievements and Challenges," *Journal of Digital Imaging*, vol. 32, no. 4, pp. 582–596, Aug 2019. [Online]. Available: https://link.springer.com/article/10.1007/s10278-019-00227-x

[49] H. Bennani, B. McCane, and J. Cornwall, "Three Dimensional (3D) Lumbar Vertebrae Data Set," *Data Science Journal*, vol. 15, Aug 2016. [Online]. Available: http://datascience.codata.org/articles/10.5334/dsj-2016-009/

[50] L. Agisoft and R. St Petersburg, "Agisoft Metashape 1.6.5." [Online]. Available: https://www.agisoft.com/downloads/installer/

[51] B. Glocker, "UWSpineCT — Powered by Box." [Online]. Available: https://imperialcollegelondon.app.box.com/s/erhcm28aablpy1725lt93xh6pk31ply1

[52] "SpineWeb : Main / Datasets." [Online]. Available: http://spineweb.digitalimaginggroup.ca/Index.php?n=Main.Datasets

[53] E. Burian, A. Rohrmeier, S. Schlaeger, M. Dieckmeyer, M. N. Diefenbach, J. Syväri, E. Klupp, D. Weidlich, C. Zimmer, E. J. Rummeny, D. C. Karampinos, J. S. Kirschke, and T. Baum, "Lumbar muscle and vertebral bodies segmentation of chemical shift encoding-based water-fat MRI: the reference database MyoSegmenTUM spine," *BMC Musculoskeletal Disorders*, vol. 20, no. 1, p. 152, Dec 2019. [Online]. Available: https://bmcmusculoskeletdisord.biomedcentral.com/articles/10.1186/s12891-019-2528-x

[54] M. T. Löffler, A. Sekuboyina, A. Jacob, A.-L. Grau, A. Scharr, M. El Husseini, M. Kallweit, C. Zimmer, T. Baum, and J. S. Kirschke, "A Vertebral Segmentation Dataset with Fracture Grading," *Radiology: Artificial Intelligence*, vol. 2, no. 4, p. e190138, Jul 2020. [Online]. Available: http://pubs.rsna.org/doi/10.1148/ryai.2020190138

[55] "OSF — VerSe2019." [Online]. Available: https://osf.io/nqjyw/

[56] S. Sudirman, A. Al Kafri, F. Natalia, H. Meidia, N. Afriliana, W. Al-Rashdan, M. Bashtawi, and M. Al-Jumaily, "Lumbar Spine MRI Dataset," *Mendeley Data*, vol. 2, 2019. [Online]. Available: https://data.mendeley.com/datasets/k57fr854j2/2

[57] F. Natalia, H. Meidia, N. Afriliana, A. S. Al-Kafri, S. Sudirman, A. Simpson, A. Sophian, M. Al-Jumaily, W. Al-Rashdan, and M. Bashtawi, "Development of Ground Truth Data for Automatic Lumbar Spine MRI Image Segmentation," in *Proceedings - 20th International Conference on High Performance Computing and Communications, 16th International Conference on Smart City and 4th International Conference on Data Science and Systems, HPCC/SmartCity/DSS 2018*, 2019, pp. 1449–1454. [Online]. Available: https://ieeexplore.ieee.org/document/8622977

[58] O. Ronneberger, P. Fischer, and T. Brox, "U-net: Convolutional networks for biomedical image segmentation," in *Lecture Notes in Computer Science (including subseries Lecture Notes in Artificial Intelligence and Lecture Notes in Bioinformatics)*, vol. 9351. Springer Verlag, May 2015, pp. 234–241. [Online]. Available: http://lmb.informatik.uni-freiburg.de/

[59] A. S. Al-Kafri, S. Sudirman, A. Hussain, D. Al-Jumeily, F. Natalia, H. Meidia, N. Afriliana, W. Al-Rashdan, M. Bashtawi, and M. Al-Jumaily, "Boundary Delineation of MRI Images for Lumbar Spinal Stenosis Detection Through Semantic Segmentation Using Deep Neural Networks," *IEEE Access*, vol. 7, pp. 43 487–43 501, 2019. [Online]. Available: https://ieeexplore.ieee.org/document/8678637

[60] S. Yuheng and Y. Hao, "Image segmentation algorithms overview," 2017. [Online]. Available: https://arxiv.org/abs/1707.02051

[61] P. Smyth, C. Taylor, and J. Adams, "Automatic measurement of vertebral shape using active shape models," *Image and Vision Computing*, vol. 15, no. 8, Aug 1997. [Online]. Available: https://www.sciencedirect.com/science/article/abs/pii/S0262885697000061

[62] T. Cootes, C. Taylor, D. Cooper, and J. Graham, "Active Shape Models-Their Training and Application," *Computer Vision and Image Understanding*, vol. 61, no. 1, Jan 1995. [Online]. Available: https://www.sciencedirect.com/science/article/abs/pii/S1077314285710041

[63] M. S. Aslan, A. Shalaby, and A. A. Farag, "Vertebral body segmentation using a probabilistic and universal shape model," *IET Computer Vision*, vol. 9, no. 2,

pp. 234–250, Apr 2015. [Online]. Available: https://digital-library.theiet.org/content/journals/10.1049/iet-cvi.2013.0154

[64] J. Carballido-Gamio, S. J. Belongie, and S. Majumdar, "Normalized cuts for spinal MRI segmentation," in *CARS 2002 Computer Assisted Radiology and Surgery*. Berlin, Heidelberg: Springer Berlin Heidelberg, 2002, pp. 1054–1054. [Online]. Available: http://link.springer.com/10.1007/978-3-642-56168-9_212

[65] A. Bundy and L. Wallen, "Generalised Hough Transform," in *Catalogue of Artificial Intelligence Tools*. Berlin, Heidelberg: Springer Berlin Heidelberg, 1984, pp. 42–43. [Online]. Available: http://link.springer.com/10.1007/978-3-642-96868-6_84

[66] B. Howe, A. Gururajan, H. Sari-Sarraf, and L. R. Long, "Hierarchical segmentation of cervical and lumbar vertebrae using a customized generalized hough transform and extensions to active appearance models," in *Proceedings of the IEEE Southwest Symposium on Image Analysis and Interpretation*, vol. 6, 2004, pp. 182–186. [Online]. Available: https://ieeexplore.ieee.org/document/1300970?reload=true

[67] X. Zhu, X. He, P. Wang, Q. He, D. Gao, J. Cheng, and B. Wu, "A method of localization and segmentation of intervertebral discs in spine MRI based on Gabor filter bank," *BioMedical Engineering OnLine*, vol. 15, no. 1, p. 32, Dec 2016. [Online]. Available: http://www.biomedical-engineering-online.com/content/15/1/32

[68] A. Mehmood, M. Usman Akram, and M. Akhtar, "Vertebra Localization using Shape based analysis and unsupervised Clustering from X-Ray Images," *PJCIS*, vol. 1, no. 1, pp. 13–24, 2016. [Online]. Available: http://173.208.131.244:9060/xmlui/handle/123456789/823

[69] M. A. Larhmam, S. Mahmoudi, and M. Benjelloun, "Semi-automatic detection of cervical vertebrae in X-ray images using generalized hough transform," in *2012 3rd International Conference on Image Processing Theory, Tools and Applications (IPTA)*. IEEE, Oct 2012. [Online]. Available: https://ieeexplore.ieee.org/document/6469570

[70] M. A. Larhmam, M. Benjelloun, and S. Mahmoudi, "Vertebra Identification using Template Matching Model and K-means Clustering," *International Journal of Computer Assisted Radiology and Surgery*, vol. 9, no. 2, Mar 2014. [Online]. Available: https://pubmed.ncbi.nlm.nih.gov/23881250/

[71] C. G. Bampis, A. C. Bovik, M. K. Markey, and K. M. Webb, "Segmentation and extraction of the spinal canal in sagittal MR images," in *2016 IEEE Southwest Symposium on Image Analysis and Interpretation (SSIAI)*. IEEE, Mar 2016. [Online]. Available: https://ieeexplore.ieee.org/document/7459161

[72] B. Glocker, J. Feulner, A. Criminisi, D. R. Haynor, and E. Konukoglu, "Automatic localization and identification of vertebrae in arbitrary field-of-view CT scans," vol. 7512 LNCS, 2012, pp. 590–598. [Online]. Available: https://link.springer.com/chapter/10.1007/978-3-642-33454-2_73

[73] J.-T. Lu, S. Pedemonte, B. Bizzo, S. Doyle, K. P. Andriole, M. H. Michalski, R. G. Gonzalez, and S. R. Pomerantz, "DeepSPINE: Automated Lumbar Vertebral Segmentation, Disc-level Designation, and Spinal Stenosis Grading Using Deep Learning," *arXiv*, vol. 85, pp. 1–16, Jul 2018. [Online]. Available: http://arxiv.org/abs/1807.10215

[74] R. Janssens and G. Zheng, "Deep Learning based Segmentation of Lumbar Vertebrae from CT Images," pp. 94–89, Jul 2018. [Online]. Available: http://lit.fe.uni-lj.si/xVertSeg/

[75] B. Sendov, "Hausdorff Distance," in *Hausdorff Approximations*. Dordrecht: Springer Netherlands, 1990, pp. 23–48. [Online]. Available: http://link.springer.com/10.1007/978-94-009-0673-0_2

[76] N. Lessmann, B. van Ginneken, P. A. de Jong, and I. Išgum, "Iterative fully convolutional neural networks for automatic vertebra segmentation and identification," *Medical Image Analysis*, vol. 53, pp. 142–155, Apr 2019. [Online]. Available: http://arxiv.org/abs/1804.04383http://dx.doi.org/10.1016/j.media.2019.02.005https://linkinghub.elsevier.com/retrieve/pii/S1361841518305905

[77] H. Tang, X. Pei, S. Huang, X. Li, and C. Liu, "Automatic Lumbar Spinal CT Image Segmentation with a Dual Densely Connected U-Net," *IEEE Access*, vol. 8, pp. 89 228–89 238, Oct 2020. [Online]. Available: http://arxiv.org/abs/1910.09198

[78] B. Benjdira, K. Ouni, M. M. Al Rahhal, A. Albakr, A. Al-Habib, and E. Mahrous, "Spinal cord segmentation in ultrasound medical imagery," *Applied Sciences (Switzerland)*, vol. 10, no. 4, Feb 2020. [Online]. Available: https://www.mdpi.com/2076-3417/10/4/1370

[79] Z. Ghogawala, J. Dziura, W. E. Butler, F. Dai, N. Terrin, S. N. Magge, J.-V. C. Coumans, J. F. Harrington, S. Amin-Hanjani, J. S. Schwartz *et al.*, "Laminectomy plus fusion versus laminectomy alone for lumbar spondylolisthesis," *New England Journal of Medicine*, vol. 374, no. 15, pp. 1424–1434, 2016. [Online]. Available: https://www.nejm.org/doi/full/10.1056/NEJMoa1508788

[80] T. Hassan and N. Werghi, "Exploiting the Transferability of Deep Learning Systems Across Multi-modal Retinal Scans for Extracting Retinopathy Lesions," in *2020 IEEE 20th International Conference on Bioinformatics and Bioengineering (BIBE)*. IEEE, Oct 2020. [Online]. Available: https://ieeexplore.ieee.org/abstract/document/9288039

[81] T. Hassan, M. U. Akram, N. Werghi, and N. Nazir, "RAG-FW: A hybrid convolutional framework for the automated extraction of retinal lesions and lesion-influenced grading of human retinal pathology," *IEEE Journal of Biomedical and Health Informatics*, pp. 1–1, 2020. [Online]. Available: https://ieeexplore.ieee.org/document/9049083/

[82] V. Badrinarayanan, A. Kendall, and R. Cipolla, "SegNet: A Deep Convolutional Encoder-Decoder Architecture for Image Segmentation," *IEEE Transactions on Pattern Analysis and Machine Intelligence*, vol. 39, no. 12, pp. 2481–2495, Dec 2017. [Online]. Available: https://ieeexplore.ieee.org/document/7803544/

[83] H. Zhao, J. Shi, X. Qi, X. Wang, and J. Jia, "Pyramid Scene Parsing Network," in *2017 IEEE Conference on Computer Vision and Pattern Recognition (CVPR)*. IEEE, Jul 2017, pp. 6230–6239. [Online]. Available: http://ieeexplore.ieee.org/document/8100143/

[84] T. Joyce, A. Chartsias, and S. A. Tsaftaris, "Deep Multi-Class Segmentation Without Ground-Truth Labels," Amsterdam, Jul 2018. [Online]. Available: https://openreview.net/forum?id=S11Xr-3iM

[85] I. J. Goodfellow, J. Pouget-Abadie, M. Mirza, B. Xu, D. Warde-Farley, S. Ozair, A. Courville, and Y. Bengio, "Generative Adversarial Nets," in *Proceedings of the 27th International Conference on Neural Information Processing Systems - Volume 2December 2014*, 2014, pp. 2672–2680. [Online]. Available: https://dl.acm.org/doi/10.5555/2969033.2969125

[86] N. J. MacIntyre, L. Bennett, A. M. Bonnyman, and P. W. Stratford, "Optimizing Reliability of Digital Inclinometer and Flexicurve Ruler Measures of Spine Curvatures in Postmenopausal Women with Osteoporosis of the Spine: An Illustration of the Use of Generalizability Theory," *ISRN Rheumatology*, vol. 2011, Feb 2011. [Online]. Available: https://www.ncbi.nlm.nih.gov/pmc/articles/PMC3317083/

[87] W. Rheault, S. Ferris, J. A. Foley, D. Schaffhauser, and R. Smith, "Intertester reliability of the flexible ruler for the cervical spine," *Journal of Orthopaedic & Sports Physical Therapy*, vol. 10, no. 7, pp. 254–256, 1989.

[88] M. Kargarfard, R. Mahdavi-Nejad, G.-A. Ghasemi, R. Rouzbehani, M. Ghias, Z. Mahdavi-Jafari, and M. Dahghani, "Assessment of spinal curvature in isfahan university students." *Journal of Isfahan Medical School*, vol. 27, no. 102, 2010.

[89] B. S. Russell, K. A. Muhlenkamp, K. T. Hoiriis, and C. M. DeSimone, "Measurement of lumbar lordosis in static standing posture with and without high-heeled shoes," *Journal of Chiropractic Medicine*, vol. 11, no. 3, pp. 145–153, Sep 2012. [Online]. Available: https://www.ncbi.nlm.nih.gov/pmc/articles/PMC3437344/

[90] B. S. Russell, K. A. Muhlenkamp-Wermert, and K. T. Hoiriis, "Measurement of Lumbar Lordosis: A Comparison of 2 Alternatives to the Cobb Angle," *Journal of Manipulative and Physiological Therapeutics*, Oct 2020. [Online]. Available: https://www.sciencedirect.com/science/article/abs/pii/S0161475420301305

[91] P. Rajnics, V. Pomero, A. Templier, F. Lavaste, and T. Illes, "Computer-Assisted Assessment of Spinal Sagittal Plane Radiographs," *Journal of Spinal Disorders*, vol. 14, no. 2, Apr 2001. [Online]. Available: https://pubmed.ncbi.nlm.nih.gov/11285426/

[92] R. Vialle, N. Levassor, L. Rillardon, A. Templier, W. Skalli, and P. Guigui, "Radiographic Analysis of the Sagittal Alignment and Balance of the Spine in Asymptomatic Subjects," *The Journal of Bone & Joint Surgery*, vol. 87, no. 2, Feb 2005. [Online]. Available: https://pubmed.ncbi.nlm.nih.gov/15687145/

[93] P. Roussouly, S. Gollogly, E. Berthonnaud, and J. Dimnet, "Classification of the Normal Variation in the Sagittal Alignment of the Human Lumbar Spine and Pelvis in the Standing Position," *Spine*, vol. 30, no. 3, Feb 2005. [Online]. Available: https://pubmed.ncbi.nlm.nih.gov/15682018/

[94] J. R. Dimar, L. Y. Carreon, H. Labelle, M. Djurasovic, M. Weidenbaum, C. Brown, and P. Roussouly, "Intra- and inter-observer reliability of determining radiographic sagittal parameters of the spine and pelvis using a manual and a computer-assisted methods," *European Spine Journal*, vol. 17, no. 10, Oct 2008. [Online]. Available: https://www.ncbi.nlm.nih.gov/pmc/articles/PMC2556466/

[95] E. Babai, A. Khodamoradi, Z. Mosavi, and S. Bahari, "An innovative software method for measuring lumbar lordosis," *Annals of Biological Research*, vol. 3, no. 1, pp. 204–213, 2012. [Online]. Available: https://www.scholarsresearchlibrary.com/abstract/an-innovative-software-method-for-measuring-lumbar-lordosis-9108.html

[96] N. J. MacIntyre, C. P. Recknor, and J. C. Recknor, "Spine Curve Measures Taken in Individuals with Osteoporosis and Osteopenia Using the IONmed Mobile Phone Application Are Highly Consistent with Digital Inclinometer Measures," *ISRN Rehabilitation*, vol. 2014, Apr 2014. [Online]. Available: https://www.hindawi.com/journals/isrn/2014/508414/

[97] J. Zhang, H. Li, L. Lv, and Y. Zhang, "Computer-Aided Cobb Measurement Based on Automatic Detection of Vertebral Slopes Using Deep Neural Network," *International Journal of Biomedical Imaging*, vol. 2017, 2017. [Online]. Available: https://www.hindawi.com/journals/ijbi/2017/9083916/

[98] S. Pang, Z. Su, S. Leung, I. B. Nachum, B. Chen, Q. Feng, and S. Li, "Direct automated quantitative measurement of spine by cascade amplifier regression network with manifold regularization," *Medical Image*

Analysis, vol. 55, pp. 103–115, Jul 2019. [Online]. Available: https://www.sciencedirect.com/science/article/abs/pii/S136184151830447X

[99] B. H. Cho, D. Kaji, Z. B. Cheung, I. B. Ye, R. Tang, A. Ahn, O. Carrillo, J. T. Schwartz, A. A. Valliani, E. K. Oermann, V. Arvind, D. Ranti, L. Sun, J. S. Kim, and S. K. Cho, "Automated Measurement of Lumbar Lordosis on Radiographs Using Machine Learning and Computer Vision," *Global Spine Journal*, vol. 10, no. 5, pp. 611–618, Aug 2020. [Online]. Available: https://journals.sagepub.com/doi/full/10.1177/2192568219868190

[100] I. S. Masad, A. Al-Fahoum, and I. Abu-Qasmieh, "Automated measurements of lumbar lordosis in T2-MR images using decision tree classifier and morphological image processing," *Engineering Science and Technology, an International Journal*, vol. 22, no. 4, pp. 1027–1034, Aug 2019. [Online]. Available: https://www.sciencedirect.com/science/article/pii/S2215098618321414

[101] R. L. Drake, A. W. Vogl, and A. W. Mitchell, *Gray's Anatomy for Students, 4th Edition*, 2019. [Online]. Available: https://www.elsevier.com/books/grays-anatomy-for-students/drake/978-0-323-39304-1

[102] J. Highsmith, "Spinal Anatomy Center — Cervical, Thoracic, and Lumbar Spine Info." [Online]. Available: https://www.spineuniverse.com/anatomy

[103] J. P. G. Urban and S. Roberts, "Degeneration of the intervertebral disc," *Arthritis research & therapy*, vol. 5, no. 3, pp. 120–130, 2003. [Online]. Available: https://pubmed.ncbi.nlm.nih.gov/12723977https://www.ncbi.nlm.nih.gov/pmc/articles/PMC165040/

[104] J. Kim, S.-J. Yang, H. Kim, Y. Kim, J. B. Park, C. DuBose, and T.-H. Lim, "Effect of Shear Force on Intervertebral Disc (IVD) Degeneration: An In Vivo Rat Study," *Annals of Biomedical Engineering*, vol. 40, no. 9, pp. 1996–2004, Sep 2012. [Online]. Available: http://link.springer.com/10.1007/s10439-012-0570-z

[105] C. Colosimo, M. Pileggi, A. Pedicelli, G. Perotti, and A. M. Costantini, "Diagnostic Imaging of Degenerative Spine Diseases: The Technical Approach," in *Minimally Invasive Surgery of the Lumbar Spine*. London: Springer London, 2014. [Online]. Available: https://link.springer.com/chapter/10.1007/978-1-4471-5280-4_2

[106] P. P. Raj, "Intervertebral disc: Anatomy-physiology-pathophysiology-treatment," pp. 18–44, 2008. [Online]. Available: https://pubmed.ncbi.nlm.nih.gov/18211591/

[107] A. P. Goode, T. S. Carey, and J. M. Jordan, "Low back pain and lumbar spine osteoarthritis: how are they related?" *Current rheumatology reports*, vol. 15, no. 2, p. 305, 2013. [Online]. Available: https://www.ncbi.nlm.nih.gov/pmc/articles/PMC3606549/

[108] S. Hashimoto, L. Creighton-Achermann, K. Takahashi, D. Amiel, R. Coutts, and M. Lotz, "Development and regulation of osteophyte formation during experimental osteoarthritis," *Osteoarthritis and cartilage*, vol. 10, no. 3, pp. 180–187, 2002. [Online]. Available: https://www.oarsijournal.com/article/S1063-4584(01)90505-9/pdf

[109] O. Osti, B. Vernon-Roberts, R. Moore, and R. Fraser, "Annular tears and disc degeneration in the lumbar spine. a post-mortem study of 135 discs," *The Journal of bone and joint surgery. British volume*, vol. 74, no. 5, pp. 678–682, 1992. [Online]. Available: https://online.boneandjoint.org.uk/doi/abs/10.1302/0301-620X.74B5.1388173

[110] B. Roudsari and J. G. Jarvik, "Lumbar spine MRI for low back pain: Indications and yield," Sep 2010. [Online]. Available: https://www.ajronline.org/doi/10.2214/AJR.10.4367

[111] K. Luoma, H. Riihimäki, R. Luukkonen, R. Raininko, E. Viikari-Juntura, and A. Lamminen, "Low back pain in relation to lumbar disc degeneration," *Spine*, 2000. [Online]. Available: https://pubmed.ncbi.nlm.nih.gov/10707396/

[112] J. L. Melancia, A. F. Francisco, and J. L. Antunes, "Spinal stenosis," in *Handbook of Clinical Neurology*. Elsevier B.V., 2014, vol. 119, pp. 541–549. [Online]. Available: https://linkinghub.elsevier.com/retrieve/pii/B9780702040863000357

[113] S. D. Glassman, K. Bridwell, J. R. Dimar, W. Horton, S. Berven, and F. Schwab, "The impact of positive sagittal balance in adult spinal deformity," *Spine*, 2005. [Online]. Available: https://pubmed.ncbi.nlm.nih.gov/16166889/

[114] Stephanie Watson, "Top Causes of Low Back Pain." [Online]. Available: https://www.webmd.com/back-pain/features/causes

[115] J. A. Carrino, J. D. Lurie, A. N. A. Tosteson, T. D. Tosteson, E. J. Carragee, J. Kaiser, M. R. Grove, E. Blood, L. H. Pearson, J. N. Weinstein, and R. Herzog, "Lumbar Spine: Reliability of MR Imaging Findings," *Radiology*, vol. 250, no. 1, Jan 2009. [Online]. Available: https://pubs.rsna.org/doi/full/10.1148/radiol.2493071999

[116] S. Ansari, M. Amanullah, K. Ahmad, and R. K. Rauniyar, "Pott's spine: Diagnostic imaging modalities and technology advancements," pp. 404–411, Jul 2013. [Online]. Available: https://pubmed.ncbi.nlm.nih.gov/24020048/

[117] Mehmet Demir, E. Gumusburun, N. Seringec, M. Cicek, R. Ertugrul, and K. . Bulent Guneri Department of Orthopedics and Traumatology, Faculty of Medicine, Kahramanmaras Sutcu Imam University, "Radiographic analysis of the lumbar and sacral region angles in young Turkish adults," *Journal of the Pakistan Medical Association*, vol. 68, no. 8, 2018. [Online]. Available: https://www.jpma.org.pk/article-details/8813?article_id=8813

[118] S.-J. Hyun, S. Han, Y. B. Kim, Y. J. Kim, G.-B. Kang, and J.-Y. Cheong, "Predictive formula of ideal lumbar lordosis and lower lumbar lordosis determined by individual pelvic incidence in asymptomatic elderly population," *European Spine Journal*, vol. 28, no. 9, Sep 2019. [Online]. Available: https://link.springer.com/article/10.1007/s00586-019-05955-w

[119] D. Czaprowski, Ł. Stoliński, M. Tyrakowski, M. Kozinoga, and T. Kotwicki, "Non-structural misalignments of body posture in the sagittal plane," *Scoliosis and spinal disorders*, vol. 13, p. 6, Mar 2018. [Online]. Available: https://pubmed.ncbi.nlm.nih.gov/29516039

[120] Benjamin Bjerke, "What Is Spinal Stenosis?" [Online]. Available: https://www.spine-health.com/conditions/spinal-stenosis/what-spinal-stenosis

[121] M. Haefeli and N. Boos, "Outcome assessment in spinal surgery," in *Spinal Disorders: Fundamentals of Diagnosis and Treatment*. Springer Berlin Heidelberg, 2008, pp. 1123–1142. [Online]. Available: https://link.springer.com/chapter/10.1007/978-3-540-69091-7_40

[122] F. Brunner, S. Weiser, A. Schmid, and M. Nordin, "Non-specific low back pain," in *Spinal Disorders: Fundamentals of Diagnosis and Treatment.*

Springer Berlin Heidelberg, 2008, pp. 585–601. [Online]. Available: https://link.springer.com/chapter/10.1007/978-3-540-69091-7_21

[123] Peter Ullrich, "Lumbar Spine Surgery." [Online]. Available: https://www.spine-health.com/treatment/back-surgery/lumbar-spine-surgery

[124] T. J. Errico, B. S. Lonner, and A. W. Moulton, *Surgical Management of Spinal Deformities*. Elsevier Inc., 2009. [Online]. Available: https://www.sciencedirect.com/book/9781416033721/surgical-management-of-spinal-deformities

[125] "Microdisectomy: Benefits, procedure, and recovery," July 2017, (Accessed on 12/26/2020). [Online]. Available: https://www.healthline.com/health/microdiscectomy

[126] "Laminectomy — johns hopkins medicine," (Accessed on 12/26/2020). [Online]. Available: https://www.hopkinsmedicine.org/health/treatment-tests-and-therapies/laminectomy

[127] I. A. Harris, A. Traeger, R. Stanford, C. G. Maher, and R. Buchbinder, "Lumbar spine fusion: what is the evidence?" *Internal Medicine Journal*, vol. 48, no. 12, pp. 1430–1434, Dec 2018.

[128] G. Logroscino and W. Lattanzi, "Bone Substitution in Spine Fusion: The Past, the Present, and the Future," in *Minimally Invasive Surgery of the Lumbar Spine*. London: Springer London, 2014. [Online]. Available: https://link.springer.com/chapter/10.1007%2F978-1-4471-5280-4_15

[129] R. J. Rothrock, I. T. McNeill, K. Yaeger, E. K. Oermann, S. K. Cho, and J. M. Caridi, "Lumbar Lordosis Correction with Interbody Fusion: Systematic Literature Review and Analysis," pp. 21–31, Oct 2018. [Online]. Available: https://www.sciencedirect.com/science/article/abs/pii/S1878875018314323

[130] C. C. Niu, T. T. Tsai, T. S. Fu, P. L. Lai, L. H. Chen, and W. J. Chen, "A comparison of posterolateral lumbar fusion comparing autograft, autogenous laminectomy bone with bone marrow aspirate, and calcium sulphate with bone marrow aspirate: A prospective randomized study," *Spine*, 2009. [Online]. Available: https://journals.lww.com/spinejournal/Abstract/2009/12010/A_Comparison_of_Posterolateral_Lumbar_Fusion.2.aspx

[131] P. Ullrich, "Posterior Lumbar Interbody Fusion (PLIF) Video," 2009. [Online]. Available: https://www.spine-health.com/video/posterior-lumbar-interbody-fusion-plif-video

[132] T. Harrington and S. Javedan, "Posterior lumbar interbody fusion," *Neurosurgery Quarterly*, vol. 10, no. 3, pp. 228–238, 2000. [Online]. Available: https://www.spine-health.com/treatment/spinal-fusion/posterior-lumbar-interbody-fusion-plif-surgery

[133] M. Montgomery, Stephen, "Transforaminal Lumbar Interbody Fusion (TLIF) Back Surgery," 2005. [Online]. Available: https://www.spine-health.com/treatment/spinal-fusion/transforaminal-lumbar-interbody-fusion-tlif-back-surgery

[134] M. Deviren, Vedat, "XLIF: Lumbar Spinal Fusion," 2009. [Online]. Available: https://www.spine-health.com/treatment/spinal-fusion/xlif-lumbar-spinal-fusion

[135] A. Keller, J. Hayden, C. Bombardier, and M. Van Tulder, "Effect sizes of non-surgical treatments of non-specific low-back pain," 2007. [Online]. Available: https://link.springer.com/article/10.1007%2Fs00586-007-0379-x

[136] C. B. Oliveira, C. G. Maher, R. Z. Pinto, A. C. Traeger, C. W. C. Lin, J. F. Chenot, M. van Tulder, and B. W. Koes, "Clinical practice guidelines for the management of non-specific low back pain in primary care: an updated overview," 2018. [Online]. Available: https://link.springer.com/article/10.1007/s00586-018-5673-2

[137] T. P. Yamato, C. G. Maher, B. T. Saragiotto, M. J. Hancock, R. W. Ostelo, C. M. Cabral, L. C. Menezes Costa, and L. O. Costa, "Pilates for low back pain," *Sao Paulo Medical Journal*, 2016. [Online]. Available: https://www.scielo.br/scielo.php?script=sci_arttext&pid=S1516-31802016000400366

[138] L. A. Carneiro Machado, M. V. S. De Souza, P. H. Ferreira, and M. L. Ferreira, "The McKenzie method for low back pain: A systematic review of the literature with a meta-analysis approach," *Spine*, 2006. [Online]. Available: https://journals.lww.com/spinejournal/Abstract/2006/04200/The_McKenzie_Method_for_Low_Back_Pain__A.22.aspx

[139] L. A. Machado, C. G. Maher, R. D. Herbert, H. Clare, and J. H. McAuley, "The effectiveness of the McKenzie method in addition to first-line care for

acute low back pain: A randomized controlled trial," *BMC Medicine*, 2010. [Online]. Available: https://bmcmedicine.biomedcentral.com/articles/10.1186/1741-7015-8-10

[140] S. C. Kao and C. S. Lin, "Caudal Epidural Block: An Updated Review of Anatomy and Techniques," 2017. [Online]. Available: https://www.hindawi.com/journals/bmri/2017/9217145/

[141] C. E. Kosasih, T. Solehati, and A. Cakrahayat, "Non-Invasive Treatment To Reduce Low Back Pain Among Treatment Acupunture, Massage, Spinal Manipulation, Yoga, And Tai Chi A Systematic Review," *Journal of Maternity Care and Reproductive Health*, 2018. [Online]. Available: http://www.mcrhjournal.or.id/index.php/jmcrh/article/view/9

[142] D. R. Murphy, "Chiropractic rehabilitation of the cervical spine," *Journal of Manipulative and Physiological Therapeutics*, 2000. [Online]. Available: https://www.sciencedirect.com/science/article/abs/pii/S016147540001263X

[143] K. Ammer, "Thermography in spinal disorders - A narrative review," 2010. [Online]. Available: http://www.uhlen.at/thermology-international/archive/abstract%2020_4_1.html

[144] C. J. Standaert, "Spondylolysis: a critical review," *British Journal of Sports Medicine*, vol. 34, no. 6, pp. 415–422, Dec 2000. [Online]. Available: https://bjsm.bmj.com/lookup/doi/10.1136/bjsm.34.6.415

[145] J. R. Jinkins, J. C. Matthes, R. N. Sener, S. Venkatappan, and R. Rauch, "Spondylolysis, spondylolisthesis, and associated nerve root entrapment in the lumbosacral spine: MR evaluation." *American Journal of Roentgenology*, vol. 159, no. 4, Oct 1992. [Online]. Available: https://www.ajronline.org/doi/10.2214/ajr.159.4.1529846

[146] M. A. Alvi, A. Sebai, Y. Yolcu, W. Wahood, B. D. Elder, T. Kaufmann, and M. Bydon, "Assessing the Differences in Measurement of Degree of Spondylolisthesis Between Supine MRI and Erect X-Ray: An Institutional Analysis of 255 Cases," *Operative Neurosurgery*, Aug 2019. [Online]. Available: https://academic.oup.com/ons/article-abstract/doi/10.1093/ons/opz180/5543969/https://academic.oup.com/ons/advance-article/doi/10.1093/ons/opz180/5543969

[147] L. L. Wiltse, "Classification, Terminology and Measurements in Spondylolisthesis," pp. 52–57, 1981. [Online]. Available: https://www.ncbi.nlm.nih.gov/pmc/articles/PMC2328707/

[148] "Wiltse classification (spondylolisthesis) — Radiology Reference Article — Radiopaedia.org." [Online]. Available: https://radiopaedia.org/articles/wiltse-classification-spondylolisthesis?lang=gb

[149] H. W. Meyerding, "Spondyloptosis," *Surg Gynaecol Obstet*, vol. 54, pp. 371–377, 1932.

[150] B. Danielson, K. Frennered, G. Selvik, and L. Irstam, "Roentgenologic Assessment of Spondylolisthesis," *Acta Radiologica*, vol. 30, no. 1, pp. 65–68, 1989. [Online]. Available: https://www.tandfonline.com/doi/abs/10.3109/02841858909177460

[151] "Spondyloptosis — Radiology Reference Article — Radiopaedia.org." [Online]. Available: https://radiopaedia.org/articles/spondyloptosis?lang=gb

[152] T. S. de Oliveira, C. T. Candotti, M. La Torre, P. P. T. Pelinson, T. S. Furlanetto, F. M. Kutchak, and J. F. Loss, "Validity and Reproducibility of the Measurements Obtained Using the Flexicurve Instrument to Evaluate the Angles of Thoracic and Lumbar Curvatures of the Spine in the Sagittal Plane," *Rehabilitation Research and Practice*, vol. 2012, 2012. [Online]. Available: https://www.hindawi.com/journals/rerp/2012/186156/

[153] I. A. F. Stokes, "Three-dimensional terminology of spinal deformity. A report presented to the Scoliosis Research Society by the Scoliosis Research Society Working Group on 3-D terminology of spinal deformity," *Spine*, 1994. [Online]. Available: https://pubmed.ncbi.nlm.nih.gov/8153835/

[154] T. Vrtovec, F. Pernuš, and B. Likar, "A review of methods for quantitative evaluation of spinal curvature," *European Spine Journal*, vol. 18, no. 5, pp. 593–607, May 2009.

[155] R. M. Lin, I. M. Jou, and C. Y. Yu, "Lumbar lordosis: normal adults." *Journal of the Formosan Medical Association = Taiwan yi zhi*, vol. 91, no. 3, pp. 329–333, 1992. [Online]. Available: https://pubmed.ncbi.nlm.nih.gov/1354697/

[156] H. J. Kim, S. Chung, S. Kim, H. Shin, J. Lee, S. Kim, and M. Y. Song, "Influences of trunk muscles on lumbar lordosis and sacral angle," *European Spine Journal*, 2006. [Online]. Available: https://link.springer.com/article/10.1007/s00586-005-0976-5

[157] O. Hay, G. Dar, J. Abbas, D. Stein, H. May, Y. Masharawi, N. Peled, and I. Hershkovitz, "The lumbar lordosis in males and females, revisited," *PLoS ONE*, vol. 10, no. 8, 2015. [Online]. Available: https://journals.plos.org/plosone/article?id=10.1371/journal.pone.0133685

[158] J. Legaye, G. Duval-Beaupère, J. Hecquet, and C. Marty, "Pelvic incidence: A fundamental pelvic parameter for three-dimensional regulation of spinal sagittal curves," *European Spine Journal*, 1998. [Online]. Available: https://link.springer.com/article/10.1007%2Fs005860050038

[159] C. JR, "Outlline for the Study of Scoliosis," *American Academy of Orthopaedic Surgeons*, vol. 5, p. 261, 1948.

[160] D. D. Harrison, R. Cailliet, T. J. Janik, S. J. Troyanovich, D. E. Harrison, and B. Holland, "Elliptical modeling of the sagittal lumbar lordosis and segmental rotation angles as a method to discriminate between normal and low back pain subjects." *Journal of spinal disorders*, vol. 11, no. 5, pp. 430–439, Oct 1998. [Online]. Available: https://pubmed.ncbi.nlm.nih.gov/9811104/

[161] D. E. Harrison, D. D. Harrison, R. Cailliet, S. J. Troyanovich, T. J. Janik, and B. Holland, "Cobb Method or Harrison Posterior Tangent Method," *Spine*, vol. 25, no. 16, pp. 2072–2078, Aug 2000. [Online]. Available: http://journals.lww.com/00007632-200008150-00011

[162] D. E. Harrison, R. Cailliet, D. D. Harrison, T. J. Janik, and B. Holland, "Reliability of centroid, Cobb, and Harrison posterior tangent methods: which to choose for analysis of thoracic kyphosis." Tech. Rep. 11, 2001. [Online]. Available: https://pubmed.ncbi.nlm.nih.gov/11389406/

[163] T. Vrtovec, B. Likar, and F. Pernuš, "Manual and computerized measurement of sagittal vertebral inclination in computed tomography images," *Spine*, vol. 36, no. 13, Jun 2011. [Online]. Available: https://pubmed.ncbi.nlm.nih.gov/21289562/

[164] D. W. Polly, F. X. Kilkelly, K. A. McHale, L. M. Asplund, M. Mulligan, and A. S. Chang, "Measurement of Lumbar Lordosis," *Spine*, vol. 21, no. 13, pp. 1530–1535, Jul 1996. [Online]. Available: http://journals.lww.com/00007632-199607010-00008

[165] A. Ishihara, "Roentgenographic studies on the normal pattern of the cervical curvature," *Journal of the Japanese Orthopaedic Association*, vol. 42, no. 11, pp. 1033–1044, Nov 1968. [Online]. Available: https://pubmed.ncbi.nlm.nih.gov/5752136/

[166] S. A. Voutsinas and G. D. MacEwen, "Sagittal Profiles of the Spine," *Clinical Orthopaedics and Related Research®*, vol. 210, 1986. [Online]. Available: https://journals.lww.com/clinorthop/Fulltext/1986/09000/Sagittal_Profiles_of_the_Spine.34.aspx

[167] Y. L. Chen, "Vertebral centroid measurement of lumbar lordosis compared with the Cobb technique," *Spine*, vol. 24, no. 17, pp. 1786–1790, Sep 1999. [Online]. Available: https://pubmed.ncbi.nlm.nih.gov/10488508/

[168] B. P. Yang, C. W. Yang, and S. L. Ondra, "A novel mathematical model of the sagittal spine," *Spine*, vol. 32, no. 4, pp. 466–470, Feb 2007. [Online]. Available: https://pubmed.ncbi.nlm.nih.gov/17304139/

[169] F. O. Okpala, "Comparison of four radiographic angular measures of lumbar lordosis," *Journal of Neurosciences in Rural Practice*, vol. 9, no. 3, pp. 298–304, Jul 2018. [Online]. Available: https://pubmed.ncbi.nlm.nih.gov/30069082/

[170] D. A. Vacari, E. B. Neves, and L. Ulbricht, "Comparison between methods of assessing lumbosacral curve obtained by radiographic image," *Acta Ortopédica Brasileira*, vol. 23, no. 2, 2015. [Online]. Available: https://pubmed.ncbi.nlm.nih.gov/27069403/

[171] J. Weese and C. Lorenz, "Four challenges in medical image analysis from an industrial perspective," *Medical Image Analysis*, vol. 33, pp. 44–49, Oct 2016. [Online]. Available: https://linkinghub.elsevier.com/retrieve/pii/S1361841516300998

[172] I.-R. Chen and T.-S. Wei, "Disc Height and Lumbar Index as Independent Predictors of Degenerative Spondylolisthesis in Middle-Aged Women With Low Back Pain," *Spine*, vol. 34, no. 13, Jun 2009. [Online]. Available: https://pubmed.ncbi.nlm.nih.gov/19478661/

[173] "DICOM Viewer - RadiAnt — Products." [Online]. Available: https://www.radiantviewer.com/products/

[174] R. F. Masood, I. A. Taj, T. Hassan, M. B. Khan, and M. Talha, "Composite Dataset of Lumbar Spine Mid-Sagittal Views with Automated Spinal Measurements," 2020. [Online]. Available: https://data.mendeley.com/datasets/k3b363f3vz/1

[175] K. Zuiderveld, "Contrast Limited Adaptive Histogram Equalization," in *Graphics Gems*, 1994. [Online]. Available: https://www.sciencedirect.com/science/article/pii/B9780123361561500616?via%3Dihub

[176] G. Sotak and K. Boyer, "The laplacian-of-gaussian kernel: A formal analysis and design procedure for fast, accurate convolution and full-frame output," *Computer Vision, Graphics, and Image Processing*, vol. 48, no. 2, Nov 1989. [Online]. Available: https://www.sciencedirect.com/science/article/abs/pii/S0734189X89800362

[177] M. Aubry, S. Paris, S. W. Hasinoff, J. Kautz, and F. Durand, "Fast Local Laplacian Filters," *ACM Transactions on Graphics*, vol. 33, no. 5, Sep 2014. [Online]. Available: https://dl.acm.org/doi/10.1145/2629645

[178] M. I. Sezan, A. M. Tekalp, and R. Schaetzing, "Automatic Anatomically Selective Image Enhancement in Digital Chest Radiography," *IEEE Transactions on Medical Imaging*, 1989. [Online]. Available: https://ieeexplore.ieee.org/document/24863

[179] S. F. Wong and K. Y. K. Wong, "Segmenting lumbar vertebrae in digital video fluoroscopic images through edge enhancement," in *2004 8th International Conference on Control, Automation, Robotics and Vision (ICARCV)*, vol. 1. IEEE, 2004, pp. 665–670. [Online]. Available: http://ieeexplore.ieee.org/document/1468906/

[180] N. Otsu, "A Threshold Selection Method from Gray-Level Histograms," *IEEE Transactions on Systems, Man, and Cybernetics*, vol. 9, no. 1, Jan 1979. [Online]. Available: https://ieeexplore.ieee.org/document/4310076

[181] D. Bradley and G. Roth, "Adaptive Thresholding using the Integral Image," *Journal of Graphics Tools*, vol. 12, no. 2, pp. 13–21, Jan 2007. [Online]. Available: https://www.tandfonline.com/doi/full/10.1080/2151237X.2007.10129236

[182] P. Soille and P. Soille, "Opening and Closing," in *Morphological Image Analysis*. Berlin, Heidelberg: Springer Berlin Heidelberg, 1999, pp. 89–127. [Online]. Available: https://link.springer.com/chapter/10.1007/978-3-662-03939-7_4

[183] C. Bustacara, M. Gómez-Mora, and L. Flórez-Valencia, "Anisotropic Diffusion for Smoothing: A Comparative Study," 2016. [Online]. Available: https://link.springer.com/chapter/10.1007/978-3-319-46418-3_10

[184] X. Liu, Y. Zhang, H. Jing, L. Wang, and S. Zhao, "Ore image segmentation method using U-Net and Res_Unet convolutional networks," *RSC Advances*, vol. 10, no. 16, pp. 9396–9406, 2020. [Online]. Available: https://pubs.rsc.org/en/content/articlelanding/2020/ra/c9ra05877j

[185] N. Saxena, K. B. N., and B. Raman, "Semantic Segmentation of Multispectral Images using Res-Seg-net Model," in *2020 IEEE 14th International Conference on Semantic Computing (ICSC)*, 2020, pp. 154–157. [Online]. Available: https://ieeexplore.ieee.org/document/9031487

[186] Y. Shen, V. S. Sheng, L. Wang, J. Duan, X. Xi, D. Zhang, and Z. Cui, "Empirical comparisons of deep learning networks on liver segmentation," *Computers, Materials and Continua*, vol. 62, no. 3, pp. 1233–1247, 2020. [Online]. Available: https://www.techscience.com/cmc/v62n3/38351

[187] R. Zhang, L. Du, Q. Xiao, and J. Liu, "Comparison of Backbones for Semantic Segmentation Network," *Journal of Physics: Conference Series*, vol. 1544, no. 1, 2020. [Online]. Available: https://iopscience.iop.org/article/10.1088/1742-6596/1544/1/012196/pdf

[188] T. Hassan, M. U. Akram, and N. Werghi, "Evaluation of deep segmentation models for the extraction of retinal lesions from multi-modal

retinal images," 2020. [Online]. Available: https://deepai.org/publication/evaluation-of-deep-segmentation-models-for-the-extraction-of-retinal-lesions-from-multi-modal-r

[189] K. He, X. Zhang, S. Ren, and J. Sun, "Deep residual learning for image recognition," *CoRR*, vol. abs/1512.03385, 2015. [Online]. Available: http://arxiv.org/abs/1512.03385

[190] A. G. Howard, M. Zhu, B. Chen, D. Kalenichenko, W. Wang, T. Weyand, M. Andreetto, and H. Adam, "MobileNets: Efficient Convolutional Neural Networks for Mobile Vision Applications," *arXiv*, Apr 2017. [Online]. Available: http://arxiv.org/abs/1704.04861

[191] J. Long, E. Shelhamer, and T. Darrell, "Fully convolutional networks for semantic segmentation," in *2015 IEEE Conference on Computer Vision and Pattern Recognition (CVPR)*. IEEE, Jun 2015, pp. 3431–3440. [Online]. Available: http://ieeexplore.ieee.org/document/7298965/

[192] M. D. Zeiler, "ADADELTA: an adaptive learning rate method," *CoRR*, vol. abs/1212.5701, 2012. [Online]. Available: http://arxiv.org/abs/1212.5701

[193] J. Duchi, E. Hazan, and Y. Singer, "Adaptive subgradient methods for online learning and stochastic optimization," *Journal of Machine Learning Research*, 2011. [Online]. Available: https://www.jmlr.org/papers/volume12/duchi11a/duchi11a.pdf

[194] T. Tieleman and G. Hinton, "Lecture 6.5-rmsprop: Divide the gradient by a running average of its recent magnitude," *COURSERA: Neural networks for machine learning*, 2012. [Online]. Available: http://www.cs.toronto.edu/~hinton/coursera/lecture6/lec6.pdf

[195] Y. Tao, Z. Ling, and I. Patras, "Universal Foreground Segmentation Based on Deep Feature Fusion Network for Multi-Scene Videos," *IEEE Access*, vol. PP, p. 1, Oct 2019. [Online]. Available: https://ieeexplore.ieee.org/abstract/document/8888275

[196] J. Jing, Z. Wang, M. Rätsch, and H. Zhang, "Mobile-Unet: An efficient convolutional neural network for fabric defect detection," *Textile Research Journal*, 2020. [Online]. Available: https://journals.sagepub.com/doi/abs/10.1177/0040517520928604

[197] C. Balakrishna, S. Dadashzadeh, and S. Soltaninejad, "Automatic detection of lumen and media in the IVUS images using u-net with VGG16 encoder," *CoRR*, vol. abs/1806.07554, 2018. [Online]. Available: http://arxiv.org/abs/1806.07554

[198] Z. Zhou, M. M. R. Siddiquee, N. Tajbakhsh, and J. Liang, "Unet++: Redesigning skip connections to exploit multiscale features in image segmentation," *IEEE Trans. Medical Imaging*, vol. 39, no. 6, pp. 1856–1867, 2020. [Online]. Available: https://doi.org/10.1109/TMI.2019.2959609

[199] G. Csurka, D. Larlus, and F. Perronnin, "What is a good evaluation measure for semantic segmentation?" *BMVC 2013 - Electronic Proceedings of the British Machine Vision Conference 2013*, 2013. [Online]. Available: http://www.bmva.org/bmvc/2013/Papers/paper0032/index.html

[200] J. Huang, H. Shen, J. Wu, X. Hu, Z. Zhu, X. Lv, Y. Liu, and Y. Wang, "Spine Explorer: a deep learning based fully automated program for efficient and reliable quantifications of the vertebrae and discs on sagittal lumbar spine MR images," *Spine Journal*, vol. 20, no. 4, pp. 590–599, Apr 2020. [Online]. Available: https://pubmed.ncbi.nlm.nih.gov/31759132/

[201] F. Monteiro and A. C. Campilho, "Distance measures for image segmentation evaluation," in *AIP Conference Proceedings*, vol. 1479, no. 1, 2012, pp. 794–797. [Online]. Available: https://aip.scitation.org/doi/10.1063/1.4756257

[202] A. A. Taha and A. Hanbury, "Evaluation Metrics for Medical Organ Segmentation and Lesion Detection," in *Cloud-Based Benchmarking of Medical Image Analysis*. Springer International Publishing, 2017, pp. 87–105. [Online]. Available: https://link.springer.com/chapter/10.1007/978-3-319-49644-3_6

[203] F. C. Monteiro and A. C. Campilho, "Performance evaluation of image segmentation," in *International Conference Image Analysis and Recognition*. Springer, 2006, pp. 248–259. [Online]. Available: http://link.springer.com/10.1007/11867586_24

[204] Y. J. Zhang, "A review of recent evaluation methods for image segmentation," in *6th International Symposium on Signal Processing and Its Applications, ISSPA 2001 - Proceedings; 6 Tutorials in Communications, Image Processing*

and Signal Analysis, vol. 1, 2001, pp. 148–151. [Online]. Available: https://ieeexplore.ieee.org/document/949797

[205] S. Ghosh, M. R. Malgireddy, V. Chaudhary, and G. Dhillon, "A Supervised Approach Towards Segmentation of Clinical MRI for Automatic Lumbar Diagnosis," in *Lecture Notes in Computational Vision and Biomechanics*, ser. Lecture Notes in Computational Vision and Biomechanics, J. Yao, T. Klinder, and S. Li, Eds. Cham: Springer International Publishing, 2014, vol. 17, pp. 185–195. [Online]. Available: http://link.springer.com/10.1007/978-3-319-07269-2_16

[206] M. Rak, J. Steffen, A. Meyer, C. Hansen, and K. D. Tönnies, "Combining convolutional neural networks and star convex cuts for fast whole spine vertebra segmentation in MRI," *Computer Methods and Programs in Biomedicine*, vol. 177, pp. 47–56, 2019. [Online]. Available: https://www.sciencedirect.com/science/article/abs/pii/S0169260718307417

[207] A. Suzani, A. Seitel, Y. Liu, S. S. Fels, R. N. Rohling, and P. Abolmaesumi, "Fast automatic vertebrae detection and localization in pathological CT scans - A deep learning approach," in *Medical Image Computing and Computer-Assisted Intervention - MICCAI 2015 - 18th International Conference Munich, Germany, October 5 - 9, 2015, Proceedings, Part III*, ser. Lecture Notes in Computer Science, N. Navab, J. Hornegger, W. M. W. III, and A. F. Frangi, Eds., vol. 9351. Springer, 2015, pp. 678–686. [Online]. Available: https://doi.org/10.1007/978-3-319-24574-4_81

[208] S. Helgason and S. Helgason, *The radon transform*. Springer, 1980, vol. 2. [Online]. Available: https://link.springer.com/book/10.1007%2F978-1-4757-1463-0

[209] D. J. Williams and M. Shah, "A fast algorithm for active contours," in *Proceedings Third International Conference on Computer Vision*. IEEE Comput. Soc. Press, 1990, pp. 592–595. [Online]. Available: https://ieeexplore.ieee.org/abstract/document/139602

[210] D. P. Kingma and J. Ba, "Adam: A method for stochastic optimization," 2017. [Online]. Available: https://arxiv.org/abs/1412.6980

Appendix A

Miscellaneous Techniques used for Vertebral Body Segmentation

The selected methods suggested by other researchers to perform segmentation related task are described below:

- **Gabor Filter**

  Being orientation-sensitive filters, Gabor filters [67] are commonly advocated for their superior performance in texture analysis. To perform experimentation. initially, Gabor filter bank was defined with equidistance angular variation of 30° and same wavelength. It was revealed through experimentation and variation of angles that minimal structural similarity information was extracted out from the binarized images in case of VB segmentation. The result of Gabor filter bank with constant wavelength and different angular variation is given in figure A.1.

- **Radon Transform**

  Radon Transform [208] forms the foundation of image reconstruction in tomography was also tested in order to segment the region of interest in this case the VBs. Through experimentation it was established that θ range from

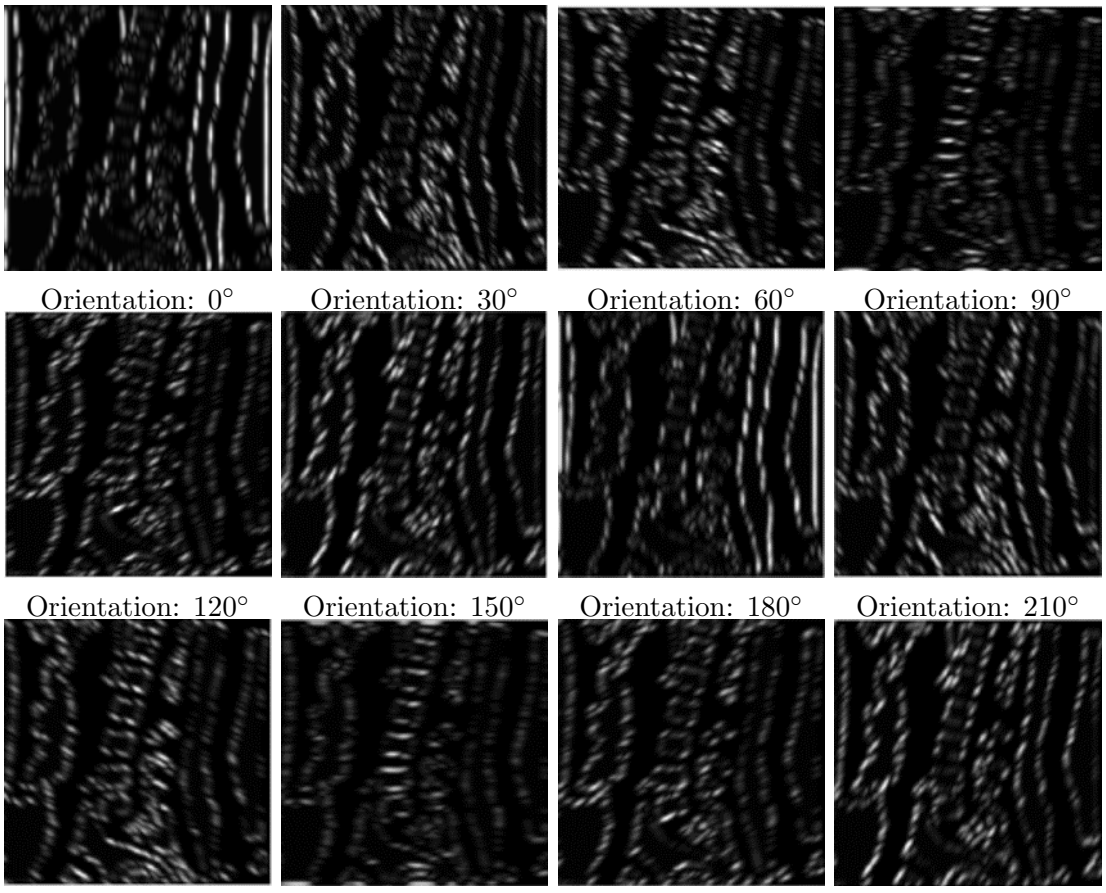

FIGURE A.1: Result with Gabor Filter using Gabor Filter Bank of Orientation Mentioned as sub-caption.

[30, 45] has proved very effective in filtering out the IVDs. It involves application of application of Radon transformation to the original mask in the specified theta range θ, later reconstructing the image with inversion Radon transformation in the same range of θ. Afterwards, LoG is applied and magnitude of gradient of image is computed. Image is converted to grayscale to form a mask; the resultant mask is later subtracted from the original image. The expression to compute Radon transform is given as under:

$$R_\theta(x') = \int_{-\infty}^{\infty} f(x' \cos\theta - y' \sin\theta, x' \sin\theta + y' \cos\theta) dy' \tag{A.1}$$

where,

$$\begin{bmatrix} x' \\ y' \end{bmatrix} = \begin{bmatrix} \cos\theta & \sin\theta \\ -\sin\theta & \cos\theta \end{bmatrix} \begin{bmatrix} x \\ y \end{bmatrix}$$

As evident from figure A.2, Radon transform filtered the IVDs by using back-projection, however, the end-plates of VB bones as depicted by red arrows and boundary information of IVD shown by yellow arrows are not intact. An improvement is to include other directions to reconstruct the image but was not suited well due to the challenge given by variety of lumbar spine structures in the images.

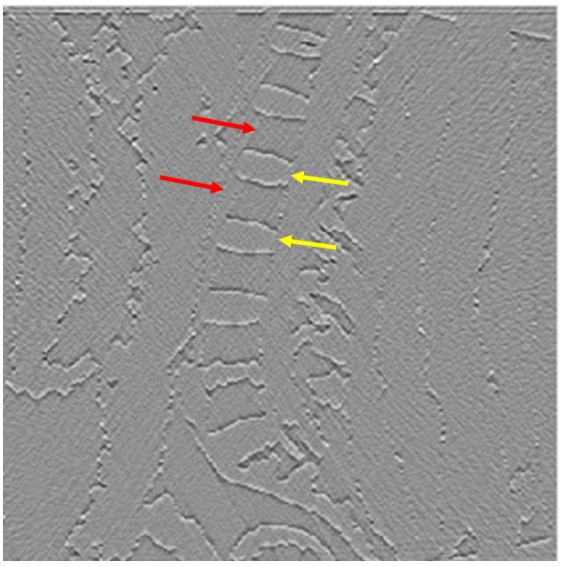

FIGURE A.2: Mask using Radon Transform.

- **Active Contours**

  Active Contours Method [209] (Snakes) algorithm was also experimented as being extensively used in the research work. The basic limitation found was that user interaction (seed) was involved in making a region of interest (ROI) to perform clustering based on Snakes Algorithm. This method suggested intervention by user therefore was not found suitable to develop fully automated segmentation tool without the user-intervention.

Appendix B

Implementing Deep Learning with MATLAB

An effort to check the suitability of deep learning toolbox in MATLAB to perform the semantic segmentation is also carried out. The results obtained through Python are far superior in both qualitative and quantitative aspects as given in Chapter 8 section 8.3.1.

While implementing semantic segmentation, same sequence of transfer learning protocol is followed. The sequence of steps performed are as under:

- Initially two-datastores are defined namely, the image datastore containing the input images and labels datastore comprising of ground truth labels.
- The images are then distributed into training images and test images with 70 % and 30 % of the entire dataset respectively.
- Class labels are balanced since, the ROI is limited to 6 VBs with major portion of the target image is composed of background.
- A pre-trained model like VGG16, VGG19, UNet is imported and target segmentation network i.e., SegNet model is defined.

- The last classification layer of the source model is clipped and newly defined layer containing the 7 class labels including the background pixels is appended with the target SegNet model.
- The training hyperparameters are then defined including the default learning rate, choice of optimizer like stochastic gradient descent with momentum, RMSprop and Adam[210], cross entropy loss function, regularization parameters.
- In the last step, training is performed followed by evaluation.

The training is performed with all three optimizers available i.e., stochastic gradient descent with momentum (SGDM), root mean square propagation (RMSProp) and adaptive moment estimation (Adam) optimizers in deep learning toolbox.